Study of calcium silicate glasses derived from agro-food wastes and minerals for biomedical applications

A THESIS

submitted by

Navneet Kaur
Registration no. 902012008

under the guidance of

Dr. Kulvir Singh
Professor

for the partial fulfillment of the award of the degree

of

Doctor of Philosophy

Department of Physics and Material Science
Thapar Institute of Engineering and Technology
(Deemed-to-be-University)
Patiala-147004, Punjab, India

June 2025

Declaration

I hereby certify that the work which is presented in the thesis entitled "**Study of calcium silicate glasses derived from agro-food wastes and minerals for biomedical applications**" in the partial fulfillment of requirements for the award of the degree of **Doctor of Philosophy** in the Department of Physics and Material Science, Thapar Institute of Engineering and Technology, Patiala (Punjab), India, is an authentic record of my own research work carried out under the supervision of Dr. Kulvir Singh. The matter embodied in this thesis has not been submitted in part or in full to any other university or institute for the award of any degree.

Navneet Kaur
Regn no. 902012008

Date: 13-10-2025

THAPAR INSTITUTE
OF ENGINEERING & TECHNOLOGY
(Deemed to be University)

Certificate

I hereby certify that the work presented in this thesis, entitled "**Study of calcium silicate glasses derived from agro-food wastes and minerals for biomedical applications**," submitted by **Navneet Kaur (Regn. no. 902012008)** in partial fulfillment of the requirements for the degree of **Doctor of Philosophy** in the Department of Physics and Material Science, Thapar Institute of Engineering and Technology, Patiala (Punjab), India, is a bona fide record of the candidate's own work carried out under my supervision and guidance. The matter embodied in this thesis has not been submitted in part or in full to any other university or institute for the award of any degree.

Dr. Kulvir Singh
Professor
Department of Physics and Material Science
Thapar Institute of Engineering and Technology
Patiala-147004, India

Acknowledgement

This thesis has been a profound learning journey, marked by both challenges and growth. Its completion would not have been possible without the unwavering support and encouragement of several individuals. I would like to express my heartfelt gratitude to all those who stood by me throughout this endeavor.

I am deeply thankful to my supervisor, **Dr. Kulvir Singh**, for his unwavering support, patience, and guidance throughout my Ph.D. journey. His vast knowledge and passion for research were essential in shaping this work, while his encouraging words and optimistic nature gave me strength during some of the most challenging phases. More than just a supervisor, he has been a mentor and a father figure—always there with wise counsel, kind support, and an open door. His constant belief in my abilities gave me the confidence to move forward, even when I doubted myself. I feel truly fortunate to have worked under his guidance. Thank you, Sir, for inspiring me, uplifting me, and helping me become a better researcher and a better person.

I am deeply grateful to **Prof. Padmakumar Nair**, (Director) and **Prof. Prakash Gopalan** (Former Director) of TIET for providing the institutional funding and resources essential for this research. My sincere thanks also go to **Prof. N. Tejo Prakash**, Dean of Research and Sponsored Projects, for the excellent research facilities. I also thank **Prof. O.P. Pandey** for his continued support and valuable guidance.

I express my sincere gratitude to **Dr. B.N. Chudasama** (Head, DPMS), **Dr. S.D. Tiwari** (Ph.D. coordinator) and my doctoral committee—**Dr. Loveleen K. Brar**, and **Dr. Devendra Kumar** for their constructive suggestions and critical feedback. I especially thank **Dr. Priyankar Dey** (Department of Biotechnology, TIET) for his invaluable collaboration, insights, and unwavering support. **Entire faculty and staff** of DPMS are acknowledged for helping me at different stages of my research.

I gratefully acknowledge the financial support of the **University Grants Commission (UGC)**, New Delhi, through the **Savitribai Jyotirao Phule Fellowship for Single Girl Child** (Award Letter No. F.No.82-7/200(SA-III)).

I am deeply indebted to my seniors, **Dr. Manmeet Kaur**, **Dr. Paramveer Kaur**, and **Dr. Trisha Walia**, for their valuable guidance during the initial stages of my research. I am especially grateful to **Dr. Shivani Punj**, whose support throughout this journey has been invaluable—not just as a senior but as a caring friend. I would also like to express my sincere gratitude to **Dr. S.S. Danewalia** for their insightful suggestions and feedback during the thesis writing process. My sincere appreciation goes to my colleagues, **Dr.Vimi Dua**, **Santosh Kumar**, **Vishavdeep Kaur**, **Rajni**, **Venu Chaudhary**, and **Manish Kumar**, for their support, encouragement and for making this journey more enjoyable.

This thesis is a testament to the unwavering love and support of my **family**. I am deeply indebted to my parents, who have always stood by me, encouraging me to reach new heights. My mother's constant belief in me gave me the wings to soar, and my father's unwavering support empowered me to dream big and pursue my goals. To my brothers and sisters-in-law, thank you for your constant presence and encouragement. And to my little sister, thank you for always being there, ensuring I never felt alone.

To my dear friends, your presence has made this Ph.D. journey brighter. **Manbir**, thank you for creating a home away from home and for always lifting my spirits. **Uma**, thank you for your timely check-ins and invaluable advice. **Bhavnoor**, thank you for your unwavering support, for listening patiently, for reminding me of my priorities, and for keeping me motivated during challenging times.

Finally, I express my deepest gratitude to the Almighty for the countless blessings bestowed upon me.

Navneet Kaur

Publications

Thesis work

1. **Navneet Kaur Mattu**, K. Singh, Structurally modified bioglasses synthesized using agro-food wastes and conventional sources for bone regeneration application, Ceramics International, (2023) 49 38910-38920. (**I.F.= 5.6**)

2. **Navneet Kaur Mattu**, K. Singh, Crystallization effect on structural, mechanical and cytotoxic properties of bioglasses synthesized using conventional and biowaste as resources, Materials Chemistry and Physics (2025) 331 130157. (**I.F.= 4.7**)

3. **Navneet Kaur Mattu**, Priyankar Dey K. Singh, K_2O effect on structural, hardness, and bioactivity of sodium calcium silicate bioglasses, Materials Chemistry and Physics (2025) 339 130719. (**I.F.= 4.7**)

4. **Navneet Kaur**, K. Singh, Decompositional and chemical reaction kinetics study of eggshell powder waste for value-added materials, Journal of Thermal Analysis and Calorimetry (2023) 148 6451–6463. (**I.F.= 3.2**)

5. **Navneet Kaur** and K. Singh, A comparative study of Raman spectroscopic and photoluminescence properties of the eggshell powder and conventional calcium carbonate, Journal of physics: conference series (2023). 2426 012001

6. **Navneet Kaur Mattu**, K. Singh, Non-isothermal crystallization kinetics study of Na_2O-K_2O-CaO-SiO_2 glasses derived from hybrid resources, Journal of Thermal Analysis and Calorimetry (Accepted). (**I.F.= 3.2**)

Other publications

1. Vageesh Kumar, Paramjyot Kumar Jha, Santosh Kumar, **Navneet Kaur Mattu**, K. Singh, Impact of CuO on physical, structural and optical properties of sodium-phosphate glasses, Ceramics International (2024) 50 39868-39877. (**I.F.= 5.6**)

2. Aamir Bashir, Paramjyot Kumar Jha, **Navneet Kaur Mattu**, Santosh Kumar, K. Singh, The network former/modifier behavior of CuO in Na_2O-P_2O_5 glasses, Ceramics International (2024) 50 50766-50773.(**I.F.= 5.6**)

3. Shivani Punj, **Navneet Kaur Mattu**, K. Singh, Manoj Baranwal, In-vitro and thermal stability study of bioglass synthesized from biogenic sources, Ceramics International (2024) 50 54513-54522. (**I.F.= 5.6**)

4. Jaspreet Kaur, **Navneet Kaur Mattu**, Isha Mudahar, K. Singh, Role of Sm_2O_3 on surface to bulk crystallization and thermal properties of Fe_2O_3-V_2O_5-B_2O_3-SiO_2 glasses, Journal of Non-Crystalline solids (2023) 610 122304. (**I.F.= 3.2**)

5. Shivani Punj, **Navneet Kaur Mattu**, K. Singh, Evolution of crystalline phases in glass matrix and their effect on optical and photoluminescent properties of silicate glasses derived from agro-food wastes Journal of Materials Science: Materials in Electronics 36 547. (**I.F.= 2.9**)

6. Manmeet Kaur Chhina, **Navneet Kaur Mattu**, K. Singh, Dy doped calcium silicates synthesized using agro-food wastes and conventional chemicals as resources: a comparative study, Hybrid Advances (2024) 7 100314.

Patent

1. "Non-toxic and cost-effective bioactive glasses formed using hybrid resources" Published on (16/08/2024), Application no. (202411056211 A)

Conferences attended

1. Oral presentation in International Conference on Current Trends in Physics and Photonics (ICCTPP-2022) organized by School of physics, Dr. Vishwanath Karad MIT World peace university, Pune, Maharashtra, India, that was held online during 9th to 11th June 2022.

2. Oral presentation in 6th National Conference on Advanced Materials and Radiation Physics (AMRP-2023) organized by Sant Longowal Institute of Engineering and Technology, Longowal, Distt. Sangrur-148106 (Punjab), India, that was held online during 18th-19th May 2023.

3. Poster Presentation in International Conference on Sustainable Development in Chemical and Environmental Engineering (SDCEE-2024) organized by Department of Chemical Engineering, TIET, Patiala held on February 22-24, 2024.

4. Poster Presentation in in the International Conference on Engineered Materials for Sustainable Development (EMSD 2024) jointly organized by Punjab Engineering College (Deemed to be University), Chandigarh and National Agri-Food Biotechnology Institute (NABI), Mohali held on July 24-26, 2024.

5. Poster Presentation in the National conference on Biotechnology, Biomanufacturing, and Bioeconomy (Bio3) organized by Department of Biotechnology, TIET, Patiala held on March 22-24, 2025

Abstract

The rapid expansion of the agricultural sector has led to a significant increase in agricultural waste. Crop residues such as corn, rice, sugarcane, and wheat are often openly burned, despite the detrimental environmental consequences. In addition to agricultural waste, a substantial portion of the food produced is also wasted and left to decompose without proper disposal mechanisms. From both environmental and energy perspectives, the most effective waste management strategy involves utilizing these wastes to synthesize value-added products. Rice husk ash (RHA) and eggshells (ES) are among the most abundant agro-food wastes and represent promising sources of SiO_2 and $CaCO_3$, respectively. These agro-food wastes/ashes/powders also contain magnesium, potassium, and other trace elements typically required for the production of bioglass and bioglass-ceramics. Furthermore, agro-food wastes offer sustainable and cost-effective alternatives to conventional precursors. This study focuses on the synthesis of bioglasses with a base composition of $43SiO_2$-$25CaO$-$25Na_2O$-$7P_2O_5$ (wt%) using biowaste-derived silica and calcium, supplemented with conventional precursors for P_2O_5, Na_2O, and MgO. The effects of systematically substituting CaO with MgO and Na_2O with K_2O were investigated. The resulting glasses and glass-ceramics were characterized to determine their physical, structural, thermal, and mechanical properties to assess their suitability as biomaterials. Bioactive properties were evaluated *in-vitro* using simulated body fluid (SBF). Furthermore, biocompatibility was assessed using the 3-(4,5-dimethylthiazol-2-yl)-2,5-diphenyltetrazolium bromide (MTT) assay in human peripheral blood mononuclear cells (PBMC). The thesis contains five chapters. The detailed summary of the chapters are given below.

Chapter 1 provides a basic understanding of biomaterials, with a specific focus on bioglasses and bioglass-ceramics, and the essential requirements for these materials to be considered as bioactive. It outlines various testing meth-

ods employed to assess the bioactivity of glasses and glass-ceramics, including a detailed explanation of the hydroxyapatite (HAp) layer formation mechanism on the material surface upon immersion in SBF. The biocompatibility testing methods are also given in brief. The MTT assay is a reliable method. It is directly related to the number of viable (living) cells introduced to test the biocompatibility of bioglass/bioglass-ceramics. Further, the potential agro-food wastes and their constituents are also discussed in this chapter.

Chapter 2 presents a comprehensive review of the existing literature on sustainable bioactive glasses, with a particular emphasis on the utilization of agro-food waste as a precursor source. The review explores the potential of various agro-food wastes, including RHA and ESP, as sustainable alternatives to conventional chemicals in bioactive glass synthesis. Different processing techniques for extracting valuable minerals from these waste sources are examined, along with a discussion of various synthesis methods employed for producing bioactive glasses and glass-ceramics. The review analyzes the crucial structure-property relationships in these materials, highlighting the influence of composition and processing parameters on bioactivity, biocompatibility, and mechanical properties. Furthermore, the *in-vitro* and *in-vivo* performance of agro-food waste-derived bioactive glasses in various biomedical applications is critically evaluated. The effects of MgO and K_2O on the bioactive properties of different bioglasses and bioceramics are also discussed. Finally, based on this comprehensive literature survey, the motivation and specific objectives of the present study are outlined in the last of the chapter.

Chapter 3 details the synthesis of two glass series based on the nominal composition $43SiO_2$-$25CaO$-$25Na_2O$-$7P_2O_5$ (wt%). The first series involved the systematic substitution of CaO with MgO, resulting in the compositions $43SiO_2$-$25Na_2O$-$7P_2O_5$-(25-x)CaO-xMgO (where x = 0, 5, 10, and 15 wt%). The second series involved the substitution of Na_2O with K_2O, yielding the compositions $43SiO_2$-$25CaO$-$7P_2O_5$-(25-y)Na_2O-yK_2O (where y = 0, 5, 10, and 15 wt%). Both glass series were synthesized via the melt-quench method using platinum-rhodium (Pt-Rh) crucibles. The chemical compositions of the as-synthesized samples were evaluated using energy-dispersive X-ray spectroscopy

(EDS). Density measurements were performed using the Archimedes principle. Structural and thermal characterization included X-ray diffraction (XRD), Fourier-transform infrared spectroscopy (FTIR), and differential thermal analysis (DTA). Microhardness and fracture toughness, a key mechanical property, was determined using a Vickers hardness tester. *In-vitro* bioactivity was assessed by immersing the glass samples in simulated body fluid (SBF) for various time periods (2, 5, 10, 20, and 40 days). Weight changes of the samples and pH changes of the SBF solution were monitored. The immersed samples were further characterized using XRD, FTIR, scanning electron microscopy (SEM), field emission scanning electron microscopy (FESEM) with EDS, and microwave plasma atomic emission spectroscopy (MP-AES) to investigate the physicochemical reactions occurring on the glass surface. Biocompatibility of the as-synthesized glasses was evaluated using the MTT assay on human peripheral blood mononuclear cells (PBMCs). Cell viability was measured using an ELISA microplate reader.

Chapter 4 presents the results obtained from the characterization of the synthesized calcium silicate glasses and glass-ceramics, followed by a detailed interpretation and discussion. The chapter is structured into four sections. The first section compares the properties of eggshells (ESP) as a calcium source with conventional $CaCO_3$. The second section details the results and discussion for the first glass series, 43SiO_2-25Na_2O-7P_2O_5-(25-x)CaO-(x)MgO (where x = 0, 5, 10, 15 wt%). The third section investigates the effects of K_2O substitution for Na_2O in the control glass composition, focusing on the series 43SiO_2-25CaO-7P_2O_5-(25-y)Na_2O-(y)K_2O (where y = 0, 5, 10, 15 wt%). The fourth section compares the properties of the hybrid source derived glasses (derived from RHA, eggshells, and conventional chemicals) with their counterparts synthesized using only conventional precursors. The influence of MgO substituting for CaO and K_2O substituting for Na_2O is comprehensively studied using various characterization techniques. MgO substitution in the the glasses composition resulted in increased phase separation. Also, MgO plays a dual role, acting as both a network former (increasing polymerization within the silicate network) and a modifier in the phosphate network. On the other hand, K_2O substitution

enhanced structural homogeneity and promoted the conversion of non-bridging oxygens (NBOs) to bridging oxygens (BOs), leading to a higher proportion of odd-numbered Q^n (n= 1,3) structural units. Both MgO and K_2O substitutions widened the sintering window and improved thermal stability, with thermal expansion coefficient (TEC) suitable for biomedical coatings. Both modifiers increase the hardness as compared to base glass. The mixed modifier effect is also recorded in both series, exhibiting a non-linear trend through the different properties of glasses, as well as in *in-vitro* testing. *In-vitro* bioactivity tests revealed that all glasses formed carbonated hydroxyapatite (c-HAp). However, MgO substitution delayed c-HAp formation and Si^{4+} release while simultaneously improving cytocompatibility. Conversely, K_2O substitution accelerated c-HAp formation, with SNK-15 (15 wt% K_2O) showing the highest bioactivity, but reduced cytocompatibility over time due to increased ion leaching. Compared to their hybrid source derived counterparts, conventionally derived glasses displayed higher density and hardness, more rapid and stable c-HAp formation, but lower fracture toughness and reduced cytocompatibility. The base glass, SC-0 (no MgO or K_2O substitution), demonstrated the most favorable balance of bioactivity and biocompatibility.

Chapter 5 concludes the study by analyzing the results presented in Chapter 4. The substitution of MgO for CaO decreases bioactivity while increasing hardness. Conversely, substituting K_2O for Na_2O in the base glass reduces phase separation and enhances bioactivity. To validate these findings from hybrid-source glasses, comparative glasses were synthesized using conventional melt-quench techniques with pure chemicals. Results showed that hybrid-source glasses exhibited better bioactivity and biocompatibility compared to conventionally synthesized glasses. However, conventional glasses demonstrated better hardness and other physical properties. Ultimately, the hybrid approach is considered advantageous due to its cost-effectiveness and sustainability. The chapter concludes by outlining future research directions stemming from this study.

Abbreviations

ATP	Adenosine triphosphate
BCP	Biphasic calcium phosphate
BOs	Bridging oxygens
bSNPs	Biogenic silica nanoparticles
CAGR	Compound annual growth rate
Ca-P	Calcium phosphate
CBG	Conventional bioglass
CC	Coconut cell
CH	Corn husk
CHA	Corn husk ash
c-HAp	Carbonated hydroxyapatite
c-SBF	Conventional SBF
DCPD	Dicalcium hydrogen phosphate dihydrate
DMSO	Dimethyl sulfoxide
DMEM	Dulbecco's Modified Eagle's Medium
DTA/TGA	Differential thermal analysis / Thermogravimetric analysis
EDS	Energy dispersive spectroscopy
ESM	Eggshell membrane
ESP	Eggshell powder
FESEM	Field emission scanning electron microscopy
FTIR	Fourier transform infrared spectroscopy
FA	Folic acid
FWHM	Full width at half maximum
gf	Gram force
HAp	Hydroxyapatite
h	Hours
hBMSCs	Human bone marrow stromal cells

hLFCs	Human lung fibroblast cells
HOB	Human osteoblasts cells
ICP-OES	Inductively coupled plasma-optical emission spectroscopy
MAE	Mixed alkali effect
MBG	Mesoporous bioglass
MP-AES	Microwave Plasma Atomic Emission Spectroscopy
m-SBF	modified-Simulated body fluid
MTT	3-(4,5-Dimethylthiazol-2-yl)-2,5 diphenyl tetrazolium bromide
N-HAp	Nanocrystalline HAp
NBOs	Non-bridging oxygens
OPD	Oxygen packing density
PBMC	Peripheral blood mononuclear cells
PBS	phosphate buffered solution
PCL	Polycaprolactone
PE	Polyethylene
PEG	Polyethylene glycol
pH	Potential of hydrogen
PPB	Parts per billion
PS	Peanut shells
Pt-Rh	Platinum-Rhodium
r-SBF	Revised SBF
RHA	Rice husk ash
RH	Rice husk
R-SBgC	Rice husk silica based bioactive glass-ceramics
rMBG	Rice husk derived mesoporous bioglass
SAOS-2	Sarcoma osteogenic osteoblast-like cells
SBF	Simulated body fluid
SCB	Sugarcane bagasse
SCLA	Sugarcane leaves ash
SCL	Sugarcane leaves
SEM	Scanning electron microscope
TEC	Thermal expansion coefficient

$\mathbf{T}_g$	Glass transition temperature
$\mathbf{T}_c$	Glass crystallization temperature
$\mathbf{T}_s$	Glass softening temperature
TTCP	Tetracalcium phosphate
wt%	Weight percentage
WSA	Wheat straw ash
XRD	X-ray diffraction
β**-TCP**	β-Tricalcium phosphate

Table of Contents

List of Tables

List of Figures

CHAPTER 1

Bioactive glasses: Classifications, applications and sustainable synthesis

Overview

This chapter provides a foundational overview of biomaterials and their diverse applications in modern medicine and healthcare. The main focus is on bioactive glasses and glass ceramics, a unique class of biomaterials with significant potential for tissue regeneration and repair. Key compositional modifications of bioactive glasses and their effect on bioactive properties are explored, highlighting how these variations can tailor material properties to meet specific clinical needs. Further, the mechanism to test the bioactivity and biocompatibility are discussed. Finally, the chapter introduces the concept of sustainable biomaterial synthesis using agro-food waste, setting the stage for further exploration of this promising area.

1.1 Biomaterials: An introduction

Biomaterials, encompassing natural and synthetic materials, are designed to interface with biological systems, replacing, supporting, or enhancing tissues and organs of living body [1][2][3][4]. These materials are used in a wide range of applications, from simple wound dressings and bone plates to complex devices like pacemakers and artificial hearts. A critical requirement for biomaterials is their ability to remain in contact with living tissues and body fluids for extended periods without causing adverse reactions in human body [5]. This biocompatibility is achieved by mimicking aspects of living tissues, such as surface topography, porosity, and mechanical properties, ensuring a neutral response from the living body, free from inflammation or immune rejection.

The specific requirements for a biomaterial are dictated by its intended medical application. Implantable biomaterials, for instance, must meet more stringent criteria than those designed for external or temporary use. Major properties include biocompatibility, bioactivity, mechanical strength, and biodegradability [6][7]. As illustrated in **Fig. 1.1**, these properties are fundamental for ensuring long-term implant stability, functionality, and ultimately, patient well-being. Biocompatibility allows for harmonious coexistence with surrounding tissues, while bioactivity enables the materials to actively participate in biological processes like tissue regeneration. Mechanical strength is essential for withstanding physiological stresses, and biodegradability allows for controlled breakdown and absorption, especially crucial for temporary implants or scaffolds.

The biomaterials market is showing rapid growth, driven by the increasing demand for advanced healthcare solutions and the transformative impact of biomaterials on human health and longevity [7][8]. This growth, projected to reach a compound annual growth rate (CAGR) of 12.6% by 2032 from a market size of $123.8 billion in 2023, highlights the increasing integration of biomaterials in diverse medical devices, from heart valves and stents to joint replacements. Within this rapidly expanding field, bioactive glasses and glass-ceramics have emerged as a prominent area of interest due to their unique

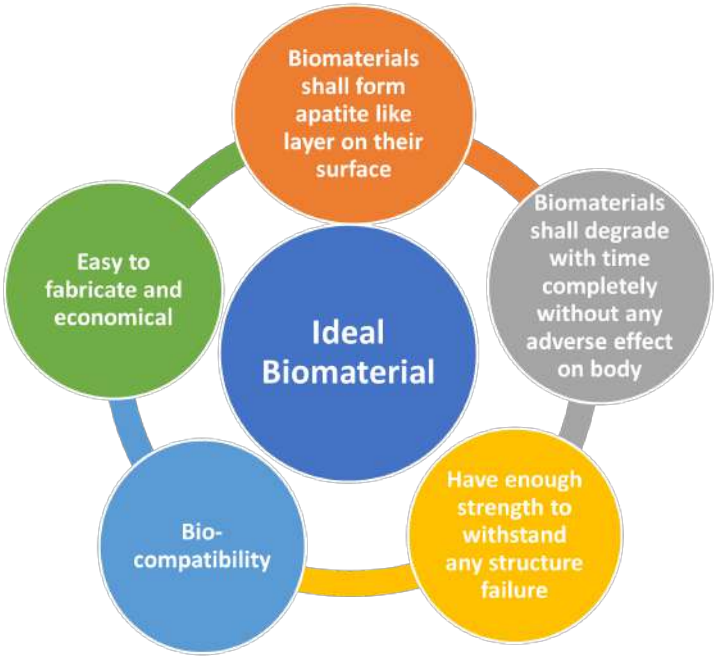

Figure 1.1: Essential properties required for an ideal biomaterial

potential in bone regeneration and tissue integration. This focus on bioactive glasses and glass-ceramics stems from their remarkable properties and ability to seamlessly integrate with living tissues, driving a significant increase in demand. Indeed, the market for these materials is now estimated to exceed 1.5 million units annually, with a value approaching $10 billion [6][7]. The choice of biomaterial, whether metal, polymer, ceramic, or composite, depends critically on the specific application and its functional requirements, underscoring the importance of ongoing materials science innovation in addressing the evolving challenges of medicine and healthcare. The following sections will delve deeper into the specific properties and applications of bioactive glasses and glass-ceramics, emphasizing their synthesis from sustainable resources.

1.2 Classification of biomaterials: Based on biocompatibility

Biocompatibility, a material's ability to harmoniously interact with the body, dictates its integration with tissues and is crucial for success in specific applications. Biomaterials are classified into three generations based on their tissue interaction [3][9], as summarized in **Table 1.1**.

1.2.1 Bio-inert

Bio-inert materials represent the first generation of biomaterials and were designed to have minimal interaction with surrounding biological tissues when implanted into the body. These materials exhibit high chemical durability and resist degradation, maintaining their structural integrity in physiological environments. Due to their inert nature, they do not actively engage with the tissues and are often encapsulated by a fibrous layer of non-adherent tissue. Common examples of bio-inert materials include alumina (Al_2O_3), zirconia (ZrO_2), zirconia-toughened alumina (Zr-Al_2O_3), and yttria (Y_2O_3)[10]. The alloys and metals, such as stainless steel and titanium and their alloys, are widely used in orthopedic and dental applications due to their excellent mechanical properties, corrosion resistance, and stability in both acidic and basic conditions. However, while bio-inert materials provide structural support, they do not integrate with the surrounding tissue and, in some cases, may lead to complications such as implant displacement or loosening strength over time [11].

1.2.2 Bio-active

The development of second-generation biomaterials in the 1970s marked a shift toward materials designed to stimulate specific biological responses at the interface with living tissues. This interaction promotes the formation of a strong bond between the material and surrounding tissue [5]. As a result, these biomaterials are referred to as bioactive due to their controlled reactions within the physiological environment. Examples of these bioactive materials include crystalline calcium phosphates, bioactive glasses, and bioactive glass ceramics. Clinically, these materials are widely used in applications such as bone regeneration, tissue augmentation, and as coatings on metallic implants to improve their integration with bone and enhance healing processes [2].

1.2.3 Bio-resorbable/Bio-degradable

Bio-resorbable/bio-degradable biomaterials represent the third generation of biomaterials, developed in the 2000s. Unlike other materials, which are unable

to adapt to physiological load changes or biochemical stimuli, bio-resorbable biomaterials are designed to mimic the dynamic nature of living tissues [12]. This characteristic allows them to support the body's healing processes while gradually degrading over time. As the biomaterial is absorbed, it is replaced by natural tissue, thus enhancing the repair and regeneration of damaged areas. The development of these materials addresses the limitations of traditional artificial implants, providing a more biologically integrated approach to tissue repair and regeneration [13]. Nearly all calcium phosphates act as bio-resorbable materials. One of the important advantages of calcium phosphate biomaterials is that their dissolution products can be easily assimilated by the human body.

Table 1.1: Classifications of biomaterials and their type of bonding with the human body

Biomaterials	**Type of bonding**	**Example**
First (Bio-inert)	Mechanical interlock	Metals, alumina, zirconia, polyethylene
Second (Bio-active)	Interfacial bonding with tissues	Bioactive glasses-glass ceramics, Hydroxyapatite (HAp)
Third (Bio-resorbable)	Replacement with tissues	Calcium Phosphates, poly-lactic acids

However, before the clinical implantation of any biomaterial, it is crucial to carefully evaluate its biocompatibility and their performance. Thorough testing is required to ensure that these materials not only interact with tissues as intended but also exhibit the necessary safety, efficacy, and longevity within the body. This evaluation process necessitates an approach involving various testing methodologies, as discussed in the following section.

1.3 Biomaterials and their testing

Before implantation or use in human clinical applications, biomaterials must undergo thorough testing outside the living body. Various testing methodologies, including in-silico, in-vitro, and in-vivo, are utilized for this purpose. These preclinical tests are crucial for predicting how the material will interact with the complex biological environment of the human body and for identi-

fying potential risks or limitations of the biomaterials. Such evaluations help ensure the safety, efficacy, and reliability of the biomaterial before clinical trials commence.

1.3.1 In-silico

In-silico testing, performed through computer simulations, is increasingly contributing to the biomedical field by predicting the behavior of pathogens, genes, and drugs within the human body. This approach allows for the rapid screening of therapeutic interventions, reducing the need for extensive physical trials and helping to streamline drug development. Additionally, it provides insights into complex biological interactions, accelerating the design of personalized medicine and improving patient health [14].

1.3.2 In-vitro

In-vitro testing is a critical step in the development and evaluation of biomaterials for potential clinical applications. These tests enable researchers to investigate the interactions of biomaterials with cells, tissues, and other biological components under controlled laboratory conditions. This provides an initial understanding of a material's biocompatibility, cytotoxicity, and bioactivity [15].

The success of tissue engineering strategies depends on the ability to recreate or mimic the conditions of the healthy tissue. In-vitro tests, despite their usefulness, often lack the complexity of the human body, which includes a dynamic and multifaceted environment influenced by mechanical stimuli, vascularization, immune responses, and cellular interactions. For instance, in-vitro cytotoxicity tests provide valuable insights into immediate cell-material interactions, but they do not account for long-term responses such as chronic inflammation, degradation kinetics, or the material's behavior under physiological stresses. In-vitro methods cannot capture all complexities in the body during in-vivo tests as discussed in the following section. Despite these limitations, in-vitro testing remains an indispensable part of the evaluation process for medical devices, including implants. These tests precede in-vivo studies

because they serve as valuable indicators of how newly developed biomaterials might behave when in contact with living tissue [16].

For biomaterials such as ceramics and bioactive oxide glasses, in-vitro testing typically involves cytotoxicity assays, such as the (3-(4,5-dimethylthiazol-2-yl)-2,5-diphenyl-2H-tetrazolium bromide) MTT assay, to assess the material's effects on cell viability and proliferation during degradation. Additionally, bioactivity is often evaluated by immersing the materials in different immersion mediums such as simulated body fluid (SBF), tris-buffered solution, and phosphate-buffered solution to observe both material degradation, and the formation of a hydroxyapatite (HAp)-like layer on their surface. This layer indicates the material's potential for bonding with bone tissue [17]. Before the development of SBF, in-vitro tests were conducted using distilled water or Tris buffer solution. The SBF solution synthesized by Kokubo et al. [18] mimics human blood plasma, with ionic concentrations more or less similar to those found in plasma (as given in **Table 1.2**).

Table 1.2: Ionic concentration of human body plasma and SBF

	Na^+	K^+	Mg^{2+}	Ca^{2+}	HCO_3^-	Cl^-	HPO_4^{2-}	SO_4^{2-}
Plasma	142.0	5.0	1.5	2.5	103.0	27.0	1.0	0.5
SBF	142.0	5.0	1.5	2.5	147.8	4.2	1.0	0.5

For the synthesis of SBF during in-vitro studies, the pH of the solution is maintained between 7.25-7.4 at normal body temperature (37°C). Since Kokubo's innovation of SBF, several variations, such as revised SBF (r-SBF), modified SBF (m-SBF), and conventional SBF (c-SBF), have been proposed to evaluate the in-vitro bioactivity of different materials [19]. Despite these alternatives, Kokubo's protocol remains widely used for testing in-vitro bioactivity. The SBF method is an efficient way to assess the bioactivity of materials like glasses and glass-ceramics [20][21], particularly for monitoring the formation of hydroxyapatite (HAp) on their surfaces. However, the bioactivity and HAp formation are highly dependent on the material's composition, processing parameters and their properties. For example, silicate-based bioactive glasses and glass-ceramics, including diopside-based ceramics ($Ca_2MgSi_2O_6$), have demon-

strated excellent apatite-forming abilities in SBF [22]. Thus, the in-vitro bioactivity of these glasses and glass-ceramics can often be reliably inferred from their reaction in SBF [18][23]. In addition to this, various important immersion conditions, such as surface-to-volume ratio, static or dynamic setups, and the structure of the test samples, play a crucial role in validating the accuracy of in-vitro bioactivity tests. Additionally, in-vitro methods using tissue or cell cultures are also employed to assess the biocompatibility of bioactive glasses and glass ceramics.

1.3.3 In-vivo

In-vivo testing is performed within living organisms under controlled physicochemical conditions to observe biological responses in a natural environment. It is most commonly applied in animal testing to evaluate safety, efficacy, and potential side effects before proceeding to clinical trials involving human participants. This method provides valuable insights into the interactions between biomaterials and complex biological systems, helping to ensure the material's suitability for clinical biomedical applications [24]. The present work is focused on the development of bioactive glasses, so the detailed mechanism of in-vitro testing are given in the following section.

1.4 Formation of hydroxyapatite in in-vitro

In-vitro testing of biomaterials such as bioactive glass and glass-ceramics focuses on the formation of a HAp layer on the material's surface upon interaction with SBF. This HAp layer, specifically its carbonated form (HCA or c-HAp), is crucial for bonding with bone tissue due to its similarity to bone's mineral composition [18].

The process begins when the glass surface comes in contact with SBF, initiating a series of chemical reactions. These reactions can be broadly categorized into leaching, dissolution, and precipitation [25][26]. Initially, alkali and alkaline earth metal ions (e.g., Na^+, K^+) from the glass network exchange with hydrogen and hydronium ions (H^+ and H_3O^+) from the SBF, increasing the solution's pH level >7, resulting in increased basicity of the solution. This

process is relatively easy because these ions function as modifiers in the glass network and are only weakly bonded to the network [27]. Further, the ion exchange reaction weakens the glass network, making it susceptible to dissolution. Hydroxyl ions (OH^-) then attack and break down the silica network ($-Si-O-Si-O-Si-$) of glasses and glass ceramics, releasing silicic acid ($Si(OH)_4$) into the solution. The release of the silica into the solution is highly dependent on the composition of the glass. [24][27].

Subsequently, the silicic acid undergoes polycondensation, forming a silica-rich gel layer on the glass surface. Calcium (Ca^{2+}) and phosphate (PO_4^{3-}) ions from the glass and the SBF then migrate to this silica-rich layer, precipitating and forming an amorphous calcium-phosphate (Ca-P) layer. Finally, carbonate ions (CO_3^{2-}) from the SBF incorporate into the Ca-P layer, leading to the crystallization of a c-HAp layer. The time required for HAp formation varies based on factors such as the material's composition, ion exchange rate, hydroxylation, and solution pH. Hench *et al.* [27] have detailed a five-step reaction sequence for c-HAp layer formation on glass surfaces, as given below [8][28] and shown in **Fig. 1.2**:

- **Ion exchange:** Rapid exchange of alkali or alkaline earth metal ions (Na^+, K^+) with H^+ or H_3O^+ from the solution.

$$Si-O-Ca^{2+}+H^+ \rightarrow Si-OH^- + Ca^{2+} \tag{1.1}$$

- **Dissolution of silica:** Hydroxyl ions break $-Si-O-Si-$ bonds, forming silanols (Si-OH^-).

$$Si-O-Si+H_2O \rightarrow 2Si-OH \tag{1.2}$$

- **Silica re-polymerization**: Condensation of Si-OH^- groups forms a silica-rich layer.

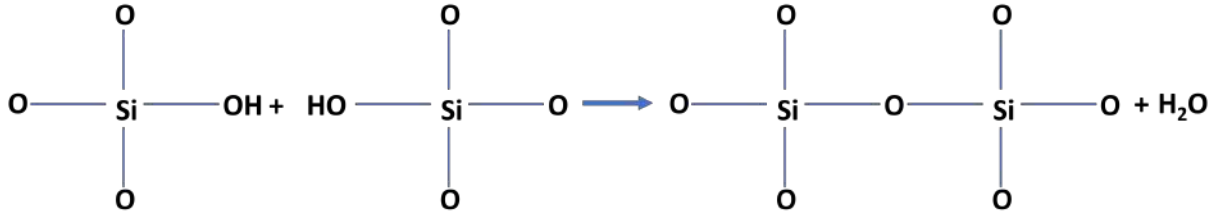

- **Ca-P layer formation:** Ca^{2+} and PO_4^{3-} migrate to the surface and form an amorphous Ca-P film.
- **HAp crystallization:** Incorporation of OH^-, CO_3^{2-}, or F^- and crystallization of the Ca-P layer into c-HAp or fluorapatite.

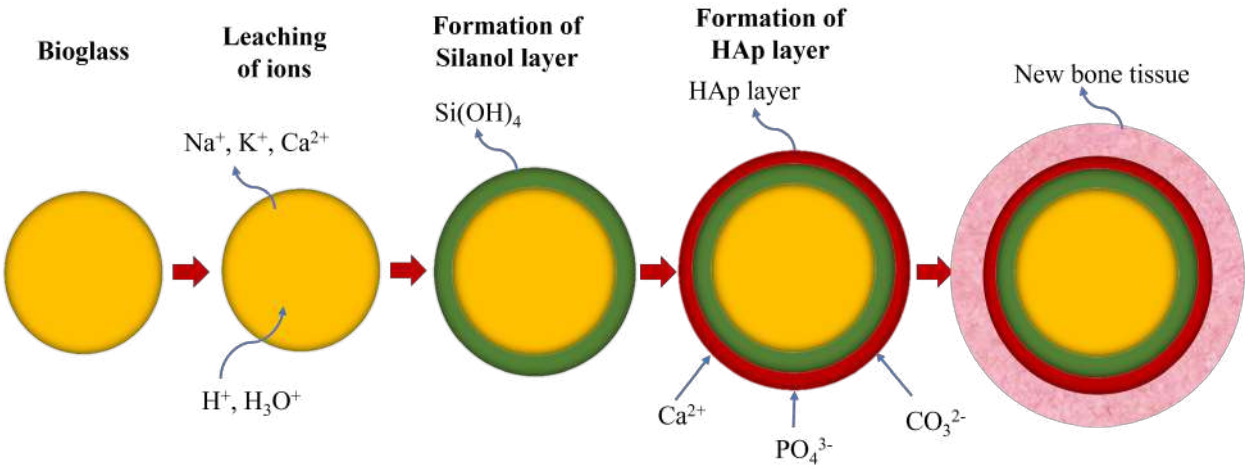

Figure 1.2: Mechanism of bioactive glass surface modification in response to SBF

While the initial five steps of bioactive glass interaction—ion exchange, network breakdown, silica re-polymerization, Ca-P layer formation, and HAp crystallization occur independently of the surrounding tissues, they are essential prerequisites for subsequent tissue integration. The resulting c-HAp layer provides a scaffold for the next stage of biological interaction, which involves a cascade of reactions (steps 6-11), which include cell colonization, proliferation, and differentiation to form new bone with good mechanical bond to the implant surface [27]. These biological processes include cell colonization, proliferation, and differentiation, ultimately leading to the formation of osteoblasts and the growth of new bone tissue firmly bonded to the implant surface. Bioactive glass's effectiveness in regenerating soft tissues and hard tissues is intrinsically linked to the glass's structural properties and chemical composition as discussed in the following sections.

1.5 In-vitro cytotoxicity of bioactive glasses

While in-vivo testing provides the most comprehensive assessment of biomaterial performance within a living organism, in-vitro methods offer valuable

preliminary insights and reduce the reliance on animal testing. In-vitro, cytotoxicity tests are particularly crucial for evaluating the biocompatibility of newly developed biomaterials like bioactive glass/glass ceramics [29][30]. These tests offer rapid, standardized protocols, generating comparative data that can identify and eliminate toxic materials early in the development process.

The most common in-vitro biocompatibility test utilizes cell cultures to assess various aspects of cell behavior, including cytotoxicity, proliferation, adhesion, and death. Cultured human and animal cells provide a controlled environment for evaluating the material's effects on cell viability and function. These studies are often referred to as cytocompatibility tests when focusing on one or two specific cell types [31]. Several methods exist for exposing cells to the test materials. In direct contact tests, the cells are cultured directly on the bioglass surface. Indirect contact tests employ an agar layer or filter between the cells and the material, while elution tests expose cells to the dissolution products released by the bioglass into the culture medium [15].

The choice of cell type significantly impacts the assay's performance and depends on the specific assay being performed as well as the laboratory's capabilities. Both primary cells and established cell lines can be used, derived from various tissues and organisms (animal or human). The selection of appropriate cell types for in vitro testing is guided by the intended application of the biomaterial [31]. For example, when evaluating a material designed for bone regeneration, human osteoblast cell (HOB) lines are commonly used. Osteoblasts, the single-nucleus bone-forming cells responsible for synthesizing and depositing HAp within the organic matrix, play a vital role in building strong, dense bone tissue [32].

Another important parameter is the time duration of the cell culture. While many tests are conducted over 24 hours, slower-growing cells like HOBs often require longer culture periods, ranging from 3-7 days. In these cases, cell proliferation and spreading assays, frequently performed using 96-well plates, are employed to assess the biomaterial's influence on cell growth. One such assay, the MTT (3-(4,5-Dimethylthiazol-2-yl)-2,5 diphenyl tetrazolium bromide)

assay, is a sensitive and reliable colorimetric method used to quantify cell proliferation, viability, and cytotoxicity [15].

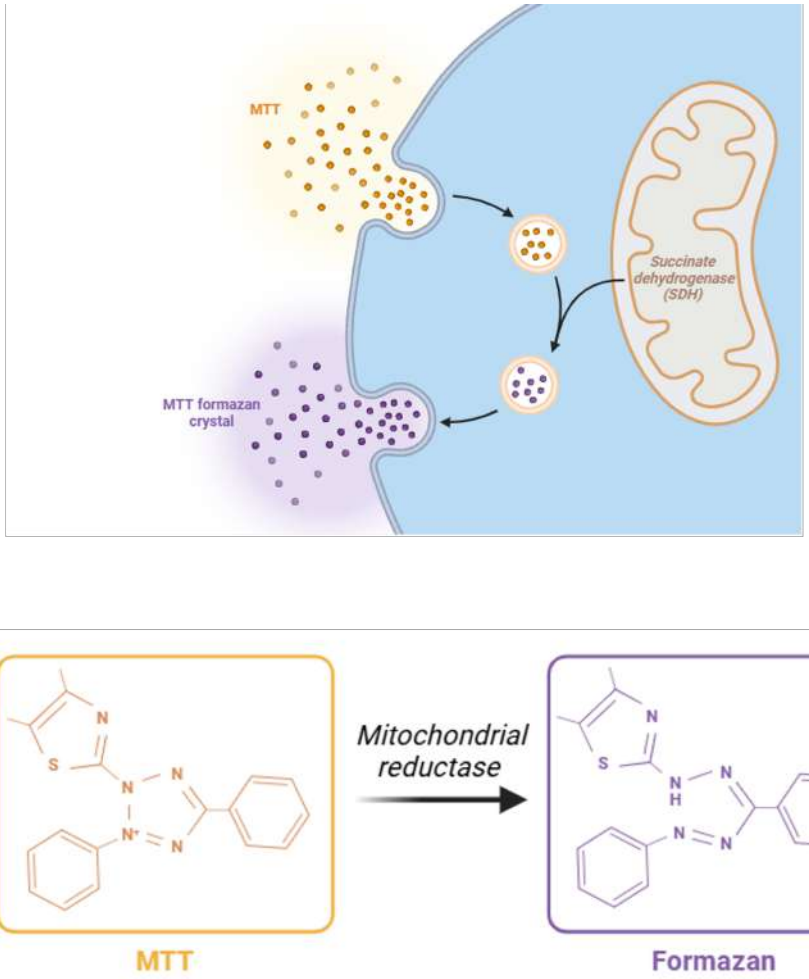

Figure 1.3: Principle of the MTT assay, a common method for assessing cell viability

The MTT assay provides a quantitative measure of cell viability, a key indicator of biomaterial cytotoxicity. In this assay, viable cells with active mitochondria reduce the yellow tetrazolium MTT salt to an insoluble purple formazan product by metabolically active cells. This reaction, catalyzed by succinate dehydrogenase, leads to formazan accumulation within the cells. **Fig. 1.3** illustrates the principle of the MTT assay, a common method for assessing cell viability. This color change, measured spectrophotometrically, provides a direct indication of the number of viable cells. Adding a solvent such as spectrophotometric grade dimethylsulfoxide (DMSO) or isopropanol dissolves the formazan, enabling colorimetric quantification, which directly corresponds to the number of viable cells. Cytotoxicity is then calculated as the ratio of viable

cells to the total number of cells initially seeded. A biomaterial is generally considered cytocompatible if cell viability exceeds 70%. Since cytotoxicity is a primary concern for biomaterials intended for in-vivo use, the MTT assay plays a crucial role in assessing their safety. Furthermore, the MTT assay can reveal the impact of a biomaterial's structure on cell behavior, as ion release and subsequent pH changes can influence cell attachment, proliferation, and growth [15][32].

1.6 Bioactive glass and glass-ceramic: Properties and applications

Following the discussion of biomaterials and their classification, this section focuses specifically on bioactive glass and glass-ceramic as a unique class of biomaterials. As discussed in the above sections, ceramics and bioactive glass-based biomaterials form a specialized category of biomaterials that have a profound positive impact on human beings [2][33][34]. The term "bioactive glass" refers to glass materials that are non-carcinogenic, non-antigenic, and compatible with surrounding tissues [7]. Bioactive glasses and ceramics offer superior biocompatibility, along with anti-corrosion and anti-compression properties, and possess composition flexibility that allows for tailored medical applications. Typically, these materials are brittle and mechanically strong, with elastic moduli similar to human bone. These materials are considered advanced materials for bone tissue engineering due to their ability to promote osteoprogenitor differentiation, enhance enzyme activity, support osteoblast cell adhesion, and aid in revascularization, making them ideal for bone regeneration and repair [6].

1.6.1 45S5 Bioglass®: A pioneering bioactive material

The second-generation biomaterial, bioactive glass known as "45S5 Bioglass®" was first designed by Hench in 1969. The 45S5 Bioglass contains 45% SiO_2-24.5% CaO-24.5% Na_2O-6% P_2O_5 in wt% [35]. This glass demonstrates a positive response in living bone by triggering osteogenesis through the release of biologically active ions. The bioactivity of the glass can range from surface

bioactivity to bulk degradability, allowing it to be resorbed within 10 to 30 days in tissue. The invention of Bioglass® revolutionized biomaterials development and led to the creation of doped bioactive glass systems for human being betterment. While ancient civilizations utilized biomaterials for reconstructing damaged body parts, Bioglass® has been in clinical use since 1985, particularly in dental applications, such as NovaMin and Perioglass [6][36].

1.6.2 Compositional modifications and diverse applications

Bio-active materials, by definition, are designed to induce target-specific biological responses. A key advantage of bioactive glasses, which has attracted significant attention from researchers, is that even small changes in their chemical composition can lead to substantial changes in their properties. The performance of bioactive glass depends on its composition and structure. For instance, Hench's 45S5 glass is a silicate (SiO_2)-based glass having short-range order ($\sim$ 3.4 Å) with alkali and alkaline ions such as calcium (CaO) and sodium (Na_2O) as modifiers and phosphorus pentaoxide (P_2O_5) as another glass network former oxide. The presence of a SiO_2 network promotes the formation of an HAp layer, which is essential for bonding with bone. The CaO and P_2O_5 release stimulates osteogenesis, while Na_2O enhances degradation, making it ideal for rapid bone boding and repairing [37].

Since the invention of bioglass, researchers have explored various compositional modifications to tailor bioactive glasses for specific applications. **Table 1.3** presents some examples of these modifications derived from the original 45S5 bioglass [4][38][39]. Modified bioactive glasses such as 13-93, 45S5F, and 58S are also employed in various biomedical applications, including dental repairs, knee replacements, and middle ear bone reconstruction, benefiting millions of patients worldwide. These advancements in bioactive glass compositions not only enhance their therapeutic potential but also make them attractive candidates for producing scaffolds used in bone regeneration [2][4][8][38][39].

Bioactive glasses, categorized as class A or class B based on composition, offer a versatile platform for biomedical applications. Class A bioglasses, primar-

Table 1.3: Chemical composition of bioactive glasses synthesized by modifications in 45S5 bioglass composition

bioactive glasses	SiO_2	CaO	NaO_2	P_2O_5	K_2O	B_2O_3	MgO	CaF_2	Ref.
45S5	45.0	24.5	24.5	6.0	—	—	—	—	[4]
13-93	53.0	20.0	6.0	4.0	12.0	—	5.0	—	[4]
45B15S5	30.0	24.5	24.5	6.0	—	15.0	—	—	[4]
$\mathbf{P_{50}C_{35}N_{15}}$	—	19.7	9.3	71.0	—	—	—	—	[4]
45B5S5	40.0	24.5	24.5	6.0	—	5.0	—	—	[4]
70S30C	71.4	28.6	—	—	—	—-	—	—	[4]
58S	58.2	32.6	—	9.2	—	—	—	—	[4]
6P53B	52.7	18.0	10.3	6.0	2.8	—	10.2	—	[4]
45S5F	43.0	12.0	23.0	6.0	—	—	—	16.0	[40]
45S5-C	50.0	19.5	24.5	6.0	—	—	—	—	[41]

ily composed of SiO_2, CaO, and Na_2O, with potential additions of P_2O_5, CaF_2, or B_2O_3, exhibit high bioactivity, readily forming a hydroxyapatite (HAp) layer upon interaction with body fluids, leading to strong bonding with bone tissue. This controlled degradation and ion release stimulate bone regeneration, making them suitable for bone regeneration, tissue engineering, and dental restorations. Conversely, class B bioglasses, with higher silica content (over 60 wt%) show only osteoconductive properties and often incorporate biocompatible minerals like fluorapatite or wollastonite, are generally bio-inert, lacking the inherent ability to bond with bone. However, their structural stability and potential for composite formation, where bioactive phases can be integrated, make them valuable components in various biomedical applications [42].

Notably, research has revealed that modifying the composition of bioactive glasses, such as replacing Ca^{2+}, Na^{+} or creating phosphate-free variations, can significantly alter their properties and bioactivity. For instance, incorporating MgO can enhance mechanical properties, thermal properties, biocompatibility, and biodegradability, while the addition of Al_2O_3 or B_2O_3 can influence surface reactions and formation of glasses, particularly reduces the melting temperature of the glass composition [43][44]. Further tailoring of bioactivity and antimicrobial properties can be achieved by incorporating ions like Sr^{2+}, Cu^{2+}, Ag^{+}, Zn^{2+}, and F^{-}. This compositional flexibility highlights the adaptability of bioactive glasses for diverse biomedical applications, emphasizing the im-

portance of understanding the interplay between composition, structure, and bioactivity for optimized functionality [2][45][46][47][48].

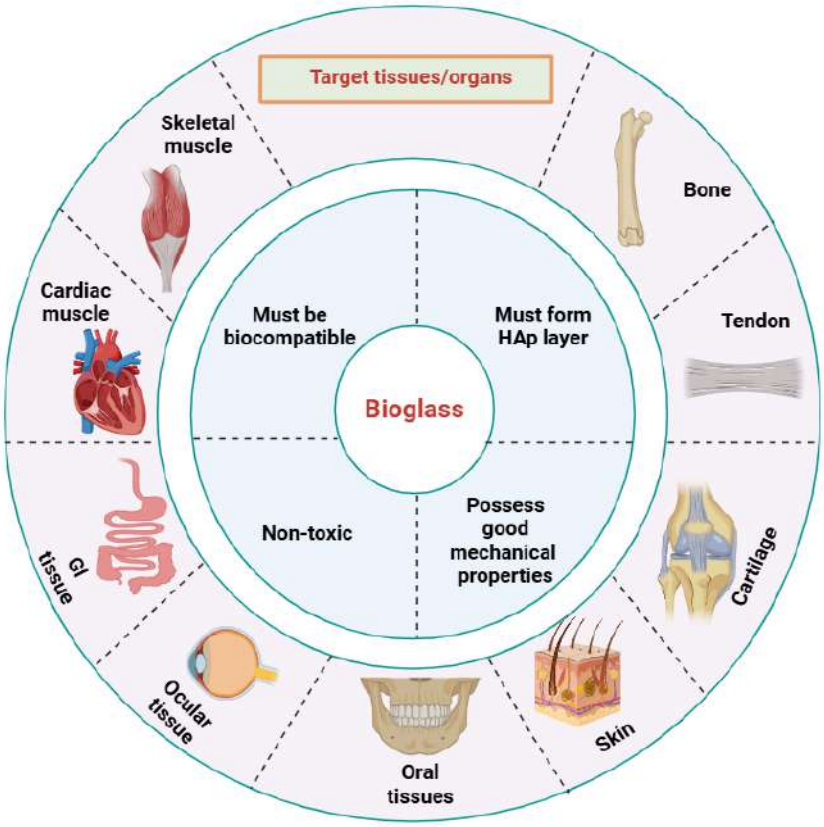

Figure 1.4: Ideal characteristics required for bioglass/bioglass ceramics and their applications

In addition to the composition, bioactive glass must have good interaction with body fluids, ensuring the formation of an apatite-like layer that promotes osteogenic cell proliferation and cellular adhesion, leading to partial bone replacement after long-term implantation. The synthesized glasses should also exhibit compatibility with host tissues without adverse effects. During synthesis, it's crucial to ensure that released elements remain within biologically safe levels, demonstrating compatibility and no cytotoxicity. **Fig. 1.4** illustrates the ideal characteristics required for bioactive glasses as implants and their applications.

While traditional methods for synthesizing bioactive glass depend on conventional chemicals, researchers are increasingly looking for ways to synthesize

these materials in a more sustainable, cost-effective, and eco-friendly ways. One exciting approach is to transform waste from agriculture and food production into bioactive glass. This "trash to treasure" approach not only holds promise for a greener future but also offers a potential solution for managing the vast amounts of agro-food waste generated globally.

1.7 Agro-food waste as resource

Presently, the world produces an average of 23.7 million tonnes of food each day [49]. However, as agricultural production intensifies to support a growing population, managing agro-food waste has become a critical issue. The agricultural and food sectors generate approximately one billion tonnes of waste annually, with around one-third of all food intended for human consumption going unused or wastes [50]. This represents a complex challenge with significant environmental and economic impacts.

Although agricultural waste is biodegradable, the decomposition process can be slow, and farmers often need to clear their fields quickly for the next planting season. The costs involved in collecting, processing, and transporting this waste can be prohibitive, often outweighing potential profits from alternative uses. Consequently, some farmers burn crop residues, a practice that contributes to air pollution and produces ash as a secondary byproduct [51][52]. Land-filling is another common disposal method, but it poses environmental risks such as greenhouse gas emissions and groundwater contamination [53]. The need for sustainable and efficient agro-food waste management is clear. Developing innovative approaches to reduce environmental impact while enhancing resource recovery is essential for planetary health and food security.

The agricultural industry, a major biomass producer, plays a key role in transitioning to a more sustainable energy future. Agricultural residues can be converted into biofuels like bio-oil, bio-char, and biogas, providing cleaner alternatives to fossil fuels and helping reduce greenhouse gas emissions [53]. However, the process of generating bioenergy from agricultural waste often leaves behind ash, a byproduct that requires careful management. While ash

can be harmful due to its small particle size, it also contains valuable minerals like SiO_2, CaO, Na_2O, K_2O, and P_2O_5, making it a potential source for various value-added products [52][54]. The mineral composition of agro-food waste ash varies depending on factors like crop type, soil composition, and fertilizer use, allowing for the synthesis of a diverse range of glasses and ceramic materials. **Table 1.4** indicates the chemical compositions of different agro-food waste ashes, such as rice husk ash (RHA), sugarcane leaves ash (SCLA), sugarcane baggase ash(SCBA), corn husk ash(CHA), eggshell (ES), coconut cell (CC), peanut shell (PS), and wheat straw ash (WSA) residues, etc. [52][55].

Table 1.4: Oxide composition of agro-food waste ashes obtained from EDS

Wastes	SiO_2	CaO	K_2O	Na_2O	MgO	P_2O_5	Fe_2O_3	Al_2O_3	SO_3	Ref.
RHA	97.8	0.6	1.3	–	<1	–	<1	<1	–	[55]
ES	<1	98.6	<1	–	–	–	<1	–	–	[55]
CHA	35.7	5.8	20.2	5.1	9.9	22.5	<1	<1	–	[52]
PS	29.3	21.9	25.7	<1	6.7	7.4	1.3	3.7	3.2	[52]
SCSA	58.6	4.6	5.4	–	1.6	–	8.4	9.0	1.9	[52]
WSA	73.9	5.2	11.5	–	1.8	–	1.5	<1	–	[52]

RHA and ES are good sources of SiO_2 and $CaCO_3$ among agro-food waste ashes. Rice husk, a common global byproduct, generates approximately 18-22 % RHA after processing, providing an economical, readily available, and highly reactive silica source with a substantial surface area [56]. Similarly, eggshells, which make up a considerable portion of global food waste, are rich in calcium carbonate ($CaCO_3$) and serve as an excellent calcium source for various applications [57][58]. RHA, rich in amorphous silica (SiO_2) [59], can be obtained from rice husk through combustion or chemical extraction methods [55][60]. Typically, combustion-derived RHA comprises around 97 % silica, with trace elements making up the balance, and its purity can be further increased to nearly 99 % with acid or alkali treatments. On the other hand, ES, primarily composed of $CaCO_3$, can often be used directly as a raw material without significant pre-treatment [55][61].

The abundance of SiO_2 in RHA and $CaCO_3$ in ES makes them ideal candidates for synthesizing calcium silicate-based materials, including glasses and

bioglasses [62][63]. RHA serves as a cost-effective source of silica for producing various glasses, including microelectronic devices, dielectrics [62][64][65], and importantly, bioactive glass-ceramics [66][67]. RHA-derived glass-ceramics, mimicking the composition of Hench's 45S5 bioglass, have demonstrated promising bioactivity when tested in simulated body fluid [63], highlighting RHA's potential for creating biocompatible materials suitable for bone regeneration and tissue engineering.

ES has also shown promise as a valuable source of calcium for producing hydroxyapatite (HAp), a well-known bioactive material that supports bone growth and integration [68][69]. This reinforces the versatility of agro-food waste as a sustainable source for synthesizing a range of advanced materials with applications in healthcare and beyond.

This chapter has explored the fundamental aspects of bioactive glasses and glass ceramics, including their properties, synthesis, and biological interactions, emphasizing sustainable approaches like using agro-food waste as a resource to develop bioglass or bioceramics. The next chapter provides a comprehensive review of recent advances in sustainably derived bioglasses and glass ceramics, focusing on developments from the past few years.

CHAPTER 2

Literature Review

Overview

This chapter presents a comprehensive literature review on sustainable bioactive glasses, focusing on utilizing agro-food wastes as a source of valuable precursors. The review explores the potential of various agro-food wastes, including rice husk ash (RHA) and eggshell powder (ESP), as sustainable alternatives to conventional chemicals for synthesizing the glasses. It examines different processing techniques for extracting valuable materials from these wastes and discusses various synthesis methods employed for producing bioactive glasses and glass ceramics. The review also analyzes the structure-property relationships in these materials, emphasizing the impact of composition and processing parameters on bioactivity, biocompatibility, and mechanical properties of end products. Furthermore, it investigates the in-vitro and in-vivo performance of agro-food waste-derived bioactive glasses in various biomedical applications. Finally, the key research gaps are identified, and the motivation for the present study is given. Based on these, the objectives for the present work are given at the end of this chapter.

2.1 Value added materials from agro-food waste ashes

The increasing generation of agricultural, food waste residues and their ash by-products poses significant health and environmental challenges. However, these wastes also offer a valuable source of materials, as discussed in Chapter 1. Agro-food wastes and their ashes contain substantial amounts of elements like carbon, silicon, calcium, magnesium, phosphorus, and potassium (**Table 1.4**), providing a sustainable alternative to conventional chemicals used in glass synthesis. Silica (SiO_2) is a major component in many agro-food waste ashes, such as rice husk ash (RHA), sugarcane bagasse ash (SCBA), corn husk ash (CHA), and wheat straw ash (WSA), making them attractive for silica-based applications [56][63][70][71]. However, the purity and form of silica depend heavily on processing parameters. While RHA can yield 80-97% pure silica, it also contains other alkali and alkaline earth metal ions (**Table 1.4**), offering flexibility in glass composition but posing challenges for precise control over elements content. These challenges can be addressed through mineral extraction techniques such as calcination at controlled temperatures or acid pre-treatments to these wastes.

The processing parameters, particularly temperature and duration, are crucial in determining the reactivity and crystalline structure of the extracted silica. Controlled rice husk (RH) combustion below 700 °C typically yields amorphous silica ash. Higher temperatures ($>$ 800 °C) generally result in crystalline ash, although amorphous silica can still be obtained with a shorter duration at these heat treatment temperatures [72]. Fernandes *et al.* [73] reported the transition to crystalline silica above 850 °C. In a subsequent study, the two different extraction methods were used, and crystalline SiO_2 (cristobalite and tridymite phases) with approximately 99% purity was obtained after heat treatment above 1000 °C [74]. Some studies have achieved amorphous silica at temperatures up to 900 °C with heat treatment times less than 1 hour [75]. Conversely, prolonged exposure (e.g., 15 hours) can induce crystallization even at lower temperatures like 300 °C for heat treatment of RH [75].

Beyond temperature and time, pre-treatments like acid leaching can signif-

icantly influence the extracted silica's quantity and purity. For example, acid leaching of RHA sintered at 600 °C under an inert atmosphere can yield silica >90% with few metallic impurities. Yalcin and Sevinc [76] and Real *et al.* [77] obtained silica from RHA with a purity index of 99.87% ± 0.01 by combining acid pre-treatment with burning RH at 700 °C for 6 h in air. Deshmukh *et al.* [78] extracted amorphous SiO_2 with 97.73% purity using acid leaching followed by burning at three different temperatures. Dhaneshwara *et al.* [79] achieved similarly high SiO_2 purity (≈ 99%) by burning rice husk at 700 °C in an electric furnace followed by acid treatment. Beyond RHA as a rich silica source, food waste like eggshell powder (ESP) offers a valuable source of calcium. High-temperature treatment of ESP yields highly pure calcium oxide (≈ 99%) along with some trace elements [58][80]. Incorporating ESP into glass compositions introduces calcium oxide, which acts as a network modifier and can reduce the melting temperature of the silica glass melt, offering another avenue for tailoring material properties [64].

2.2 Biogenic silica derived bioglass/bioglass-ceramics

As discussed in the preceding section, agro-food waste ashes, rich in various minerals, have found applications in diverse engineering and medical fields. For glasses intended as biomaterials, in-vitro bioactivity testing, particularly the formation of a bone-like apatite layer on the material's surface when immersed in SBF, serves as a crucial evaluation method. This formation of the apatite layer, a key indicator of bioactivity, is influenced by several factors, including glass composition, the synthesis method, immersion time in SBF, and specific immersion conditions. Since the discovery of bioglass in 1969, researchers have extensively explored variations in composition and processing parameters to optimize bioactivity, according to the needs of different applications [2][6][81][82].

Beyond conventional chemical precursors, researchers have investigated the use of extracted silica from rice husk ash (RHA) as an alternative sustainable resource [63][83][84]. Various processing techniques, including sol-gel and melt-quench methods, have been employed to synthesize bioactive glasses

using silica derived from RH and RHA [85][86][87]. For example, Nayak *et al.* [85] extracted amorphous silica from RH as sodium silicate and utilized it as a precursor for sol-gel synthesis of bioceramics. Similarly, Yucel *et al.* [88] synthesized 46S6 bioactive glass ($46SiO_2$-$24Na_2O$-$24CaO$-$6P_2O_5$) in wt% via melt-quenching at 1400 °C using biogenic silica from RHA. The glasses were immersed in SBF for 7 days at a concentration of 20 mg/ml. The result indicates the partial HAp formation, highlighting the influence of factors like surface area/volume ratio on apatite layer formation kinetics.

Further research by Yucel *et al.*[89] explored the effects of substitution of SrO for CaO in a $45SiO_2$-$24.5Na_2O$-$14CaO$-$6P_2O_5$-10.5SrO (wt%) bioglass composition synthesized via melt-quenching using RHA-derived silica. It was found that Sr^{2+}, due to its lower field strength compared to Ca^{2+}, creates a more loosely cross-linked glass network. This structural change resulted in increased bioactivity and a thicker apatite layer with an increase in the immersion time in SBF (7 to 21 days). Furthermore, these bioglasses exhibited continuous, though slow, weight loss for up to 7 days in Tris buffer solution, attributed to the release of Ca^{2+}, Na^{+}, Si^{4+}, and P^{5+} ions. This degradation behavior, along with a favorable pH range (7.4-8.2) for osteoblasts, offers additional evidence of the bioactivity of the materials [90]. Similarly, Karakuzu-Ikizler *et al.* [91] investigated substituting magnesium and alumina (up to 1 wt%) for CaO in 45S5 bioglass synthesized with RHA-derived silica. Their findings indicated enhanced hardness without compromising bioactivity, surpassing the apatite layer formation observed in bioglasses made with commercial or conventional silica. The addition of magnesium oxide and alumina also improved the biodegradability of the commercial silica glasses. The impact of heat treatment on mechanical properties was explored by Leenakul *et al.* [63]. Enhanced mechanical properties were observed in 45S5 bioglass made with biogenic silica after heat treatment at different temperatures. The promising bioactive properties were retained. These studies highlight the potential for tailoring bioglass properties through compositional adjustments and processing techniques when utilizing RHA as a sustainable silica source. Subsequently, the heat treatment temperature and glass stability significantly influence the bioactivity and

mechanical properties of bioactive glasses and glass ceramics. Glass ceramics, produced through controlled crystallization (vitrification, nucleation, and crystal growth), can exhibit enhanced density, chemical durability, and mechanical strength. Potentially, compressive strength can be increased due to heat treatment effects such as particle rearrangement, mass diffusion to pores, and grain growth. However, fully crystallized glass ceramics can negatively impact bioactivity by decreasing dissolution rates and hindering apatite formation [92]. A balance between enhanced mechanical properties and bioactivity can be achieved by inducing partial, controlled crystallization, resulting in semi-crystalline phases. Successful controlled crystallization depends on heat treatment parameters, including heating rate, nucleation, crystallization temperatures, and heat treatment duration. Precise control over these parameters is crucial for achieving homogeneous microcrystalline glass ceramics with uniform microstructures and optimized mechanical properties [93].

For instance, Peitl *et al.* [94] studied the crystallization and SBF interaction of Na_2O-CaO-SiO_2 glasses and glass-ceramics with varying P_2O_5 content in glass composition. It was observed that these materials formed a carbonated hydroxyapatite (c-HAp) layer even after controlled crystallization at 550–700 ^oC. Fourier-transform infrared spectroscopy (FTIR) and inductively coupled plasma-optical emission spectroscopy (ICP) analyses revealed significantly faster c-HAp formation (8–35 h) after SBF immersion compared to conventional bioactive ceramics, which typically require at least 7 days. This enhanced bioactivity in the above composition is attributed to two key mechanisms: the formation of a non-phosphate bioactive crystal phase ($Na_2Ca_3Si_3O_9$) and the rapid release of phosphorus ions from the crystal structure's solid solution. Remarkably, even phosphorus-free compositions formed a c-HAp layer by absorbing phosphorus from the SBF solution. Although crystallization increased the onset time for c-HAp formation, it did not hinder the overall bioactivity of the material.

Few studies have reported similar findings, indicating that increasing crystallinity in bioglass/bioceramics slows down the bioactivity [92][95]. On the other hand, some research even demonstrates enhanced bioactivity in partially

crystallized glass-ceramics, where two or more crystalline phases are present [96]. For instance, Loh *et al.* [97] reported that heat-treating CaF_2-CaO-Na_2O-B_2O_3-SiO_2 glasses at 700 °C to form glass-ceramics increased densification, microhardness, and fracture toughness while retaining bioactivity comparable to the pristine glass. Their in-vitro bioactivity studies, using phosphate-buffered solution (PBS) immersion, confirmed apatite layer formation, indicating physicochemical reactions between PBS and glass that promote bioactivity. Some studies have even demonstrated that 45S5 glass-ceramic containing combeite crystals with high crystallinity (up to 100%) can retain their bioactivity [96][98]. Similarly, Siqueira *et al.* [99] reported that the formation of wollastonite ($CaSiO_3$) and α-tricalcium phosphate ($Ca_3(PO_4)_2$) crystalline phases in a glass matrix increased bioactivity.

In addition to using conventional chemical precursors for the synthesis of bioglass/bioglass ceramics, numerous studies have investigated RHA-derived bioglass and bioglass ceramics. These studies often report comparable properties to conventionally synthesized materials. For instance, Nayak *et al.* [83][85] utilized RHA as a silica source for sol-gel derived glasses ($50SiO_2$-$25Na_2O$-25CaO mol%). It was found that heat treatment at 1000 °C yielded combeite and devitrite crystals with good mechanical strength. However, heat treatment at 1050 °C resulted in decreased strength. This was due to the formation of cracks in glass ceramics, attributed to thermal expansion mismatch between glass matrix and ceramics. The same group also fabricated porous bioactive ceramics from RHA-derived silica gel, achieving a mechanical strength of 27.5 $\pm$ 0.2 MPa with $\sim$ 25% porosity. The apatite formation was confirmed during in-vitro test. Leenakul *et al.* [63] observed a transition from amorphous to crystalline phases in melt-quenched 45S5 bioglass derived from RHA upon heat treatment at 650-1050 °C. Optimal mechanical properties were achieved at 1050 °C while maintaining bioactivity. Furthermore, mesoporous bioglass (MBG) was synthesized from RHA via the sol-gel method. The results showed promise for drug delivery and bone regeneration, exhibiting no cytotoxicity and effectively delivering an anticancer drug [66][100].

In addition to RHA, eggshell powder (ESP) is another valuable agro-food

waste resource, rich in calcium oxide, for bioglass and bioglass-ceramic synthesis. The use of eggshells and their membranes as a CaO source has gained significant attraction [101]. An in-vivo study showed enhanced angiogenesis and antibacterial activity in copper-doped bioglasses nanocoated with the eggshell membrane (ESM)[32]. Punj *et al.* [71][102] synthesized bioactive calcium silicate glasses from corn husk ash (CHA), sugarcane leaf ash (SCLA), and ESP, reporting enhanced bioactivity and osteointegration compared to mineral-derived glasses, with microhardness increasing with eggshell replacement (575–638 H_v). Diopside ($CaMgSi_2O_6$) from these agro-waste sources was also synthesized, demonstrating apatite formation and non-toxicity in-vitro [61]. Pala-kurthy *et al.* [103] synthesized bioactive SiO_2–CaO–Na_2O bioglass from eggshells and RHA, confirming bioactivity, HAp formation, and cytocompatibility.

Beyond these applications, ESP has also been utilized to synthesize various bioceramics [104]. Choudhary *et al.* [105] synthesized akermanite ($Ca_2MgSi_2O_7$), diopside ($CaMgSi_2O_6$), and nanocrystalline larnite (Ca_2SiO_4) using ESP via sol-gel and mechanical milling methods. HAp formation on akermanite was observed by them after 7 days in SBF. Cell proliferation, osteogenesis, and angiogenesis were promoted, while osteoporotic bone regeneration was suppressed in-vitro. The synthesized diopside exhibited a bonding strength of approximately 350 ± 7 MPa and a fracture toughness of 4 ± 0.3 MPa [106][107][108][109]. Other studies have explored wollastonite ($CaSiO_3$), diopside, forsterite, and pseudo-wollastonite ceramics synthesized from RHA and ESP by heat treatment at various temperatures (870–1300 °C). Wollastonite glass-ceramics showed a greater propensity for HAp formation than pseudo-wollastonite due to enhanced degradability in SBF [110][111]. Loh *et al.* [112] reported that these materials, sintered at 700 °C, achieved excellent mechanical properties (5.34 ± 0.21 GPa microhardness, 2.99 ± 0.24 $MPa{\cdot}m^{1/2}$ fracture toughness), comparable to human enamel while retaining bioactivity and biodegradability in PBS, although with a slower apatite formation rate.

These studies highlight the complex relationship between thermal behavior, heat treatment temperature, and bioactivity. Higher heat treatment temper-

atures often increase crystallinity, potentially reducing bioactivity due to decreased dissolution and permeability in SBF and other in-vitro testing fluids. For bioglass and bioglass-ceramics derived from agro-food waste, biodegradability (silica network dissolution and apatite formation) is also influenced by impurity oxides inherited from the rice husk ash [113]. RHA-derived bioactive glass-ceramics (R-SBgC) combined with polycaprolactone (PCL) using the thermally induced phase separation (TIPS) method have shown promising results as bioactive composite scaffolds. These scaffolds have enhanced density and compressive modulus, suitable for non-load-bearing bone substitutes [67][114]. Other bioactive materials like calcium phosphate and silicate-calcium ceramics are also being synthesized from agro-food waste, showcasing the versatility of these sustainable resources [115][116][117]. These studies demonstrate the potential of agro-food waste-derived bioactive glasses and glass-ceramics for various biomedical applications, particularly in bone regeneration, due to their promising bioactivity and biocompatibility. While bioactive glasses stimulate bone growth by promoting the formation of hydroxyapatite (HAp), the use of naturally derived HAp itself as a biomaterial is also a promising area of research, as discussed in the following section.

2.3 Hydroxyapatite and natural sources

As discussed in the previous section, HAp plays a crucial role in the bioactivity of bioglasses and glass-ceramics. This naturally occurring calcium phosphate mineral exhibits excellent bioactivity and is a major component of both teeth and bone, readily bonding with natural bone tissue due to its similar chemical and structural composition [118]. However, the mineral composition of human bone differs slightly from stoichiometric HAp due to the presence of impurities like carbonate, chloride, fluoride, magnesium, and sodium [119]. Natural bone apatite contains approximately 3–8 wt% carbonate [120].

While commercially available calcium phosphate bioceramics such as tricalcium phosphate (TCP), biphasic calcium phosphate (BCP), and HAp are often expensive due to the required high-purity reagents, naturally derived HAp presents a cost-effective alternative [121]. Natural sources, including fish bone,

bovine bone [122][123], coral [124], and oyster shells [125], can be processed to obtain HAp. Naturally derived HAp often exhibits enhanced bioactivity due to its inherent porosity [118][126]. In contrast, commercially synthesized HAp, often produced via hydrothermal synthesis or chemical precipitation methods, may lack essential trace elements like magnesium, sodium, potassium, silicon, strontium, and iron [126].

Coralline HAp, derived from the hydrothermal conversion of coral skeletons, has been used in biomedical applications [119][124][127]. However, the endangerment and slow growth of some coral species necessitate exploring alternative renewable sources. Avian eggshells, with a mineral composition similar to coral and readily available, have emerged as a promising candidate, particularly for maxillofacial and craniofacial surgery [116][128]. Similarly, Chicken eggshells, comprising about 11% of an egg's weight, consist primarily of calcium carbonate (94%), with smaller amounts of magnesium carbonate (1%), calcium phosphate (1%), and organic matter (4%). Importantly, it also contain trace elements like Na, Mg, and Sr, found in human bone, further supporting their potential as a biomaterial source [129]. Furthermore, chicken eggshells are being used to synthesize various calcium salts crucial for bone regeneration, including β-tricalcium phosphate (β-TCP), BCP, CaO nanoparticles, and HAp. These calcium salts, commonly used in biomaterials, enhance the osteoconductivity of the resulting materials by mimicking the inorganic components of native bone [109].

Chicken eggshells, a readily available biowaste resource, are rich in calcium carbonate (95-98% $CaCO_3$) and also contain trace elements such as Mg, Sr, Si, Na, and F, making them an attractive source for HAp synthesis. While these trace elements are present in relatively small amounts, it can influence the properties of the resulting HAp. Studies have shown that the presence of these ions, even at trace levels, can affect the lattice structure, vibrational frequencies, and thermal stability of commercially synthesized HAp, potentially impacting its bioactivity and biocompatibility [130].

Several studies have investigated the use of eggshells for HAp synthesis,

employing various processing techniques. For example, Ahmed *et al.* [130] demonstrated the synthesis of HAp from calcined eggshells. Their method yielded HAp with a combination of amorphous and crystalline phases and a Ca/P molar ratio of 1.69. The researchers observed that further heat treatment could enhance the crystallinity of the final product. Siddharthan *et al.* [116] explored a microwave processing method to synthesize nanocrystalline apatite from chicken eggshells, achieving varying Ca/P ratios (1.5, 1.60, and 1.67). These eggshell-derived HAp materials exhibited improved morphology, stoichiometry, thermal stability at higher temperatures, and enhanced osteoblast cell adhesion compared to some commercially synthesized HAp materials [131]. Importantly, it has been also observed that the presence of trace elements did not negatively affect the bioactivity and biocompatibility of the eggshell-derived HAp [116]. Similar results were obtained by Dumitrescu *et al.* [132], who synthesized hydroxyapatite powder from eggshells using a microwave-assisted hydrothermal technique. Their study compared the eggshell-derived HAp with commercially available bone-derived HAp materials, namely partially deproteinized porcine bone (Gen-Os®) and deproteinized cortical bovine bone (Bio-Oss®). The results indicated that the eggshell-derived HAp exhibited significantly higher mesoporosity, suggesting improved biomolecule adhesion and osteoconductivity, which are essential properties for bone regeneration.

The specific extraction process employed for obtaining HAp from eggshells plays a crucial role in determining the final material's properties, including the Ca/P ratio, crystallinity, phase assemblage, and particle size [133]. These properties, in turn, influence the bioactivity, biocompatibility, and overall performance of the HAp in biomedical applications. Ahmed *et al.* [130], in their earlier work, reported that calcination of eggshells at 900 °C for 30 minutes resulted in the formation of a single crystalline HAp phase. This calcined HAp exhibited spherical, hexagonal, and cylindrical shapes, as confirmed by scanning electron microscopy (SEM) analysis. The crystallite size was found to be in the range of 30-60 nm, and the Ca/P molar ratio was 1.66. This highly crystalline single-phase HAp contrasted with the mixed amorphous and crystalline phases observed in uncalcined eggshells. In addition, Patel *et al.* [134] re-

ported the synthesis of highly crystalline hydroxyapatite from eggshells using a combination of sonication and calcination. Their method resulted in improved cell viability, suggesting a greater biocompatibility for the synthesized HAp. Furthermore, Sultana *et al.* [135] developed a novel UV-mediated solid state method for the synthesizing of hydroxyapatite from eggshells without the need for thermal treatment. This innovative approach involved ball milling the eggshells, followed by UV irradiation at room temperature. It was indicated by their results that the HAp produced through this UV-mediated method exhibited admissible in-vitro bioactivity and no significant cytotoxicity. Microwave irradiation offers a rapid and efficient method for HAp synthesis. Krishna *et al.* [131] synthesized nanocrystalline HAp (N-HAp) with this method, achieving platelet-like morphology, high-temperature stability, and enhanced osteoblast cell adhesion. Ultrasonication followed by calcination at 600 ^{o}C has also been used to produce N-HAp with comparable mechanical properties to commercial HAp, exhibiting enhanced *in-vitro* bioactivity and biocompatibility. Microwave processing advantages include shorter processing times, high reaction rates, narrow size distribution, and high purity, making it suitable for applications such as implant coatings [136]. Furthermore, heat treatment at higher temperatures (1000-1150 ^{o}C) can refine particle size and improve mechanical properties such as compressive strength, hardness, and fracture toughness.

Numerous other methods, including wet chemical, solid-state reaction, hydrolysis, and mechanochemical techniques, have also been employed for HAp synthesis [137][138][139][140] Ramesh *et al.* [141] used a solid-state sintering method with calcined eggshell powder (ESP) and dicalcium hydrogen phosphate dihydrate (DCPD), achieving high densities ($> 98\%$) at heat treatment temperatures of 1300–1350 ^{o}C. Optimal properties, including enhanced fracture toughness and hardness, and a fine grain size, were obtained after heat-treatment at 1250 ^{o}C. Ho *et al.* [142] used a similar method, initially obtaining β-TCP with minor HAp, converting to single-phase HAp after further heat treatment. These HAp/TCP bioceramics find applications in bone grafts, drug delivery, and protein purification.

2.4 Processing parameters' effects on bioactivity of bioglasses/ bioglass-ceramics

The properties of bioactive glasses and glass ceramics are intricately linked to their composition, structure, and processing methods. In the case of bioglass and glass ceramics derived from agro-food waste, these parameters become even more critical, as the presence of trace elements and compositional variations in the waste-derived precursors can influence the structural and functional properties of the materials. The thermal processing route, particularly the melting temperature, quenching rate, and heat treatment schedule, strongly affects phase stability, network polymerization, and ion release behavior. Synthesized primarily through melt-quench or sol-gel techniques, these materials are extensively used in biomedical applications, such as implant coatings, bone grafts, and scaffolds, where mechanical and thermal properties are crucial. Understanding the structural transformations and crystalline phases resulting from heat treatment is essential for optimizing their performance [143].

The glass transition temperature (T_g) is a fundamental parameter influencing the thermal behavior of bioactive glasses. As O'Donnell [144] demonstrated, precise estimation of T_g enables the prediction of other temperature-dependent properties critical for processing, such as annealing temperature, and heat treatment temperature. Moreover, T_g is directly linked to the network connectivity of the glass, which governs both its bioactivity and mechanical properties. In applications like implant coatings, maintaining the stability of glass properties is critical, as undesirable variations, such as changes in the TEC, can induce stress and strain within the material. Localized strain may affect the bioactivity and as well as other properties of the glass [145]. Additionally, a mismatch in the TEC between the substrate and coating material can lead to delamination or failure of the composite system [146]. Therefore, understanding the thermal behavior and temperature-dependent properties of bioactive glasses is imperative for selecting optimal compositions and ensuring reliable performance. Several theories have been proposed to elucidate the roles of various ions in bioactive glasses, focusing on aspects such as structure, ionic potential,

and network connectivity [147][148][149]. However, these effects may vary when bioactive glasses are synthesized using agro -food waste-derived sources, as the trace elements and variable oxide contents in precursors like RHA and ESP can subtly alter network connectivity and modifier behavior [71]. Thus, understanding the structural role of modifier oxides such as MgO and K_2O becomes crucial for evaluating how compositional and structural variations influence bioactivity. Furthermore, the potential interaction between MgO and P_2O_5 can further affect bioactivity of these materials. While P_2O_5 is a well-established glass former, MgO exhibits a dual nature, acting as both a network former and a network modifier depending on its concentration and the overall glass composition [150].

Magnesium, a vital mineral and the fourth most abundant element/cation in the human body after calcium, sodium, and potassium, plays a crucial role in numerous physiological processes [93]. It is a key component of bone, dentin, enamel, muscle, and soft tissues, acting as a cofactor in over 300 enzymatic reactions. Magnesium's involvement in physiological functions includes bone development, protein synthesis, muscle contraction and relaxation, nucleic acid synthesis, Adenosine triphosphate (ATP) metabolism, and vitamin-D stimulation. Maintaining appropriate magnesium levels in extracellular fluid (0.7-1.05 mMol/L) is essential for these processes. Its higher concentration in the stratum corneum, the outermost layer of the epidermis, suggests a role in skin barrier function, epidermal differentiation, and proliferation [6][151][152]. Additionally, magnesium regulates active calcium transport, activates phagocytosis, and is involved in calcification processes within calcified tissues [6][43]. However, magnesium's role in bioactive glasses is complex and debatable. Some studies suggest that high magnesium concentrations inhibit the formation of the apatite layer [43][153], while others report no significant effect on the formation of the apatite layer [150][154]. This discrepancy highlights the need for further research to fully understand the influence of magnesium on bioactivity. Balamurugam *et al.* [155] synthesized a $55SiO_2$-26CaO-13MgO-$6P_2O_5$ (mol%) bioactive glass via the sol-gel method and observed rapid increases in pH and the release of Ca^{2+} and Mg^{2+} ions in SBF, indicating high reactivity

and bioactivity. The formation of a silica-rich layer that subsequently crystallized to form hydroxyapatite was reported, further confirming the material's bioactivity. While CaO and MgO share similar properties, CaO consistently acts as a glass modifier. It occupies interstitial spaces within the glass network, increasing NBOs and reducing network connectivity in the glass. This structural modification by CaO contributes significantly to the properties and bioactivity of the glass. The presence of magnesium in the glass composition is also reported to promote cell adhesion and osteoblast proliferation [43].

Al-Noaman *et al.* [156] investigated the effects of partially substituting MgO for CaO in bioactive glass coatings. The resulting changes in thermal properties, structure, and bioactivity in SBF were evaluated for the glasses. Their findings indicated that magnesium suppressed crystallization and decreased the TEC, T_g, and T_s. Importantly, it was concluded that the glasses' ability to form apatite was not inhibited by magnesium, but rather the onset of apatite deposition was delayed. This suggests a nuanced role for magnesium in the bioactivity mechanism. Wetzel *et al.* [157][158] further investigated the effects of partially replacing CaO with MgO, confirming that magnesium addition up to a certain threshold did not hinder apatite formation. Additionally, a widening of the sintering window for bioactive glasses with increasing magnesium substitution was observed, offering potential advantages for processing and controlling material properties. Fiume *et al.* investigated the biological response of novel silicate bioactive glasses containing MgO. In one study [159], a 47.5SiO_2-10Na_2O-10K_2O-10MgO-20CaO-2.5P_2O_5 (mol%) glass demonstrated excellent pro-osteogenic properties and complete resorption within 3 months in-vivo, with new tissue formation. An earlier study by the same group [160] on a similar SiO_2-Na_2O-K_2O-MgO-CaO-P_2O_5 glass also showed excellent cytocompatibility and osteogenic effects in-vitro and in-vivo. Jha *et al.* [161] found that substituting MgO for CaO in a SiO_2-K_2O-CaO-MgO glass increased chemical durability, slowing ion release during in-vitro bioactivity tests, while increasing hardness (464-502 H_V), comparable to bone. These studies highlight the potential benefits of incorporating MgO in bioactive glasses for bone regeneration. Expanding on this, Ikizler *et al.* [91] studied the effect of 1 wt% MgO

addition to 45S5 bioglass synthesized with biogenic silica via melt-quenching. Enhanced hardness in both biogenic and commercial silica-based bioglasses was observed. Moreover, magnesium incorporation specifically improved the bioactivity and biodegradability of the commercial silica-based glasses. These results highlight the significant influence of both silica source and magnesium addition on bioglass properties.

Further studies have demonstrated that the addition of alkali oxides to bioactive glass compositions can offer several advantages, including lower melting temperatures, leading to more economical production of glasses. Up to a certain concentration, alkali oxides also enhance glass solubility in aqueous media, promoting increased interaction between the host tissue and the biomaterial, a key factor for bioactivity. Moreover, the presence of alkali oxides can improve the thermal stability of bioglasses by suppressing crystallization, which in turn facilitates better sintering and control over the final material's microstructure [46][162]. Cannillo *et al.* [163] investigated a novel potassium-based bioactive glass (46.1SiO_2-2.6P_2O_5-26.9CaO-24.4K_2O mol%), inspired by 45S5 Bioglass ®, where K_2O substituted Na_2O. While the thermo-mechanical properties and in-vitro response were comparable to 45S5, the potassium-containing glass exhibited higher stability during enameling, avoiding crystallization, unlike 45S5. This suggests its greater suitability for producing glass coatings. Crovace *et al.* [164] explored the impact of Na_2O substitution with K_2O in a similar silicate glass system. A decrease in crystallization kinetics and viscosity was observed, with the $Na_2O/K_2O \approx 1$ composition exhibiting the fastest densification, confirming the mixed alkali effect (MAE) on sintering kinetics. While HCA formation in SBF was unaffected, the osteogenic potential of pre-osteoblastic cells was enhanced.

Sinitsyna *et al.* [165] studied the broad range of K_2O substitution for Na_2O (0-100%) in S53P4 bioactive glass, also observing an MAE, particularly influencing thermal properties, most notably around 20% K_2O. Higher K_2O levels expanded the glass network, decreasing density and widening the thermal processing window. Ion release kinetics in TRIS and SBF showed varied trends depending on the substitution level, with single-alkali glasses exhibiting supe-

rior bioactivity compared to mixed-alkali compositions. Moderate K_2O substitutions (<40%) reduced bioactivity and thermal processing flexibility, while higher levels (>66%) enhanced processability but moderately decreased bioactivity. Fully substituted K_2O glass, however, exhibited low crystallization and promising bioactivity. Similarly, Zia *et al.* [166] investigated the impact of K_2O on the microstructure of a Na_2O-CaO-P_2O_5-SiO_2 ceramic system synthesized via heat treatment at 900 °C. Increased thermal stability and a decreased crystallization tendency with increasing K_2O content were observed, which can be beneficial for promoting in-vitro bioactivity. The major crystalline phases identified were sodium calcium silicate ($Na_2Ca_3Si_6O_{16}$), combeite ($Na_2Ca_2Si_3O_9$), and wollastonite ($CaSiO_3$). These findings highlight the complex influence of K_2O substitution on properties and bioactivity, enabling tailored glass design.

2.5 Biocompatibility of agro-waste-derived bioglasses/ bioglass-ceramics

Biocompatibility is an essential requirement for biomaterials, especially those intended for implantation. in-vitro cytotoxicity testing offers a crucial initial assessment of bioglasses and glass ceramics, providing valuable safety data and informing subsequent in-vivo studies [167]. Chen *et al.* [66] synthesized Mesoporous Bioglass from low-cost agricultural waste rice husk (rMBG) using a sol-gel process. It was shown that rMBG has typical characteristics of the well-ordered hexagonal mesostructure of MBG and can be grafted with folic acid (FA) and then loaded with anticancer drugs for targeting cancer cells. It was concluded that low-cost rMBG offers a potentially practical medical application that can replace highly valuable MBG as well as reduce environmental pollution caused by agricultural waste. Yucel *et al.* [88] studied the cytotoxicity of rice husk derived 46S6 bioactive glasses with a concentration of 20 mg/ml on sarcoma osteogenic (SAOS-2) osteoblast-like cells cultured in Dulbecco's Modified Eagle Medium-F12 (DMEM-F12) media via MTT assay. 46S6 glass has shown no toxic effect during the test. Furthermore, the substitution of strontium in 45S5 bioactive glasses (using RHA) was also studied to determine their cytotoxicity via MTT assay. Strontium has been considered a promising

incorporation agent to enhance the replication of preosteoblast cells and reduce osteoclast activity. The results have shown good metabolic activity and cell viability, due to the controlled degradation rate of strontium and silica ions in DMEM cell culture media determined by inductively coupled plasma-optical emission spectroscopy (ICP-OES). It has also been found that pH change also directly affects the growth of cells, metabolic activity, and membrane potential due to their acidic and basic properties. The fast increment in pH because of H^+ cation occurs due to more ion dissolution of the glass [89]. Palakurthy *et al.* [103] used the human osteoarcoma MG-63 cell lines to test the cytocompatibility of RHA and ESP based bioglasses (SiO_2-CaO-Na_2O) with different concentrations (1000-50 μg/mL) and compared to blank control via MTT assay. The cell viability has been observed at >70% even at a higher concentration i.e., 1000 μg/mL. These bioglasses have demonstrated no toxicity effect that can be used in biomedical applications.
Punj *et al.* [61] studied the effect of diopside synthesized using CHA, SCLA, and ESP on MG-63 cell lines. Furthermore, the cytotoxicity of agro-food waste-derived glasses on similar MG-63 cell lines was studied, and the non-toxic effect of the glasses was reported even at a higher 10 mg/ml concentration [168]. The biocompatibility of biogenic silica nanoparticles (bSNPs) derived from RHA and sugarcane bagasse ash (SCBA) was also assessed by Athinarayanan *et al.* [169] using MTT assay on human lung fibroblast cells (hLFCs) at different concentrations of bSNPs (0, 25, 50, 100, 200, and 400 μg/mL). The cell viability >85% has been found for bSNPs even at a higher concentration of 400 μg/mL, indicating bSNPs are biocompatible amd may be applicable for biomedical applications.

These findings consistently support the biocompatibility of agro-food waste-derived bioactive glasses, even with compositional modifications. Kargozar *et al.* [170] synthesized magnesium (Mg)-contained bioglass (SiO_2–P_2O_5–CaO–$_2$O –MgO–K_2O (mol.%)) to use in bone reconstruction. Bio-glass were then manufactured three-dimensional (3D) scaffolds by using the sponge replica approach. The in-vitro bioactivity and the release of osteo-stimulatory Mg^{2+} ions from the prepared samples was investigated over 7 days of immersion in SBF.

in-vitro cellular analyses revealed the compatibility of the Mg-doped BGs with human osteosarcoma cells (MG-63 cell line). Futher, Shoaib *et al.* [171] synthesized the mesoporous bioactive glass (MBG) with composition (SiO_2-CaO-Na_2O-K_2O-P_2O_5 mol %) by sol-gel method. Polyethylene glycol (PEG 6000) was used as a soft template. The animal study, protein adsorption ability, and cytotoxicity investigations show no tissue damage, good biomedical properties, and no cell cycle encumbrance (even at a concentration of 80 μg/mL). Similar research group studied the effect of Mitomycin C (Mc) loaded mesoporous bioactive glass nanoparticles (Mg-MBG NPs) on MG-63 cancer cells and reported that Mg-MBG alone has no anti-proliferative effect but the Mc-Mg-MBG demonstrated an IC50 value of 20.8 μg/mL and significant inhibitory effects on cancer cells.

The following table summarizes key studies on bioactive glasses and glass-ceramics, highlighting the use of sustainable resources like RHA and ESP as precursors. The table also includes studies investigating the effects of MgO and K_2O substitution on the properties of bioactive glasses.

Table 2.1: Summary of bioactive glasses synthesized from various sources

Composition	**Resources**	**Remarks / Key Findings**	**Reference**
$50SiO_2$–$25Na_2O$–25CaO (mol%)	Hybrid	• RHA-derived bioactive glass-ceramic (R-SBgC) synthesized via sol-gel. • HAp formation confirmed within 14 days in SBF. • Non-toxic to human bone marrow stromal cells (hBMSCs). • Promising for tissue engineering applications.	[67]
Calcium-phosphate layer	Biowaste	• HAp synthesized from ESP via a reaction between CaO and TCP • Ca/P ratio of synthesized HAp close to that of natural bone (1.67). • Exhibited high biocompatibility and no significant cytotoxicity even at higher concentrations. • Indicating its suitability for tissue engineering applications, particularly bone repair.	[172]

Continued on next page

Table 2.1 – *Continued from previous page*

Composition	**Resources**	**Remarks / Key Findings**	**Reference**
SiO_2–P_2O_5–CaO–MgO–MoO_3 (mol%)	Hybrid	• Silica extracted from rice husk. • MoO_3 addition modified the glass network and improved thermal properties. • Amorphous HAp layer formed on glass surface after immersion in SBF • Suggests potential applications in scaffolds and implant materials.	[173]
60CHA-(40-x)SCLA-xESP (x = 10, 20, 30 wt%)	Agro-food waste	• Calcium silicate glasses synthesized using CHA, SCLA, and ESP. • Formed amorphous c-HAp in SBF with Ca/P ratio in the range of 1.78–4.1. • Higher ESP content increased Mg^{2+} release inhibiting the formation of crystalline HAp. • Inherent porosity of bio-waste derived glasses contributes to enhanced bioactivity.	[71]
50SiO_2–25CaO–25Na_2O (mol%)	Hybrid	• Synthesized bioglass via using ESP and RHA as calcium and silica sources. • Formation of HAP confirmed by XRD, FTIR, and SEM–EDS analysis after soaking in SBF. • Exhibited controlled degradation rate in Tris–HCl buffer solution • Cytocompatibility with MG-63 cells, suggesting potential for biomedical applications.	[103]
Diopside ($CaMgSi_2O_6$) from CHA, SCLA, ESP	Agro-food waste	• Synthesized diopside using CHA, SCLA, and ESP. • Confirmed formation of diopside and cristobalite phases. • Formed poorly crystalline HAp within 7 days of immersion in SBF with Ca/P molar ratio of 3.8-5.7. • Non-toxic to MG-63 osteoblast-like human cell lines, indicating biocompatibility and potential for biomedical applications.	[61]

Continued on next page

Table 2.1 – *Continued from previous page*

Composition	**Resources**	**Remarks / Key Findings**	**Reference**
$60SiO_2$-$15Na_2O$-$22CaO$-$3P_2O_5$	Agro-food waste	• Bioactive glasses synthesized using rice husk-derived silica showed superior biocompatibility and antibacterial activity compared to quartz-based and conventional 45S5 bioglass. • Antioxidant and cytotoxicity assays indicate the biocompatibility of bioglasses. • *in-vivo* wound healing studies carried out in the rat model demonstrated the rapid wound healing properties of the rice husk-derived silica bioglass.	[174]
(60)CA-(10)SA-(30)ES (wt%)	Agro-food waste	• Synthesized bioactive glasses via melt-quench using CHA, SCA, and ES. • Confirmed formation of diopside and cristobalite phases. • Cauliflower and flake-like HAp morphology observed after 7 days in SBF with Ca/P ratio: 1.6–3.9. • Biocompatible with MG-63 cells. • Heat treatment of soaked glasses converted amorphous HAp to crystalline HAp and diopside phase	[168]
40 B_2O_3–$(20-x)$ CaO–$25Li_2O$–15 P_2O_5–x MgO (x= 0–3 mol%)	Conventional	• Borophosphate glasses doped with MgO were synthesized. • MgO promotes glass degradation by opening the network structure. • Increased Ca/P ratio was observed after immersion in SBF with increasing MgO content. • Highest hardness and lowest wear rate observed at 3 mol% MgO. • Indicates good biocompatibility and suitability for bone filling and wound healing applications.	[175]

Continued on next page

Table 2.1 – *Continued from previous page*

Composition	**Resources**	**Remarks / Key Findings**	**Reference**
$85SiO_2$–$(15-x)$CaO -xMgO (x = 1, 3, 5, 10 mol%)	Conventional	• Synthesized Mg-doped binary bioglass nanoparticles via sol–gel. • Increasing Mg content increased surface area and porosity, enhanced dissolution rate, and retarded crystallization of the apatite phase in SBF. • Higher Mg content also improved drug release kinetics but decreased drug loading efficiency. • Glass with 5mol% MgO showed optimal bioactivity. • Nanoparticles exhibited a spherical morphology with a mesoporous structure.	[176]
ZnO/MgO-CaO-SiO_2-P_2O_5	Conventional	• Synthesized bioglass via sol-gel method. • Mg-containing glass exhibited enhanced interaction with SBF and higher mineralization compared to Zn-containing glass. • Incorporation of Zn^{2+} and Mg^{2+} ions improved both biocompatibility and antibacterial properties.	[177]
24.4K_2O-26.9CaO-46.1SiO_2-2.6P_2O_5 mol%	Conventional	• Synthesized a bioactive glass by replacing Na_2O with K_2O in the 45S5 composition and sintered it to a glass-ceramic. • Glasses exhibited good densification, mechanical strength, and bioactivity comparable to 45S5 Bioglass®. • Elastic modulus was lowered to 56 GPa. • Increasing K_2O content enlarged the sintering window. • Two-step sintering promoted crystallization and further improved mechanical properties.	[178]

Continued on next page

Table 2.1 – *Continued from previous page*

Composition	**Resources**	**Remarks / Key Findings**	**Reference**
$53.9SiO_2$-$1.7P_2O_5$-$21.8CaO$-$(22.7-x)Na_2O$-xK_2O (x=0−22.7) mol%	Conventional	• Mixed alkali effect was observed on thermal and dissolution properties of a series of glasses. • The maximum MAE was observed near 20% K_2O replacement, resulting in the lowest sintering and crystallization temperatures and the narrowest processing window. • Higher K_2O substitution increased the hot-working range and decreased glass density due to network expansion. • Bioactivity decreased with K_2O substitution beyond 40%. • Pure K_2O glass showed promising bioactivity and a low tendency for crystallization.	[165]
$51SiO_2$-$18CaO$-$20Na_2O$-$4P_2O_5$-$7MgO$ mol%	Conventional	• Synthesized Mg-doped MBG nanoparticles (∼ 65 nm) via a template-assisted sol-gel method. • The resulting material exhibited a high surface area (327 m^2/g) and pore size in nm. • Good apatite formation was confirmed after immersion in SBF. • Efficient drug loading and pH-dependent sustained release of Mitomycin C were achieved, with an IC50 of 20.8 μg/mL against cancer cells.	[154]
$49SiO_2$-$20CaO$-$20Na_2O$-$7K_2O$-$4P_2O_5$ mol%	Conventional	• Synthesized bifunctional mesoporous bioactive glass (MBG) via sol-gel. • The resulting material consisted of spherical particles (∼ 1 µm) with a surface area of 189.53 m^2/g and pore size of 21 nm. • XRD analysis confirmed hydroxyapatite formation after SBF immersion. • Non-toxic at concentrations up to 80 µg/mL. • Promoted osteoblast activity and bone mineralization. • Sustained antibiotic release (ciprofloxacin) of up to 90% over two weeks. • Good biomedical properties, confirmed by both animal and cytotoxicity studies.	[171]

Based on the literature survey, the motivation and objectives of the present study are as follows.

2.6 Motivation of the study

The development of sustainable and biocompatible materials is a critical area of research in biomedical engineering, driven by the increasing demand for environmentally friendly solutions. Bioactive glasses, with their proven efficacy in bone regeneration and tissue repair, have garnered significant attention. While extensive research has explored synthesizing bioactive glasses from conventional sources, utilizing agro-food waste as a sustainable alternative presents a compelling opportunity. This approach not only reduces environmental impact but also creates value from the wastes. As detailed in this literature review, considerable progress has been made in utilizing agro-food waste, particularly rice husk ash (RHA) and eggshell powder (ESP), as sustainable precursors for bioactive glass synthesis. These studies demonstrate the feasibility of producing bioactive glasses with comparable or even enhanced properties compared to conventionally derived materials. However, a significant gap in research exists regarding the systematic exploration of hybrid bioglass systems combining agro-food waste-derived (SiO_2, CaO) and conventional mineral oxides such as P_2O_5 and Na_2O. Existing research primarily focuses on using agro-food wastes either as the sole raw material or as silica sources alongside conventional oxides, with limited exploration of hybrid systems. To the best of our knowledge, no studies have reported bioactive glasses derived from both rice husk ash and eggshell powder as sustainable and environmentally friendly sources of silica and calcium, respectively, with systematic variations of the substitution of MgO for CaO and K_2O substituting for Na_2O in 45S5 bioglass for biomedical applications.

This identified gap and the potential for developing novel bioactive glasses with tailored properties and improved bioactivity and biocompatibility are the primary motivations for the present study. This research aims to contribute to a more sustainable biomaterials industry while advancing innovative solutions for bone regeneration and tissue repair by systematically investigating the effects of these compositional modifications and utilizing readily available agro-food waste resources.

Based on the above observations and literature survey, the following objectives are proposed for the present study.

2.7 Objectives

- Synthesis and characterization of $43SiO_2$+(25-x)CaO+(25-y) Na_2O+xMgO+ yK_2O+$7P_2O_5$ (x= 0,5,10, and 15; y= 0, 5,10 and 15) (wt%) glasses.
- In-vitro synthesis and characterization of hydroxyapatite layer on developed glass and glass ceramics.
- Evaluation of cytotoxicity of selected glass and glass ceramics.
- Comparison of hybrid source derived and conventional chemicals derived bioactive glasses.

CHAPTER 3

Materials and Methods

Overview

This chapter details the synthesis methodology and characterization techniques used for silicate-based glasses derived from hybrid resources, incorporating both agro-food waste (rice husk ash and eggshells) and conventional chemicals. The structural, thermal, microstructural, and physicochemical properties of the as-prepared glasses were investigated. Crucially, their bioactivity and biocompatibility, assessed using simulated body fluid (SBF) and human peripheral blood mononuclear cells (PBMCs), respectively, were evaluated to determine their suitability for biomedical applications. The synthesis procedure, characterization techniques, and testing methodologies, including the specific conditions and parameters for each analysis, are comprehensively described.

Agro-food wastes, such as rice husk ash and eggshells, represent a valuable source of elements with potential applications in various fields, particularly biomedicine. Careful selection and processing of these wastes are crucial for obtaining elements suitable for transforming them into valuable resources for various applications.

3.1 Agro-food wastes as raw materials

The present study aims to synthesize bioactive calcium silicate glass compositions from hybrid sources, that is, agro-food waste ashes and conventional chemicals. Rice husk (RH) was collected from a local rice mill in Patiala, Punjab, India. The obtained RH was initially cleaned to remove soil particles or remaining rice straws. Furthermore, it was washed with normal water to remove any remaining dust. The dried RH was used to obtain RHA. Further, RHA was calcined using two different heat treatments to obtain silica (SiO_2). The RHA was first calcined at 1250 ^oC for 4 h (As shown in **Fig. 3.1**), followed by heat treatment at 1450 ^oC for 4 h. Chicken eggshells (ES) were obtained from the hostel of the Thapar Institute of Engineering and Technology, Patiala, Punjab, India. The eggshells were washed with distilled water to remove impurities and kept in a 1M HCl solution for 2 h, followed by washing with distilled water. Then, ES were kept in the oven at 70 °C for 6 h to remove any moisture from the eggshell. Finally, eggshells were ground in an agate mortar to convert into powder.

The purity of SiO_2 and $CaCO_3$, determined using energy-dispersive X-ray spectroscopy (EDS) with Quantax Esprit software (Bruker microanalysis), was found to be 97.7 wt% and 98 wt%, respectively, with trace elements listed in **Table 3.1**. These sustainable sources, obtained from agro-food wastes and other required conventional chemicals such as Na_2O, P_2O_5, MgO, and K_2O, were used to synthesize the bioactive glasses according to the objectives. Details of the glass synthesis, characterization, and testing procedures are provided in the following sections.

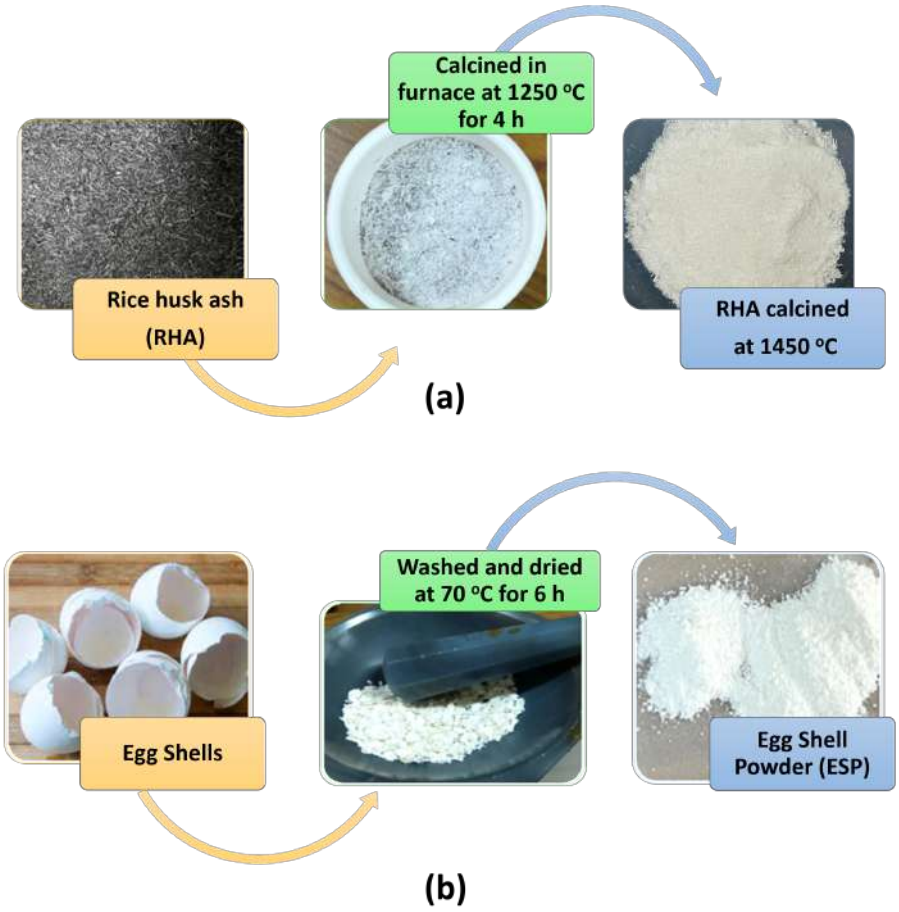

Figure 3.1: Flow chart of the conversion of (a) RHA into silica (b) Egg shells into $CaCO_3$

Table 3.1: The elemental composition (wt%) obtained from EDS of the heat-treated RHA and ESP, with mean ± standard deviation (n=3)

Elements	RHA	Eggshell powder
Si	41.3 ± 6.0	—
Ca	0.73 ± 0.2	34.8 ± 6.0
O	61.8 ± 6.4	59.8 ± 2.2
C	—	20.9 ± 2.7
Mg	0.18 ± 0.1	0.06 ± 0.03
Al	0.03 ± 0.05	—

3.2 Synthesis of bioactive glass

Bio-active glasses can be synthesized by using different techniques, such as melt quenching, sol-gel, chemical deposition, and co-precipitation methods etc. The first ever 45S5 bioglass was synthesized using the traditional melt- quenching method [179]. However, melt quenching and sol-gel are the well developed

and prominent methods used for the preparation of bioactive glasses. Each and every synthesis technique has merit and demerit. In the present case, the conventional melt quench technique has been adopted to synthesize the glasses.

The first series of glass compositions was synthesized to study the effect of MgO substitution on bioactivity. The selected compositions were as follows: **$43SiO_2$-$25Na_2O$-$7P_2O_5$-(25-x)CaO-(x)MgO (x = 0, 5, 10, and 15 wt%)**. The derived SiO_2 and $CaCO_3$ from RHA and ESP, respectively, were combined with the conventional chemicals (Na_2CO_3, P_2O_5, MgO) in the desired proportions. The conventional chemicals such as sodium carbonate (Na_2CO_3) with 99.99% purity (Loba Chemie), phosphorus pentoxide (P_2O_5-99.99%, Loba Chemie), magnesium oxide (MgO-99.99%, Loba Chemie) were used as the conventional chemicals. These were used without any further purification. The blended mixture of conventional chemicals and agro-food waste-derived SiO_2 and $CaCO_3$ was homogenized by grinding for 2 h in an acetone medium. To remove any residual carbonates, the mixture was calcined at 1000 ^oC for 2 h. The calcined material was then grinded again for 1 h. The grinded, calcined mixture was heated in a platinum-rhodium crucible within an electronic furnace (Okay model with $MoSi_2$ heating elements) at a rate of 5 °C/min. The mixture was held at intermediate temperatures (300 °C, 600 °C, 900 °C, and 1200 °C) for 0.5 h each to promote diffusion and minimize volatilization of certain components before finally being melted at 1550 °C. The melt was then air-quenched using two thick (6.84 mm) copper plates.

Second series of glass compositions was synthesized to investigate the effect ofK_2O in place of Na_2O. In this series, Na_2O was incrementally replaced with K_2O in the following compositions: **$43SiO_2$-$25CaO$-$7P_2O_5$-(25-y)Na_2O-(y)K_2O (y = 0, 5, 10, and 15 wt%).** The same procedure as described for the first series was used to synthesize these glasses. The nominal composition of all the glass samples along with their labels are given in **Table 3.2**.

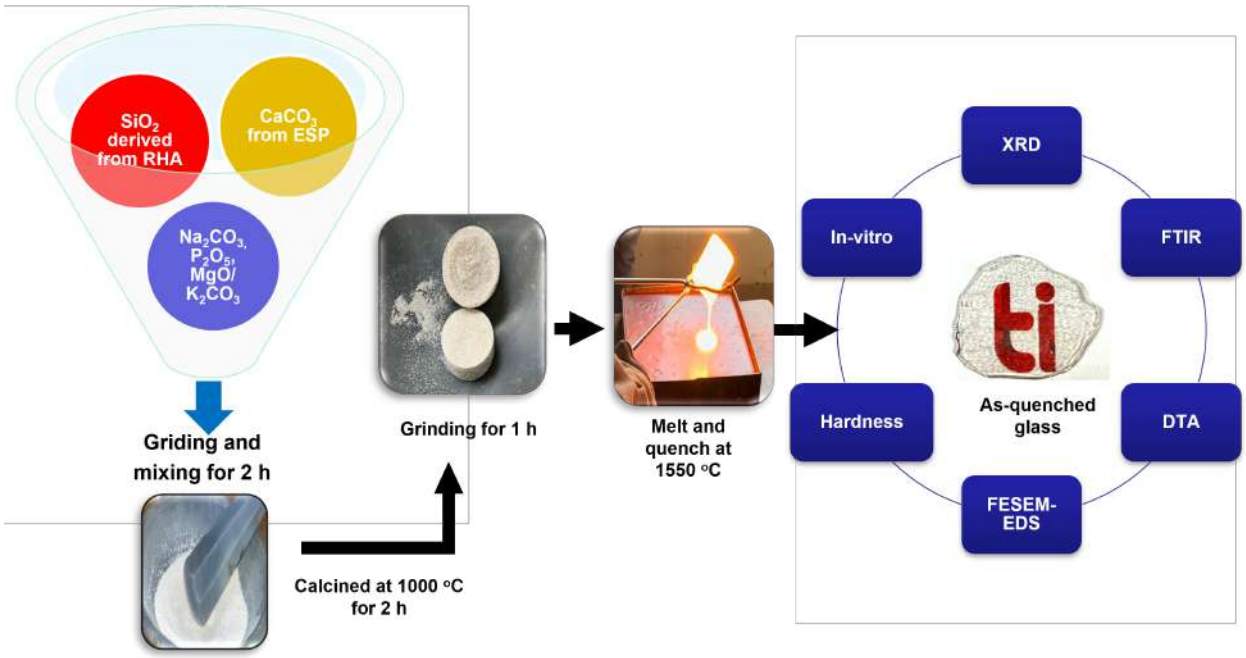

Figure 3.2: Flowchart illustrating the steps in the melt-quench synthesis of glass

Table 3.2: Glass labels and nominal composition used for different glasses in wt%

Glass ID	Elements					
	SiO_2	CaO	Na_2O	P_2O_5	MgO	K_2O
SC-O	43	25	25	7	–	–
SCM-5	43	20	25	7	5	–
SCM-10	43	15	25	7	10	–
SCM-15	43	10	25	7	15	–
SNK-5	43	25	20	7	–	5
SNK-10	43	25	15	7	–	10
SNK-15	43	25	10	7	–	15

Based on the best results obtained from the first and second glass series (as discussed in Chapter 4), three additional glasses were synthesized using only conventional chemical precursors. The synthesis procedure remained consistent with that in the earlier series. The compositions of these glasses are as follows: **$43SiO_2$–25CaO–$25Na_2O$–$7P_2O_5$, $43SiO_2$–10CaO–15MgO–$25Na_2O$–$7P_2O_5$**, and **$43SiO_2$–25CaO–$10Na_2O$–$15K_2O$–$7P_2O_5$** in (wt%), designated as MS-0, MM-15, and MK-15, respectively.

3.3 Characterization methods

3.3.1 Density measurement

Density is a crucial parameter that provides insights into the compactness, porosity, and interconnectivity of the glass structure [180]. This directly influences the bioactivity of glasses, affecting both their degradation rate and interaction with surrounding tissues. In the present study, density (ρ) of the as-quenched glasses was determined using Archimedes' principle with xylene using as buoyant medium:

$$\rho_{\text{sample}} = \frac{W_a}{W_a - W_x} \times \rho_{\text{sample}} \tag{3.1}$$

where, ρ_{sample} and ρ_{xylene} are the density of sample and xylene, respectively. W_{a} and W_{x} are the weight of the sample in air and xylene, respectively. The density of xylene is 0.863 g/cm^3 at room temperature (30 $^{\text{o}}$C). Other parameters such as molar volume (V_{m}), and oxygen packing density (OPD) were also deduced from the calculated density, using standard equations as given below:

$$V_m = \frac{M}{\rho_{\text{sample}}} \tag{3.2}$$

$$\text{OPD} = C \times \frac{\rho_{\text{sample}}}{M} \tag{3.3}$$

Where C is the number of oxygen atoms per formula unit.

3.3.2 X-ray diffraction (XRD)

XRD is a non-destructive technique widely used to characterize materials' structural properties, including identifying amorphous or crystalline phases. In the present study, the XRD was performed on the as-prepared samples as well as after immersion in simulated body fluid (in-vitro testing) to confirm the amorphosity, nanocrystallinity, and hydroxyapatite (HAp) formation, respectively. The principle of XRD relies on the interaction of X-rays with the arrangement of atoms in a crystalline lattice [181]. This ordered arrangement creates planes with characteristic interplanar spacings (d-spacing). When X-

rays interact with these planes, diffraction occurs according to Bragg's law:

$$2dsin\theta = n\lambda \tag{3.4}$$

where 'n' is the order of reflection, λ is the X-ray wavelength (0.1-4 Å), and θ is the diffraction angle. Constructive interference from diffracted X-rays results in diffraction peaks, which are analyzed to identify the crystalline phases. In a typical X-ray diffractometer, monochromatic X-rays are generated by a cathode ray tube, filtered by crystal monochromators, collimated, and directed onto the sample. As the sample and detector rotate, the intensity of reflected X-rays is recorded. When the incident X-rays' geometry satisfies Bragg's law, constructive interference occurs, producing diffraction peaks. A detector records and processes these X-ray signals, converting them into counts per second, and the output is displayed on a computer monitor (e.g., as shown in **Fig. 3.3**).

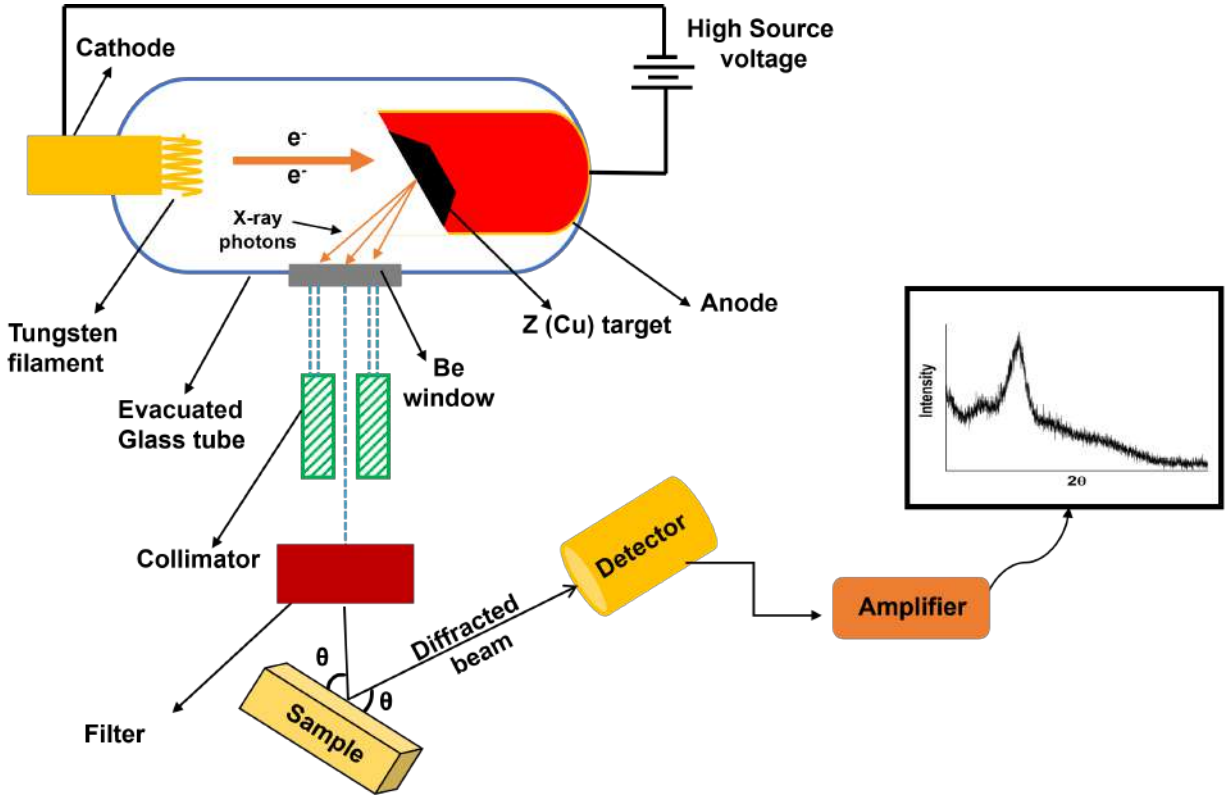

Figure 3.3: Schematic representation of X-ray production, instrument, and use for identification of the glass nature

As the glasses lack long-range atomic order, they exhibit broad halo patterns

in XRD instead of sharp diffraction peaks. The halo's position is composition-dependent, and multiple halo's may indicate phase separation or inhomogeneity in the glass [182]. In contrast, glass ceramics, which possess partial crystallinity, exhibit both broad halo and crystalline peaks embedded over the glass matrix in the glass. XRD analysis provides crucial information on the crystalline phases formed during heat treatment or after immersion in SBF, which is essential to understand the bioactivity of these materials.

In this study, XRD patterns were acquired using a Rigaku Smartlab SE X-ray diffractometer with a Cu-Kα source (λ = 1.54 Å). Measurements were performed in air over a 2θ range of 10-90° with a scanning speed of 4°/min and a step size of 0.02°. Phase identification was carried out using X'Pert HighScore Plus software. Samples were analyzed in their as-quenched state, both before and after SBF immersion (in-vitro testing).

3.3.3 Differential thermal analysis (DTA)

DTA is a crucial technique for assessing the thermal behavior of materials, providing insights into thermal stability and characteristic temperatures such as the T_g and T_c. These characteristic temperatures are essential for understanding material properties and processing parameters [183]. For bioactive glasses, T_g and T_c are particularly important as they influence the sintering and crystallization behavior during the fabrication of glass-ceramics, which can significantly impact the final material's bioactivity. Many processes, such as coating and enameling, involve subjecting the glass to high temperatures, often near or exceeding the crystallization temperature (T_c) [146]. Therefore, determining the thermal stability of the glass through DTA is essential.

In DTA, the sample and an inert reference (e.g., Al_2O_3) are subjected to identical thermal cycles, and the temperature difference (ΔT) between them is continuously monitored. This difference is plotted against temperature, producing a DTA curve (thermogram). Endothermic and exothermic peaks on the thermogram correspond to physical or chemical changes in the sample, such as glass transition, crystallization, melting, and other phase transitions. A typical DTA setup (e.g., as depicted in **Fig. 3.4**) includes a furnace, sample and

reference holders equipped with thermocouples, and a recording system. The differential arrangement of thermocouples, connected to a differential amplifier, allows for precise measurement of the temperature difference between the sample and reference, enabling the detection of even subtle thermal events.

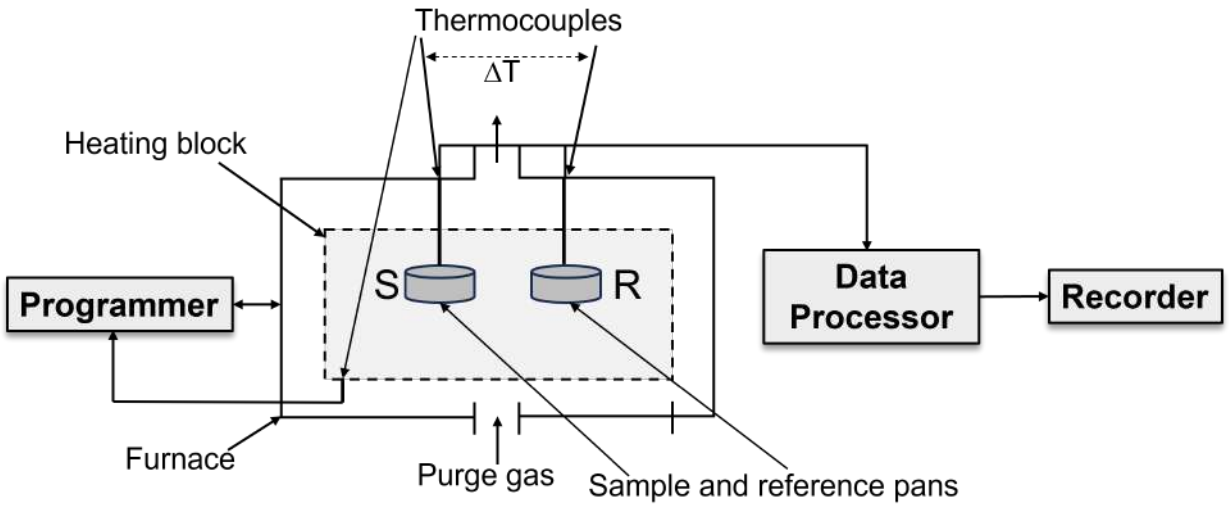

Figure 3.4: Schematic illustration of the basic assembly of differential thermal analyzer

In this study, DTA was performed using a Perkin Elmer Diamond Pyris TG/DTA instrument. Approximately 15 mg of glass powder was placed in a Pt crucible, with Al_2O_3 (99.9% pure) as the reference material. The T_g and T_c were determined from DTA curves obtained in the 20–1000°C range at a heating rate of 15°C/min. The softening temperature (T_s) and thermal expansion coefficient (TEC) of all the glasses were determined via dilatometric measurements using a Netzsch DIL402PC dilatometer at a heating rate of 5°C/min in air. The temperature measurements were accurate to within ±1°C.

3.3.4 Scanning electron microscopy (SEM) and energy dispersive spectroscopy (EDS)

SEM, coupled with EDS, played a crucial role in characterizing the synthesized glasses and glass-ceramics before and after immersion in SBF. SEM generates high-resolution images by scanning a focused electron beam across the material's surface. The interaction of the electrons with the sample produces various signals, including secondary electrons (SE), backscattered electrons (BSE), and characteristic X-rays, which provide information about surface topogra-

phy, elemental distribution, and composition, respectively [184]. A schematic of the SEM principle is shown in **Fig. 3.5**. Field emission scanning electon microscopy (FESEM) is a similar instrument to SEM; it provides enhanced resolution (down to 1.5 nm) up to three to six times better than conventional SEM and provides clearer and less distorted images [185].

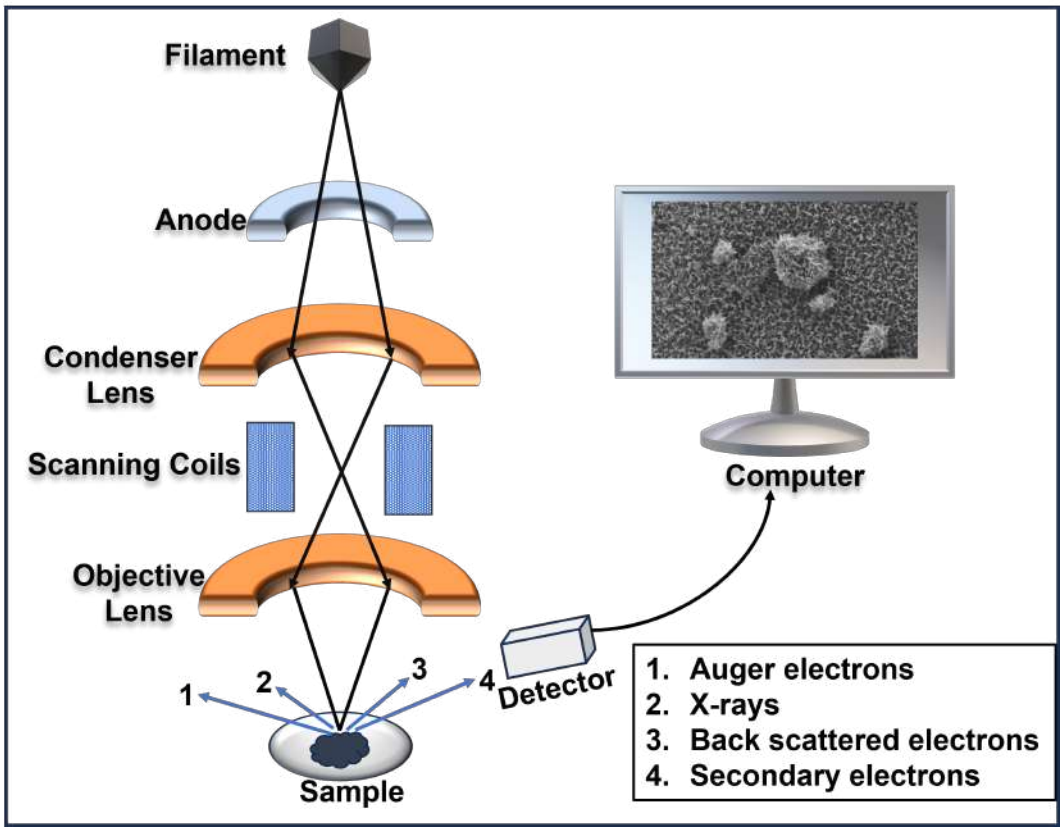

Figure 3.5: Schematic diagram of scanning electron microscopy

EDS, integrated with SEM, provides elemental analysis of the sample. When the high-energy electron beam of the SEM interacts with the sample, it causes the ejection of inner-shell electrons from atoms within the sample, creating vacancies (as shown in **Fig. 3.6 b**). These vacancies are quickly filled by outer-shell electrons, releasing energy in the form of characteristic X-rays unique to each element. An energy-dispersive X-ray (EDX) detector measures these X-rays, allowing for the identification and quantification of the elements present [186]. This is essential for verifying the composition of the synthesized glasses and confirming the presence and relative amounts of key oxides. In the context of bioactivity assessment, SEM-EDS is particularly valuable. After SBF immersion, SEM allows for direct visualization of hydroxyapatite (HAp) formation on the material's surface, providing insights into the morphology of the HAp layer, including its thickness, density, and crystallinity. EDS is crucial for determining the Ca/P ratio within the HAp layer, a key indicator of bone-bonding potential. A Ca/P ratio close to that of natural bone apatite (approximately 1.67) is considered desirable for good bioactivity. Furthermore, SEM-EDS can be used to identify different phases formed in glass-ceramics, as well as to track elemental changes during degradation studies.

For the present study, SEM micrographs were obtained using a JEOL/EO SEM (version 1.0). Samples were coated with gold (Au) using a JEOL JEC-3000 FC auto fine coater at 20 mA for 60 seconds. Higher-resolution imaging was performed using a Zeiss Sigma 500 field emission scanning electron microscope (FE-SEM). Elemental analysis was conducted via energy-dispersive X-ray spectroscopy (EDS) using a Bruker Quantax XFlash 6130 detector on the FE-SEM, operating in low vacuum mode.

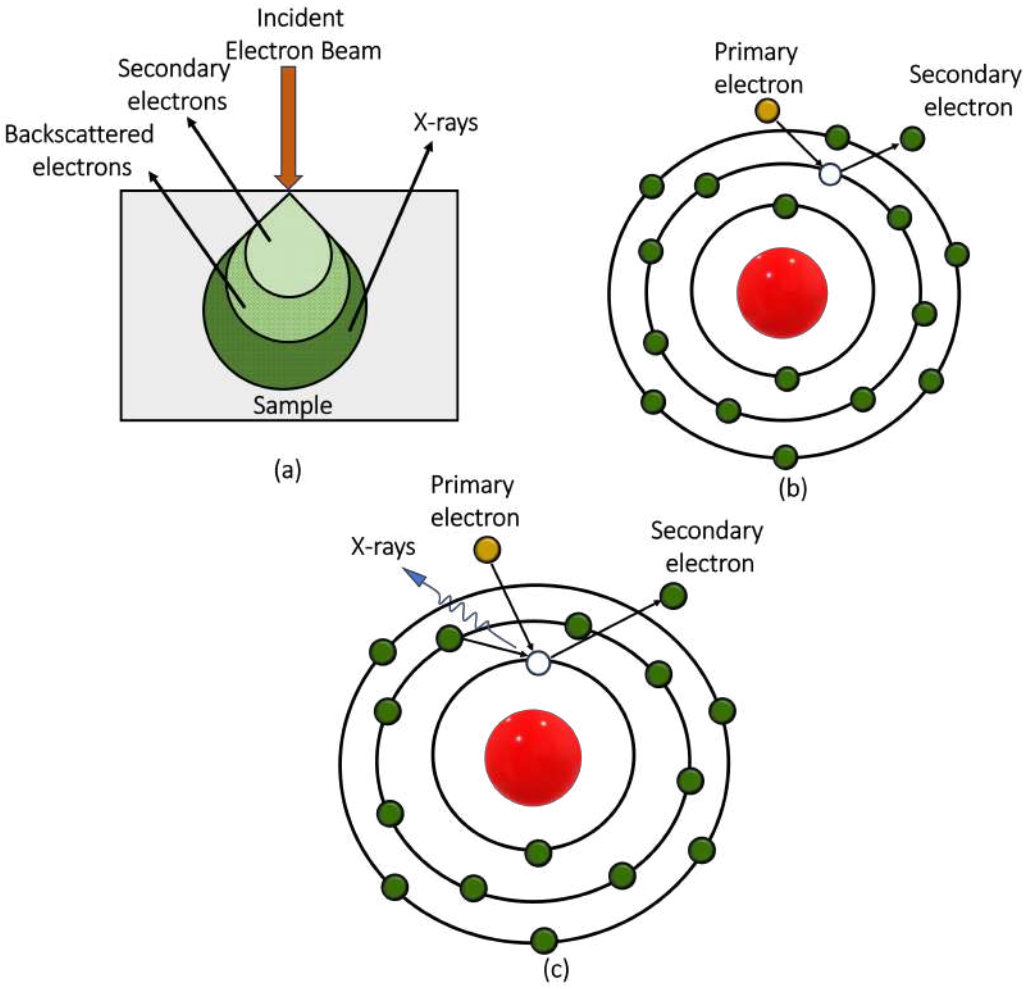

Figure 3.6: Schematic illustration of (a) interaction between electron beam and specimen in SEM (b,c) formation mechanism of SE, and Characteristic X-rays

3.3.5 Fourier Transform Infrared Spectroscopy (FTIR)

Infrared spectroscopy is a crucial analytical technique in materials science, based on the principle of molecular vibrations. When infrared radiation interacts with a sample, specific wavelengths are absorbed, corresponding to the vibrational frequencies of the material's structural units, while the remaining radiation is transmitted. The infrared spectrum is broadly divided into three regions: far-infrared (< 400 cm^{-1}), mid-infrared (4000-400 cm^{-1}), and near-infrared (13000-4000 cm^{-1}). A change in the electric dipole moment during vibration is essential for infrared absorption [187]. FTIR spectroscopy, the most common infrared method, employs the interference of two beams to generate an interferogram, a signal based on the path length difference between the

beams. Fourier transformation converts this signal from the distance domain to the frequency domain (wavenumber). The resulting spectrum, displaying transmittance as a function of wavenumber, is then analyzed by assigning specific bands to the vibrations of distinct structural units. This unique spectral fingerprint allows for the identification of a sample's structural components and can even be used to evaluate bond strength. Overlapping bands can be resolved using deconvolution, a signal processing technique that enhances spectral resolution [188].

FTIR spectroscopy is particularly valuable for analyzing bioactive glasses and glass-ceramics, both before and after immersion in SBF. A key aspect of bioactivity is the formation of silanol groups (Si-OH^-) when exposed to physiological fluids. Network modifiers within the silica network disrupt the tetrahedral SiO_4 units, breaking Si-O-Si bonds and forming Si-O-NBO groups. This process, coupled with silicate network dissolution, is crucial for bioactivity. FTIR spectroscopy, sensitive to these vibrational mode changes, provides insights into these structural transformations. Analyzing the Si-O-Si and Si-O-NBO absorption bands reveals information on network connectivity and the influence of modifiers [189]. Each glass composition's unique infrared absorption spectrum serves as a fingerprint, facilitating the identification and comparison of different structures. Comparing spectra before and after SBF immersion allows for identifying structural changes such as hydroxyapatite (HAp) formation or alterations in the glass network, which elucidates the bioactivity mechanism.

In this study, FTIR analyses were conducted using an IRTracer-100 spectrometer (Shimadzu Corporation, Japan). Spectra were recorded in the 400–4000 cm^{-1} range with a 2 cm^{-1} resolution using the KBr pellet method (0.5 mg sample mixed with 200 mg KBr). Data analysis, including deconvolution of overlapping bands, was performed using Origin 2018 software. The accuracy of the Gaussian fitting during deconvolution was assessed by maximizing R-squared ($R^2 > 0.999$) and minimizing reduced chi-square ($\chi^2 \sim 10^{-7}$) values.

3.3.6 Vickers Microhardness

Vickers microhardness measurements were performed on the as-quenched samples using a Mitutoyo MVK-H0 microhardness tester (Japan) equipped with a diamond Vickers indenter. Indentations were made at four different points on each sample surface using an applied load of 100 gram-force (gf) for a dwell time of 15 seconds as shown in **Fig. 3.7**. The indentations were made on the as-prepared sample surfaces without prior polishing. A light microscope (Eclipse-MA100, Nikon, Tokyo, Japan) at 100x magnification was used to measure the lengths of both diagonals immediately after indentation. Three indentations were made at each of the four points to minimize error, and the average diagonal length was used for the calculations.

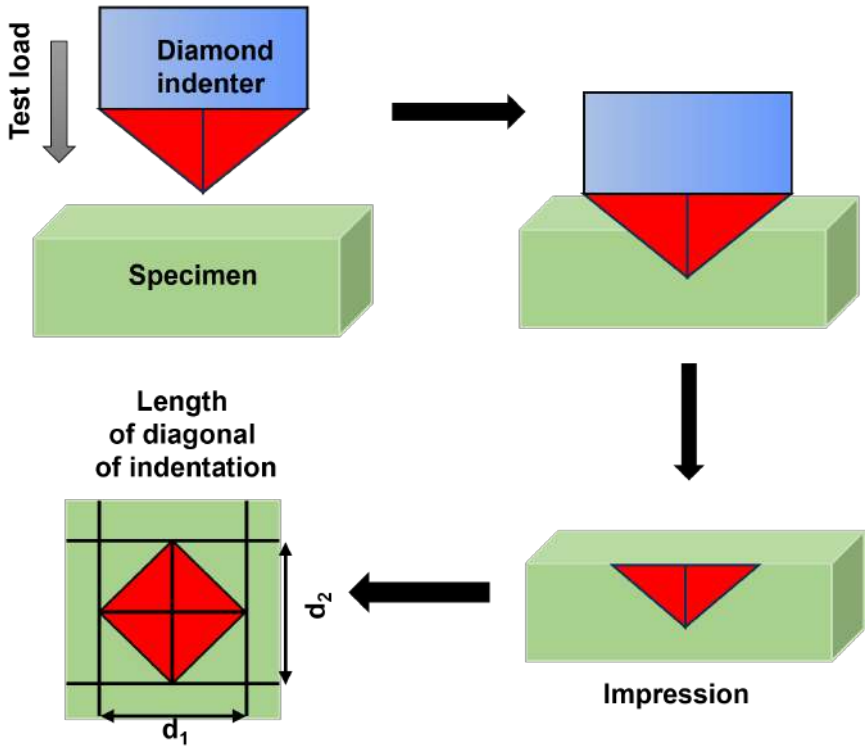

Figure 3.7: Schematic representation of the Vickers hardness measurement

The Vickers microhardness (HV) was calculated using the following equation:

$$HV = \frac{1.854L}{d^2} \tag{3.5}$$

where L is the applied load (gf) and d is the average diagonal length (mm) of the indentation.

3.4 Characterizations for bioactive properties

In addition to the characterization techniques mentioned above, further analyses are necessary to explicitly confirm the bioactivity phenomenon discussed in this section.

3.4.1 In-vitro testing

In-vitro bioactivity and degradation of the powdered glass samples were assessed using SBF. The SBF solution was prepared according to Kokubo's protocol [18] using high-purity NaCl, $NaHCO_3$, KCl, $K_2HPO_4{\cdot}3H_2O$, $MgCl_2{\cdot}6H_2O$, $CaCl_2$, and Na_2SO_4 dissolved in deionized water. The pH was maintained at approximately 7.34 (within the normal range of human blood plasma) using 50 mM Tris-hydroxymethyl aminomethane ($(CH_2OH)_3CNH_2$) and 45 mM HCl. A weight (powder sample) to volume (SBF solution) ratio of 0.02 g/mL was maintained [161][190]. Similar ratios have been employed in previous studies to promote observable apatite formation in glass systems exhibiting slower dissolution kinetics or partial crystallinity [190]. One gram of each glass powder was immersed in 50 mL of SBF in polyethylene bottles under static conditions and incubated at 37 °C for 2, 5, 10, 20, and 40 days.

SBF pH was monitored daily using a digital pH meter (P Hep model HI96107, precision 0.1). Samples were collected after 2, 5, 10, 20, and 40 days of immersion, filtered, dried at room temperature, and weighed using a Mettler Toledo precision microbalance to determine weight loss (W_c) according to the following equation:

$$W_c\% = \frac{W_0 - W_f}{W_0} \times 100 \tag{3.6}$$

Where W_0 and W_f are the initial and final weights of the sample, respectively. Immersed samples were characterized using XRD, FTIR, and SEM-EDS and compared to pristine (unsoaked) samples. The residual SBF was analyzed using microwave plasma atomic emission spectroscopy (MP-AES) to determine the elemental release profile.

3.4.2 Microwave plasma-atomic emission spectroscopy (MP-AES)

MP-AES is a highly sensitive elemental analysis technique that is valuable in various applications. In the present bioactive study, MP-AES is used for the quantification of trace elements released from the samples, providing insights into the dissolution behavior of the material and corroborating observed changes in the pH of the SBF and the sample weight. A magnetron and a waveguide are major components of the instrument. The magnetron generates electromagnetic energy (3.5 GHz), which is transferred to a waveguide assembly and focused onto a plasma torch [191]. The sample, introduced into the plasma via a nebulizer, is atomized and excited by the microwave-generated nitrogen plasma. This excitation causes the atoms to emit light at characteristic wavelengths, which are then detected by the solid-state charge-coupled device (CCD) detector, and used to quantify the elemental concentrations, even at very low levels (parts per billion).In the present bioactive study, MP-AES serves as a complementary technique, providing detailed elemental release profiles (up to ppb levels) to corroborate the observed pH and weight changes in the immersed samples.

In the present work, an Agilent 4100 MP-AES system (spectral resolution: 25-40 pm) was used to quantify ion concentrations leached from the samples into SBF. Samples (0.1 g) were dissolved in 1N HNO_3 (10 mL) and water (25 mL), heated to reduce volume by 50%, and then diluted with 100 mL of water. All measurements were performed in triplicate and average values were used for final analysis.

3.5 Biocompatibility test

3.5.1 MTT assay

The cytotoxicity of all glass samples were evaluated using the MTT (3-(4,5-dimethylthiazol-2-yl)-2,5-diphenyltetrazolium bromide) assay with human peripheral blood mononuclear cells (PBMCs) [192]. PBMCs were isolated from healthy volunteer blood using density gradient centrifugation with HiSep^{TM} LSM1077 (HiMedia, India), following the standard method. The isolated cells

were washed with phosphate-buffered saline (PBS). Again these cells were re-suspended in Dulbecco's Modified Eagle Medium (DMEM, HiMedia, India) supplemented with 5% fetal bovine serum, 100 UI/mL penicillin, 100 µg/mL streptomycin, and 25 µg/mL amphotericin B. Cells were seeded in a 96-well plate at a density of 4×10^5 cells/well. The schematic illustration of the MTT assay is shown in **Fig. 3.8**.

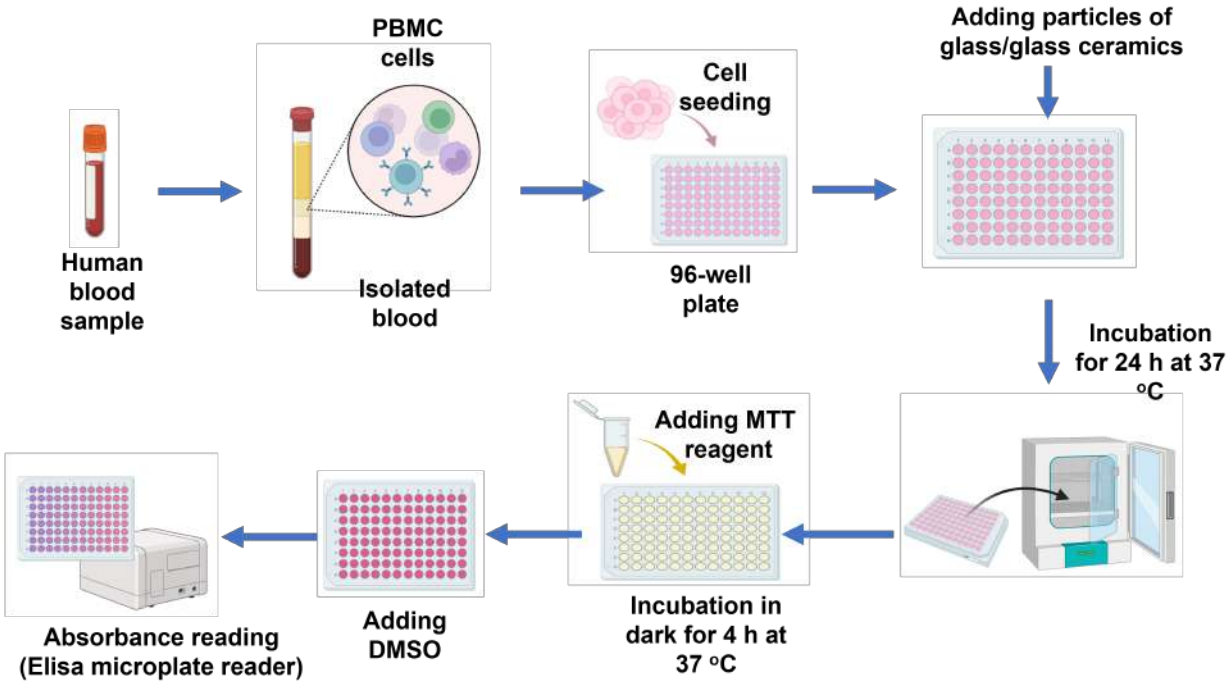

Figure 3.8: Schematic illustration of the MTT assay for cell viability assessment

For dose-response assessment, cells were treated with varying sample concentrations (0-200 µg/mL) for 24 h in a humidified incubator at 37°C with 5% CO_2. Based on these results, a concentration of 100 µg/mL was selected for time-dependent cytotoxicity assessment over 48 h. Following incubation, 200 µL of supernatant was removed, and 20 µL of MTT solution (5 µg/mL) was added to each well. After 4 h of incubation in the dark, 150 µL of DMSO was added to each well, and the absorbance was measured at 540 nm using an Infinite Pro ELISA reader. Cell viability was calculated relative to untreated controls:

$$\text{Viability (\%)} = \frac{\text{OD of treated cells}}{\text{OD of control}} \times 100 \tag{3.7}$$

Experiments were performed in triplicate with three independent biological replicates. Results are presented as mean ± standard deviation. Statistical analysis was performed using one-way ANOVA with Tukey's multiple comparison test (GraphPad Prism, GraphPad Software, Inc., San Diego, CA).

CHAPTER 4

Results and Discussion

Overview

This chapter presents the synthesis, characterization, and in-vitro assessment of three bioactive glass series prepared via the melt-quench method. The first series investigated the substitution of CaO with MgO ($43SiO_2$-$25Na_2O$-$7P_2O_5$-(25-x)CaO-(x)MgO, x = 0, 5, 10, and 15 wt%) while the second explored the replacement of Na_2O with K_2O ($43SiO_2$-$25CaO$-$7P_2O_5$-(25-y)Na_2O-(y)K_2O, y = 0, 5, 10, and 15 wt%), initially using hybrid sources (RHA and eggshell powder) combined with conventional chemicals. Different characterization techniques were used to determine the change in properties of the glasses before and after immersion in SBF. The MgO substitution improved the compactness and thermal stability, while K_2O decreased density and reduced phase separation in the glasses. Both modifiers increased the glass sintering window and resulted in increased hardness values ranging from 4.6 to 6.2 GPa. In-vitro testing in SBF showed that MgO initially retarded but later stabilized c-HAp formation, while K_2O promoted faster c-HAp growth. All glasses indicate good cytocompatibility (MTT assay with PBMCs) with >85% cell viability. Based on the results, the best glasses were synthesized using only conventional chemicals for comparison of the results. The results indicate a higher hardness and faster HAp formation but lower cytocompatibility at higher concentrations than their hybrid-source-derived counterparts.

4.1 $43SiO_2$-$25Na_2O$-$7P_2O_5$-(25-x)CaO-(x)MgO (x = 0, 5, 10, and 15 wt%)

4.1.1 Compositional analysis of as-quenched glasses

EDS analysis was used to determine the elemental composition of the as-quenched glasses. The measured compositions were consistent with the nominal compositions of the glasses. **Table 4.1** presents the elemental compositions (wt%) determined by EDS, with associated standard deviations (n=8). A representative EDS spectrum for the SC-0 glass is shown in **Fig. 4.1**.

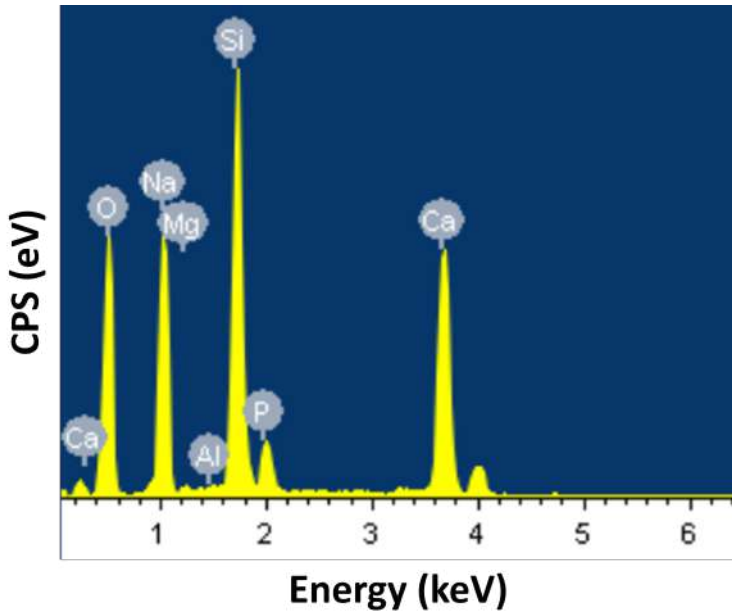

Figure 4.1: A representative EDS spectrum of as-synthesized SC-0 glass indicating the presence of different elements in glass

As observed in (**Fig. 4.1** and given in **Table 4.1**), MgO was also observed in the SC-0 glass, however MgO is not added in the nominal composition. Furthermore, Al_2O_3 was also detected with the level below $\sim$ 1 wt%. The presence of these trace elements MgO and Al_2O_3 is attributed to impurities in the starting materials of bio-wastes, as has been widely reported for agro-food waste ash [71][193].

Table 4.1: EDS analysis of as-quenched SC-0, SCM-5, SCM-10, and SCM-15 (wt%) with mean ± standard deviation (n = 8). Nominal compositions are given in parentheses below the measured values

Glass ID	Elements (wt%)				
	SiO_2	CaO	Na_2O	P_2O_5	MgO
SC-0	42.8 ± 1.50 (43)	23.9 ± 3.86 (25)	24.4 ± 2.00 (25)	7.2 ± 0.52 (7)	0.82 ± 0.10 (–)
SCM-5	43.4 ± 0.95 (43)	18.0 ± 1.80 (20)	25.2 ± 0.67 (25)	7.7 ± 0.21 (7)	5.1 ± 0.37 (5)
SCM-10	43.0 ± 1.03 (43)	11.8 ± 3.16 (15)	26.4 ± 1.69 (25)	7.5 ± 0.35 (7)	10.9 ± 1.62 (10)
SCM-15	43.0 ± 0.62 (43)	8.3 ± 1.51 (10)	25.8 ± 1.28 (25)	7.5 ± 0.28 (7)	14.1 ± 2.06 (15)

4.1.2 Physical parameters

The density (ρ) of as-quenched glasses was calculated using Archimedes' method. These data were then used to deduce the molar volume (V_m), oxygen packing density (OPD), and oxygen molar volume (V_o) as shown in **Fig. 4.2**.

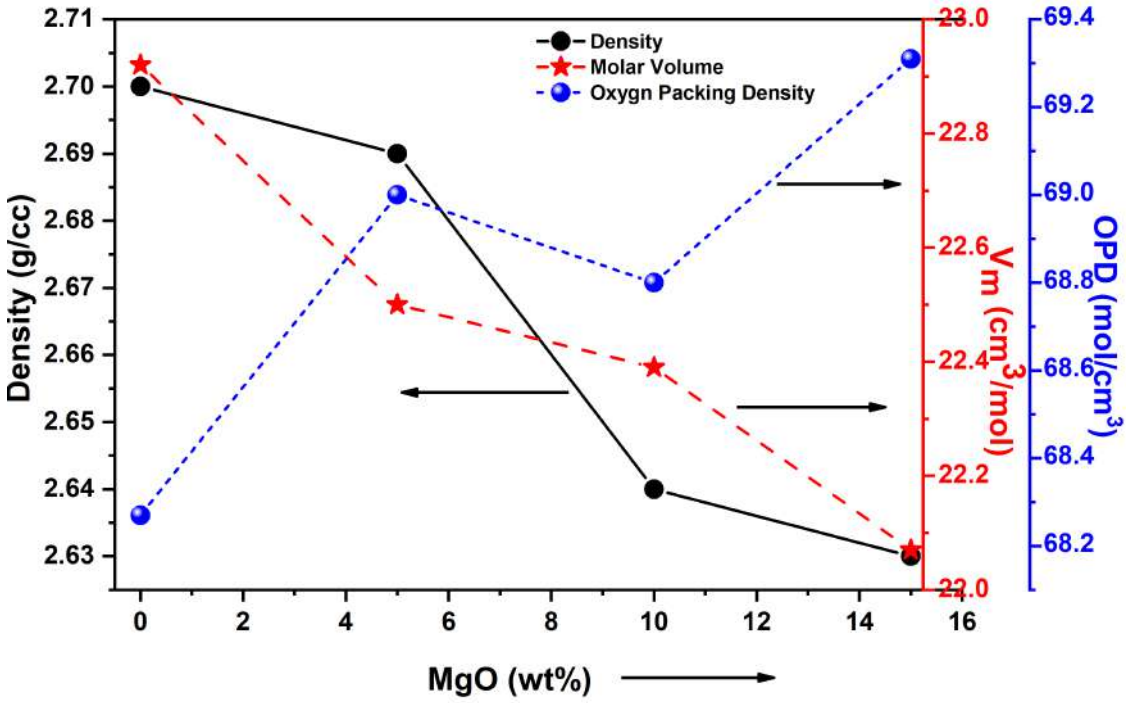

Figure 4.2: Represents the relation between density, molar volume, and oxygen packing with the increase in MgO (wt%) in the glass composition.

The density decreases with increasing MgO substitution for CaO. This observation is consistent with the lower molar mass of MgO (40.3 g/mol) com-

pared to CaO (56.1 g/mol). The molar volume (V_m), representing the volume occupied by one mole of glass, also decreases with increasing MgO concentration. While density and molar volume typically exhibit an inverse relationship, the observed decrease in both parameters in these glasses can be attributed to the higher field strength and smaller ionic radius of Mg^{2+} (0.72 Å) compared to Ca^{2+} (1.00 Å) [194][195]. The higher field strength of Mg^{2+} leads to a more compact glass network due to stronger coulombic interactions with oxygen anions, resulting in an overall volume contraction despite the lower mass of MgO [194][195]. In other words, the impact of the increased field strength outweighs the effect of the lower molar mass, resulting in a net decrease in molar volume. Furthermore, to shed light on this anomalous behavior, the oxygen packing density was calculated, revealing a trend opposite to that of the molar volume (V_m). The increased compactness induced by MgO can be further explained by its higher polarizing power compared to CaO. The smaller ionic radius of Mg^{2+} results in a higher charge-to-size ratio, leading to stronger polarization of non-bridging oxygen (NBO) atoms and a more compact glass structure [196]. This effect reinforces the observed trends in density and molar volume. The deviation from linearity observed in these parameters with increasing MgO content is attributable to the mixed modifier effect, which typically arises when the ratio of the two modifiers approaches unity, influenced by their respective field strengths and electronegativities [197][198][199].

4.1.3 XRD analysis

The X-ray diffraction (XRD) patterns of all the as-quenched glasses are shown in **Fig. 4.3**. The presence of a broad halo, instead of sharp peaks, confirms the amorphous nature of the present glasses, indicating the absence of long-range translational order. In addition to a wide halo at a maximum of around 32°, another halo is also present at $\sim 20°$. This secondary halo becomes more prominent with the addition of MgO in place of CaO. This secondary halo suggests the possibility of phase separation (matrix) within the glass matrix [196]. Several factors could contribute to this phenomenon. The higher field strength of Mg^{2+} compared to Ca^{2+} can promote immiscibility and phase separation in

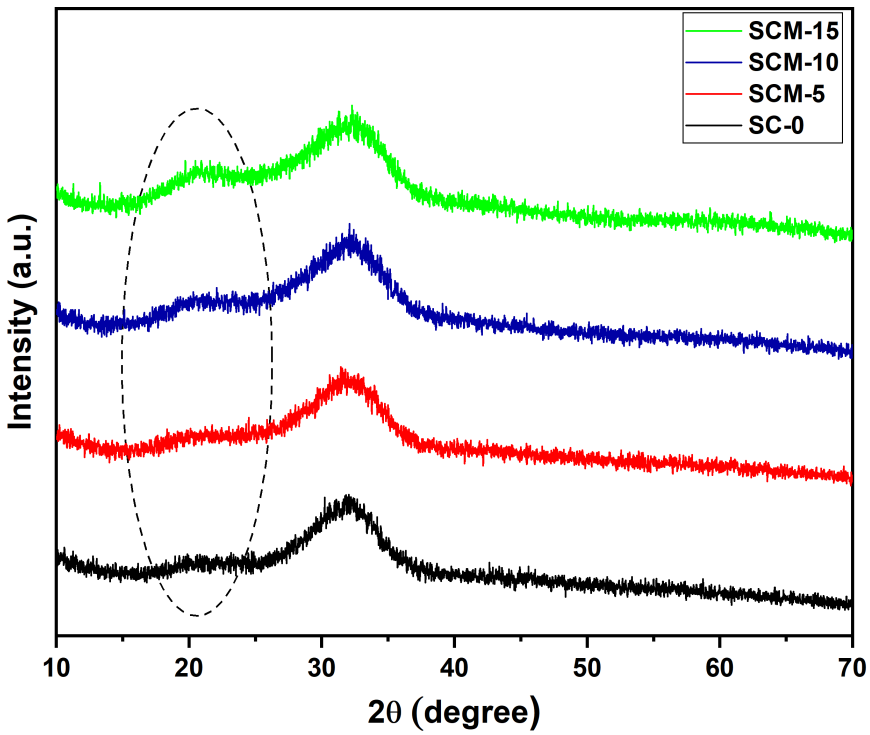

Figure 4.3: X-ray diffraction patterns of SC-0, SCM-5, SCM-10 and SCM-15 glasses

the glasses [196]. The formation of P-O-Mg bonds, due to the disruption of the orthophosphate environment of P_2O_5 by MgO (as discussed in Section 4.1.4), may also contribute to phase separation. Furthermore, the presence of two glass formers, P_2O_5 and SiO_2, is known to generally lead to phase separation in glasses due to their different chemical nature, bonding characteristics, and glass network formation behavior [200][201]. The increasing tendency of the secondary halo with increase in MgO content indicates the increased phase separation tendency of the glasses with MgO content. This observation is further supported by the presence of two glass transition temperatures (T_g) and two crystallization temperatures (T_c) determined from differential thermal analysis (DTA), as discussed in Section 4.1.4.

4.1.4 Differential thermal analysis (DTA)

DTA was performed to determine the glass transition temperature (T_g) and crystallization temperature (T_c) to assess thermal stability (**Fig. 4.4**). The thermographs reveal two T_g values: a subtle one between 300–400 °C (T_{g1}) and

a more prominent one between 400–550 $°C(T_{g2})$. The derivative of the DTA curve (**Fig. 4.5**) confirms the presence of these two endothermic T_g peaks in all glasses. Both T_g values decrease with increasing magnesium content. T_{g1} is likely associated with the phosphate network, which typically exhibits a T_g in the 300–400 °C range [202][203]. T_{g2} could be attributed to the majorly silicate glass network, usually observed between 450–600 °C [204][205].

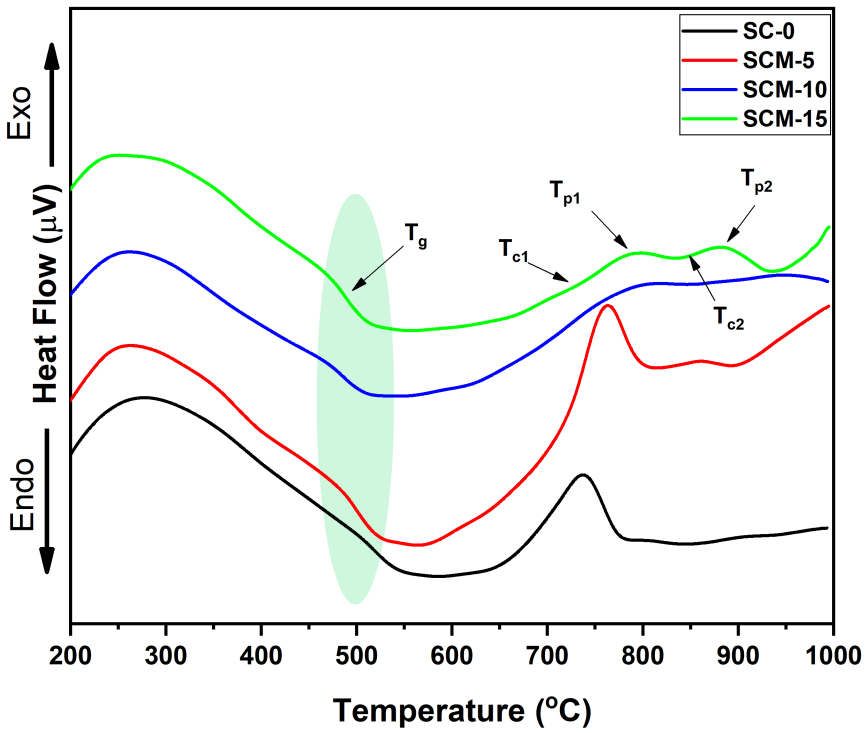

Figure 4.4: DTA thermographs of (a) SC-0, (b) SCM-5, (c) SCM-10, and (d) SCM-15 glass samples indicating T_g, and T_c

The decrease in T_{g1} may be due to the disorder created by MgO in the orthophosphate network, while the decrease in T_{g2} may be related to the dual nature of MgO. The formation of $(MgO_4)^{2-}$ tetrahedra could disrupt the silicate network, forming weaker Si-O-Mg bonds compared to Si-O-Si bonds [194]. This observation aligns with trends reported for other MgO-containing bioglasses [194][206]. While the higher field strength of Mg^{2+} compared to Ca^{2+} would typically suggest an increase in T_{g2}, the opposite trend is observed. This deviation may be associated with the presence of Na^+, leading to ion mixing

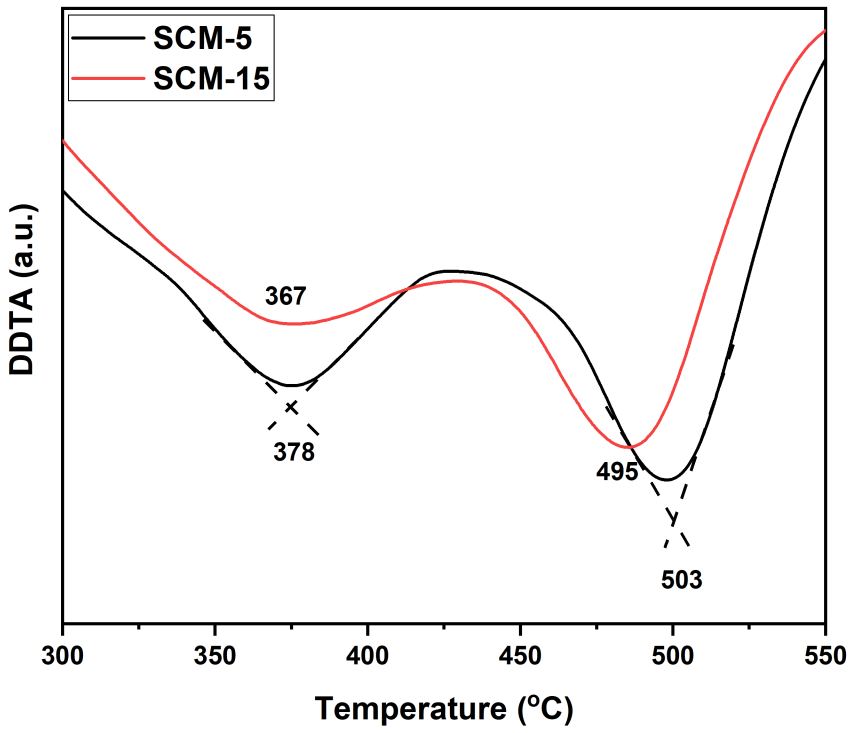

Figure 4.5: First order derivative of SCM-5 and SCM-15 glass indicating the presence of two T_g

or preferential bonding [157], as well as the increased phase separation. The presence of two T_c values, becoming more pronounced with increasing MgO substitution for CaO in the glass composition, further supports the increasing tendency for phase separation, most evident in the SCM-15 (15 wt% MgO) glass. However, T_{c2} shows a sluggish exotherm curve. The crystallization peaks also broaden with increasing MgO content. This phase separation aligns with the two halos observed in the XRD patterns (Section 4.1.3) and is consistent with previous studies on silicate glasses [196].

Table 4.2: Represents the thermal parameters of the glass,$\Delta T = T_{c1} - T_{g2}$ indicates the sintering window, T_s is the softening point, and TEC is the thermal expansion coefficient of glasses

Sample ID	T_{g1} (°C)	T_{g2} (°C)	T_{c1} (°C)	ΔT (°C)	TEC ($\times 10^{-6}$/°C)	T_s (°C)
SC-0	380	525	674	149	15.8	497
SCM-5	378	503	696	176	11.4	480
SCM-10	369	492	685	193	12.4	466
SCM-15	367	490	720	230	10.5	460

Despite the decreasing T_{g2} trend, the substitution of Ca^{2+} with Mg^{2+} leads to an increase in T_{c1} and a broadening of the crystallization peak, resulting in a wider sintering temperature window ($\Delta T = T_{c1} - T_{g2}$). This broadened window is advantageous for processing, as it allows for sintering without unwanted crystallization of the glasses. The enhanced stability and wider sintering window are attributed to the inhibitory effect of MgO on crystallization.

4.1.5 Thermal expansion coefficient (TEC)

TEC is related to the asymmetry of the interatomic potential well. As shown in **Table 4.2**, the TEC decreased with increasing MgO content, which can be attributed to the smaller ionic radius and higher field strength of Mg^{2+} compared to Ca^{2+} [157]. **Fig. 4.6** presents the dilatometric curves for the as-quenched glasses. A slight increase in TEC is observed for SCM-10, with a slight decrease in softening temperature (T_s) as compared to SCM-15 glass. This anomaly could be due to a mixed modifier effect as the MgO/CaO ratio approaches unity, resulting in increased competition between the two modifier oxides, which can lead to deviations in expected property trends [194].

The results observed for decreasing T_s are also consistent with DTA results with increasing MgO (**Table 4.2**), consistent with the DTA results. The approximately 30 °C difference between T_g and T_s is due to the different heating rates (i.e., 5 °C for TEC and 15 °C for DTA) employed in the two different techniques [207]. The measured TEC values are within the range suitable for bioactive glasses, dentin, enamel coatings, and orthopedic substrates [143]. Importantly, the TEC of bioactive glasses can be adjusted through compositional modifications, allowing it to be tailored for specific applications like dental and orthopedic coatings while maintaining bioactivity [143][146]. The TEC of SCM-15 is close to that of dentin and enamel ($8 \times 10^{-6} – 10 \times 10^{-6}/°C$) [208], suggesting its potential suitability for such applications.

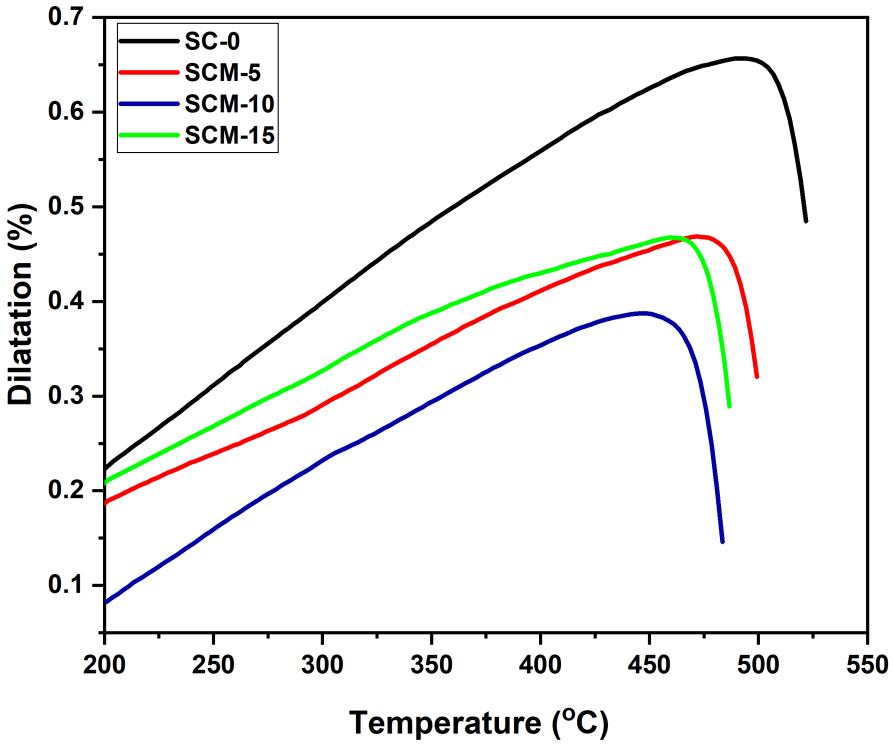

Figure 4.6: Dilatometric curves of the as-quenched glasses

4.1.6 FTIR analysis

FTIR spectra of all the glasses show more or less similar spectra, with minor band splitting and shifting of the bands is observed with increasing MgO substitution (as shown in **Fig. 4.7**, FTIR spectra in the range from 4000-400 cm^{-1} is shown in Appendix **Fig. A1(a)**). To better understand the structural roles of SiO_2 and P_2O_5, FTIR spectra of all the glasses were deconvoluted **(Fig. 4.8)**. Deconvolution reveals bands from 500 to 1200 cm^{-1}, representing various structural units of both the glass networks.

In the silicate network, the Q^n notation (where n represents the number of bridging oxygens per silicon tetrahedron) is used to describe the structural units. The band at 840–846 cm^{-1} is attributed to Si-O stretching vibrations in Q^0 units. The band at ∼906–907 cm^{-1}, assigned to Q^1 units, remains relatively unchanged with MgO content, suggesting that Q^2 units dominate the present glass structure. The increase in peak area and full width at half max-

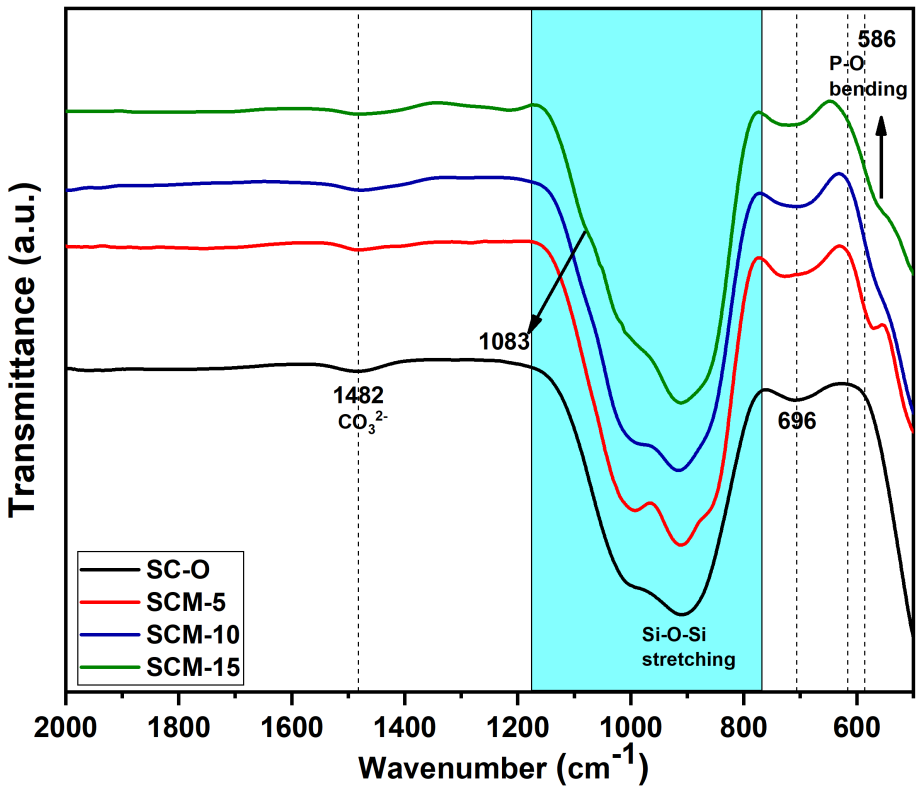

Figure 4.7: FTIR spectra of as-quenched SC-0, SCM-5, SCM-10, and SCM-15 glasses in 2000-500 cm^{-1} range

imum (FWHM) of the bands at ∼1084–1098 cm^{-1} (Q^3 units) with increasing MgO substitution indicates an increase in the proportion of Q^3 structural units (as shown in the **Table 4.3**). This shift in Q^n distribution is reflected in the increasing ratios of $\frac{Q^3}{Q^2}$, $\frac{Q^3+Q^2}{Q^1}$, and $\frac{Q^3}{Q^2+Q^1}$ with increasing magnesium substitution. However, the ratio $\frac{Q^2}{Q^1}$ deviates from the linear trend, initially decreasing for SCM-5, then increasing for SCM-10, and finally slightly decreasing for SCM-15. Overall, these changes in structural units reveal increasing polymerization of the glass network. The band at 732 cm^{-1} is assigned to Si-O-Si stretching vibrations [209][210].

Regarding the phosphate network, the band at 1034–1065 cm^{-1} represents vibrations of PO_4^{3-} tetrahedra with four NBO atoms. The shoulder band at ∼586 cm^{-1} shifts to slightly lower wavenumbers with increasing MgO substitution, indicating asymmetric bending vibrations of the P-O bond and increased

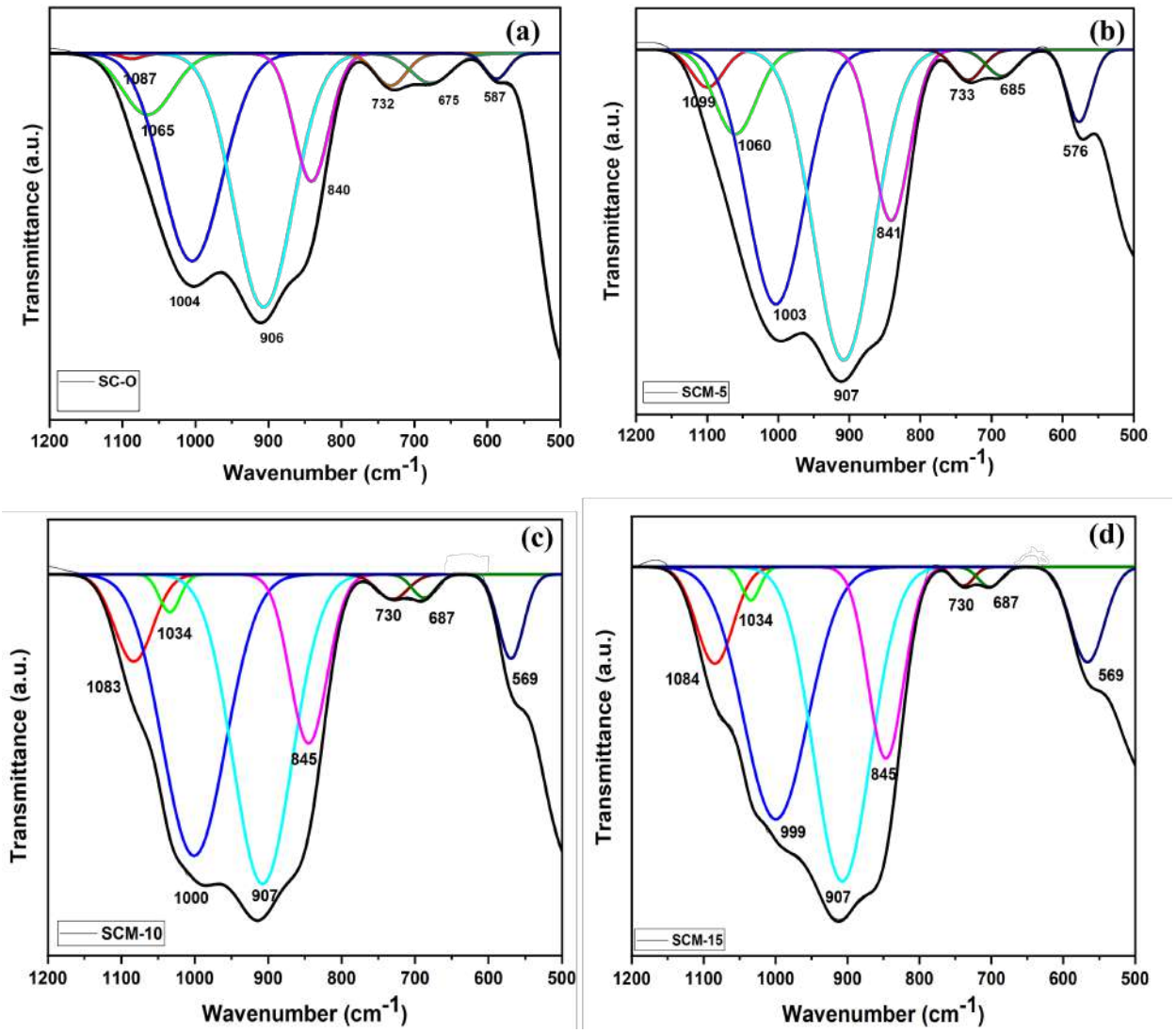

Figure 4.8: Deconvolution spectra using Gaussian curves for peak fitting of (a) SC-0 (b) SCM-5 (c) SCM-10 and (d) SCM-15 samples from 500–1200 cm^{-1}

Table 4.3: Quantitative data for Q^n (n = number of structural units) structural units derived using peak area and their ratios

Sample ID	Q^1	Q^2	Q^3	$\frac{Q^3}{Q^2}$	$\frac{Q^2}{Q^1}$	$\frac{Q^3+Q^2}{Q^1}$	$\frac{Q^3}{Q^2+Q^1}$
SC-0	74.29	62.52	0.88	0.0141	0.8416	0.8490	0.0040
SCM-5	96.08	75.91	6.183	0.0814	0.7901	0.8544	0.0360
SCM-10	85.65	83.34	15.70	0.1884	0.9730	1.1563	0.0929
SCM-15	84.62	77.00	16.81	0.2184	0.9218	1.1216	0.1040

disorder in the orthophosphate environment[209][211]. This increased disorder is potentially due to the formation of P-O-Mg bonds, facilitated by the higher electronegativity of Mg^{2+} (1.31) compared to Ca^{2+} (1.00) and Na^+ (0.93) [210]. The presence of orthophosphate units may also contribute to the observed phase

separation in the glasses [194][196].

Magnesium, with its higher field strength based on Dietzel's criteria, exhibits a dual nature, acting as both a network modifier and a former depending on its concentration in glass composition [194]. Watts *et al.* [194] reported that, in similar glass compositions (49.46 SiO_2 - 26.38 Na_2O - (23.8-x) CaO - 1.07 P_2O_5 - xMgO, where x ranges from 0 to 23.08 mol%), approximately 86% of the magnesium acts as a network modifier, while the remaining ∼14% acts as a network former. This dual behavior is reflected in the observed shifts in the SiO_2 and P_2O_5 bands: MgO addition causes the slight shift of SiO_2-related bands to higher wavenumbers (indicative of a network-forming role), while the P_2O_5-related bands shift to lower wavenumbers (indicative of a network-modifying role). This dual role of MgO further contributes to the increased phase-separation tendency. In essence, MgO promotes the formation of orthophosphate groups, which enhances phase separation in the glasses while simultaneously increasing the polymerization of the silicate network.

Further, a carbonate band is observed at ∼1482 cm^{-1} in all glass samples, which can be attributed to carbonate impurities present in the eggshell powder [212][213][214]. This band becomes more prominent upon the formation of carbonated hydroxyapatite (c-HAp), as discussed further in Section 4.1.11.

4.1.7 Hardness of glasses

Hardness, a complex property influenced by bond strength, porosity, degree of polymerization, and fictive temperature. For oxide glasses, hardness is typically reported to be within the range of ∼2–8 GPa [215]. In the present study, Vickers hardness values ranged from 4.6 to 6.2 GPa (**Fig.4.9**).

Although MgO substitution for CaO is generally expected to increase hardness due to the higher field strength of Mg^{2+} (0.45 $Å^{-2}$) compared to Ca^{2+} (0.33 $Å^{-2}$), resulting in stronger bonds, a clear monotonic trend was not observed. Hardness initially increased from SC-0 (0 wt% MgO) to SCM-5 (5 wt% MgO), then decreased for SCM-10 (10 wt% MgO), and finally increased again for SCM-15 (15 wt% MgO). This non-linear behavior may be attributed to

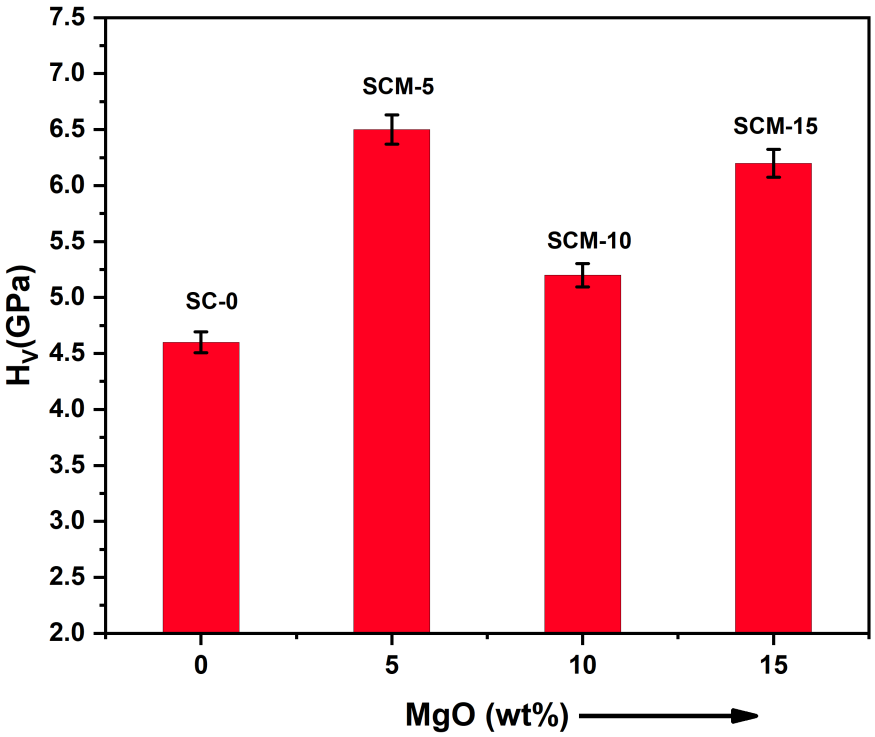

Figure 4.9: Hardness of the glass samples before and after heat treatment

the mixed modifier effect, which is expected to be most prominent in SCM-10. SCM-5 exhibited the highest hardness among the series, potentially indicating increased network connectivity, which might be related to its lower bioactivity compared to other samples as discussed in the following sections. Initially, MgO may act as a network former, integrating into the SiO_2 network. However, with increasing MgO content, it may preferentially modify phosphate units, disrupting the glass network and leading to the observed non-linearity. The measured hardness values align with the reported hardness of 45S5 glass (4.58 ± 0.094 GPa) and other heat-treated bioglass/bioceramic systems [216][217].

4.1.8 In-vitro testing of glasses

4.1.8.1 Biodegradability and pH change in SBF

The bioactive properties and degradation behavior of the glasses were evaluated by immersing them in SBF for various durations at constant temperature. **Fig.4.10** shows the pH variation (**Fig. 4.10(a)**) and weight change (**Fig.**

4.10(b)) of the glasses over time. SC-0 exhibited the highest weight loss, while SCM-15 showed the least.

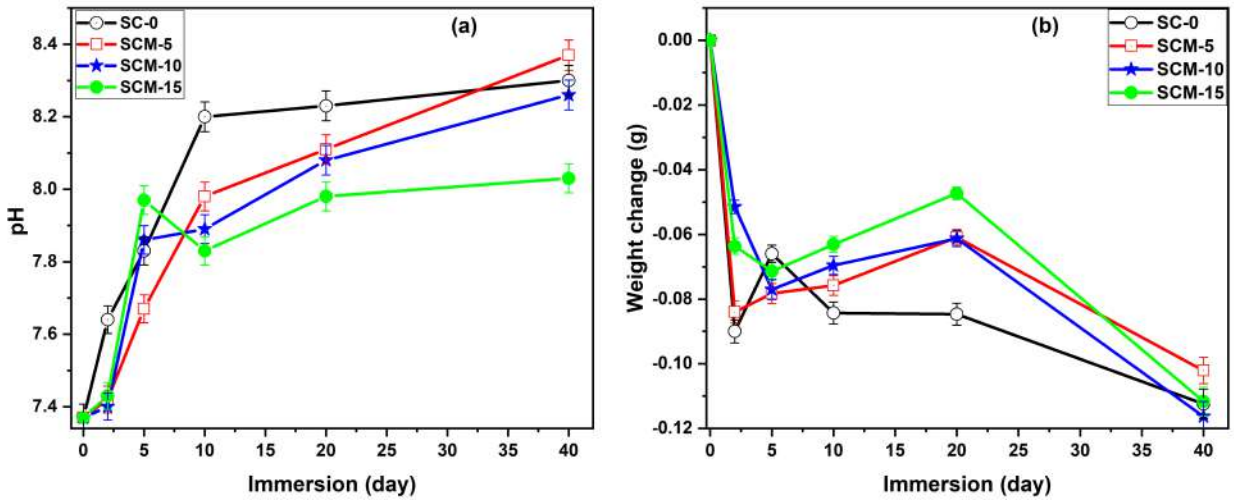

Figure 4.10: In-vitro degradation and pH variation SC-0, SCM-5, SCM-10, and SCM-15 glasses after immersion in SBF: (a) pH variation; (b) Weight change. Error bars indicate standard deviation.

SC-0 and SCM-5 showed the most rapid weight loss within the first two days of immersion. SC-0 then showed a weight gain after 5 days, followed by weight loss at 10 days, finally stabilizing at 20 days. SCM-5, after its initial weight loss, exhibited continuous weight gain up to 20 days. Glasses with higher MgO concentrations (SCM-10 and SCM-15) showed slower dissolution during the first two days, with maximum weight loss observed at 5 days, followed by continuous weight gain up to 20 days. The increasing MgO content correlates with slower degradation. This is likely because SC-0 contains only CaO (which is more hydrophilic than MgO), while the other glasses contain a mixture of CaO and MgO in different ratios [218]. The distinct behavior of SC-0 can be attributed to the presence of only one alkaline earth metal oxide (CaO) in its composition. Moreover, CaO is more hydrophilic in nature in comparison to MgO .

Interestingly, SCM-15 showed minimal weight change. This might be attributed to the mixed-modifier effect of the MgO/CaO combination, where a ratio approaching unity hinders dissolution due to the competitive interaction of the two modifier ions [212]. Similar weight change trends have been reported for other bioactive glasses derived from agro-food waste and mesoporous bioac-

tive glass [71][219].

Further, the pH variation provides insights into the dissolution process. The pH change is directly related to the physicochemical reactions and ion exchange between the glass and the SBF. All glasses exhibited degradation, and the pH variation was non-uniform over time. The initial pH rise is attributed to the release of base ions (Ca^{2+}, Na^{+}, and Mg^{2+}) and their interaction with H^{+} and H_3O^{+} ions, followed by the release of acidic Si^{4+} ions at later stages of immersion [6][219]. This process eventually reaches equilibrium, resulting in a stabilized pH. The release of base ions can be represented as follow:

$$\text{Si-O-Ca}^{2+} + \text{H}^{+} \rightarrow \text{Si-OH}^{-} + \text{Ca}^{2+} \tag{4.1}$$

This pH increase leads to the formation of silicic acid ($Si(OH)_4$) near the glass surface, which in turn stabilizes the pH and facilitates attack on the silica network by SBF. MgO-substituted glasses showed a non-uniform pH trend at 5 days. However, after 10 days, glasses with higher magnesium content (SCM-10 and SCM-15) exhibited smaller pH changes than SC-0 and SCM-5, potentially due to slower Si^{4+} release. This observation is supported by MP-AES results (section 4.1.8.3), indicating lower silicate concentrations in SBF for SCM-10 and SCM-15. These results suggest that magnesium substitution increases chemical durability and hinders Si^{4+} release, consistent with the weight change results.

A further pH increase suggests reabsorption of Ca^{2+} and PO_4^{3-} ions from the SBF to form hydroxyapatite (HAp) on the glass surface. This pH increase slows as the solution becomes saturated, and the ion exchange rate decreases. Calcium phosphate (Ca-P) ions from the glass and SBF form a Ca-P-rich layer, which gradually incorporates carbonate ions (CO_3^{2-}) from the SBF, forming carbonated HAp (c-HAp) [219]. Slower dissolution and pH variation lead to more stable HAp formation. The c-HAp formation is driven by ion exchange and influences the dissolution rate, which can be optimized by adjusting modifier type and concentration. Using a single modifier like CaO promotes faster HAp growth, while incorporating two modifiers (e.g., CaO and MgO) moder-

ates the dissolution rate, beneficial for applications requiring slow degradation [2][220]. The pH variation was recorded up to 40 days, at which point dissolution was observed for all glasses.

4.1.8.2 MP-AES analysis

MP-AES was employed to quantify ion concentrations in SBF after immersing the glasses for 20 days. **Table 4.4** shows the concentrations of Si^{4+}, Ca^{2+}, Mg^{2+}, and Na^+ in SBF, along with changes in Ca and P content (wt%) in the glasses before and after immersion, as determined by EDS analysis. The Ca/P molar ratio calculated from EDS data is also included.

Table 4.4: Ion concentrations (mg/L, n=3) in SBF after 20 days immersion measured by MP-AES and elemental composition (wt%, n=8) of glasses before and after immersion measured by EDS

Sample	MP-AES (mg/L)				EDS (wt%)				
Name	Si	Ca	Mg	Na	Unsoaked		Soaked		Ca/P
					Ca	P	Ca	P	ratio
SBF	<0.10	16.4	37.4	3508	–	–	–	–	–
SC-0	65.3	135	30.3	3223	17.1	3.2	18.3	3.4	4.1
SCM-5	51.4	110	55.3	3145	12.9	3.3	19.4	4.5	3.3
SCM-10	56.4	88.9	77.4	3125	8.5	3.2	16.8	4.6	2.8
SCM-15	55.9	66.9	107	3272	5.9	3.3	12.4	5.8	1.6

SC-0 exhibited the highest ion release, possibly due to a less polymerized glass network. The release of alkali ions and their exchange with H^+ ions are crucial for bone bonding and regeneration [8][221]. The uneven release of sodium is recorded for all the glasses. However, increasing amounts of magnesium retards the liberation of sodium. This may be attributed to the dual role of MgO and the incorporation of Na^+ ions into $(MgO_4)^{2-}$ tetrahedral for charge balancing [194].

The release of silica was highest for SC-0, with increasing magnesium having minimal impact on Si^{4+} release. This ion must be released from the interconnected glass network in the form of the Si-OH^- group. Silicon ion release from the glass network may occur later in the apatite formation process, as the glass

network weakens after immersion in SBF, and the increase in magnesium in the glass sample replacing CaO results in a decrease in the amount of leached Ca^{2+} ion in the solution. Interestingly, the decrease in Ca^{2+} ions in the solution indicates increased Ca^{2+} in the glasses, as shown in the EDS result of the immersed samples (discussed in the section below 4.1.9), which suggests the deposition of Ca^{2+} from the solution to the glasses. This trend is in accordance with the saturation of the pH value and the increase in the weight of the samples, as explained in the section above.

4.1.9 FE-SEM with EDS analysis

The FE-SEM micrographs (**Fig. 4.11**) show an appreciable surface modification of the glasses after the immersion of glass samples with increasing time in SBF solution. A heterogeneous hydroxyapatite (HAp) layer develops on all glasses after 20 days of immersion in SBF (as shown in **Fig. 4.11**). SC-0 and SCM-15 show progressive HAp layer growth, while SCM-5 exhibits slower development even after 20 days, this may be due to the higher network connectivity in the SCM-5 glass as discussed earlier. FE-SEM images show a heterogeneous, spongy layer that forms on the SC-0 surface, along with small flakes. For SCM-5 and SCM-15, small, heterogeneously distributed clusters of white aggregates are observed. SCM-15 shows a more pronounced formation of the HAp layer compared to SCM-5 and SCM-10. EDS analysis of these white aggregates is presented in **Table 4.4**.

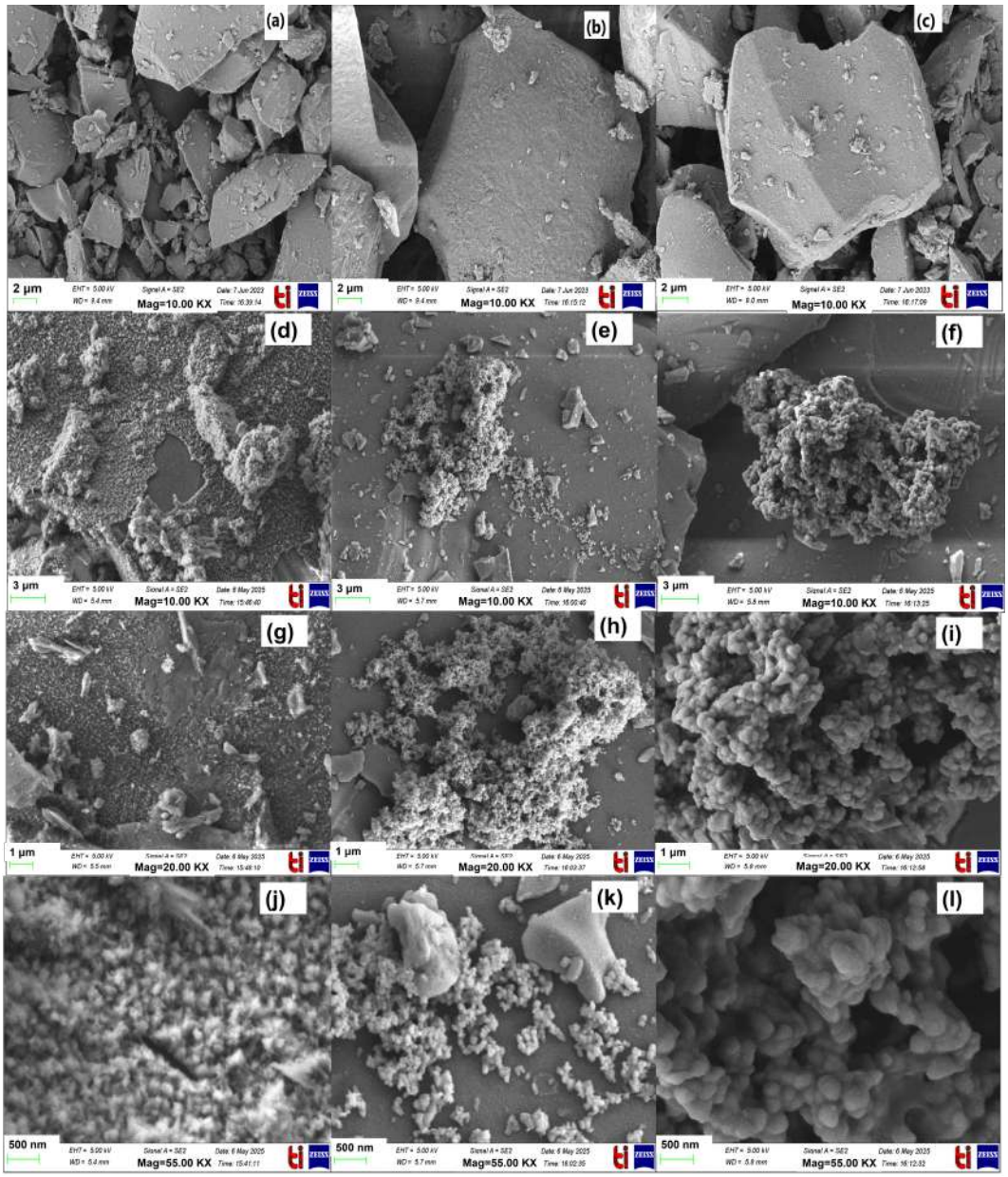

Figure 4.11: FE-SEM images of glass surfaces before and after immersion in SBF. Before immersion: (a) SC-0, (b) SCM-5, (c) SCM-15. After immersion: SC-0, SCM-5 and SCM-15 (d,e,f) after 20 days at 10X, (g,h, i) after 20 days at 20X, (j,k,l) after 20 days at 55X

The Ca/P molar ratio for SC-0, SCM-5, and SCM-10 (ranging from 2.8 to 4.1) was higher than the standard stoichiometric ratio for hydroxyapatite (HAp) (1.67). However, the Ca/P ratio for SCM-15 (1.63) was close to the standard stoichiometric value, suggesting enhanced bioactivity for this composition. While a Ca/P ratio of 1.67 is often considered ideal for HAp, values between 2.8 and 4.1 have also been reported for carbonated HAp (c-HAp) in bioactive glasses [61][222][223]. This higher Ca/P ratio can be attributed to

heterogeneity in the c-HAp layer caused by trace elements present in the starting materials, particularly when agro-food wastes were used as the sustainable resources to synthesize the glasses [71]

The distribution of various elements in SCM-15 without immersion and after immersion for 20 days is confirmed using area mapping, as shown in **(Fig. 4.12)**, which confirms the elemental distribution. It is evident from these figures that a HAp rich layer is formed on the immersed SCM-15 glass.

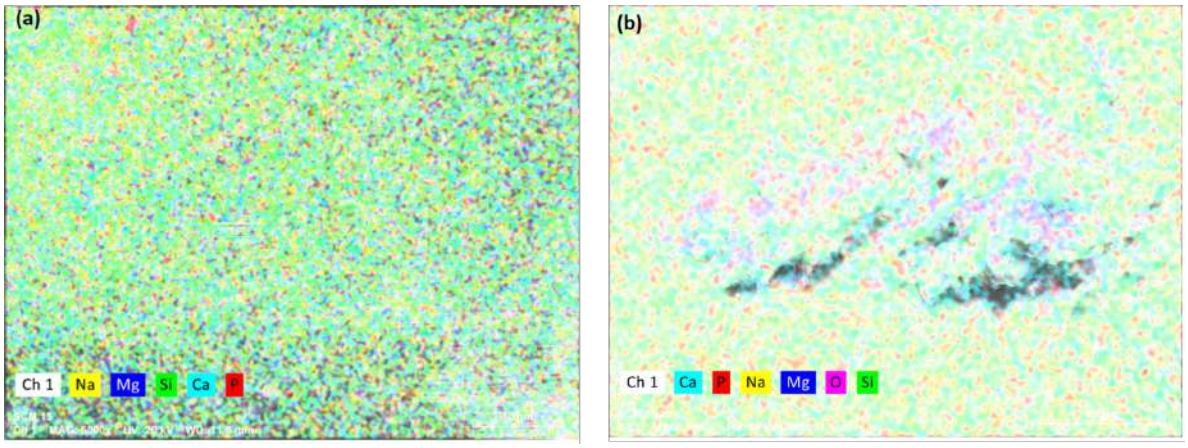

Figure 4.12: EDS area mapping of SCM-15 glass: (a) before immersion and (b) after immersion for 20 days

4.1.10 XRD analysis after immersion

XRD patterns of the glass samples before and after immersion in SBF are shown in **Fig. 4.13**. Minimal changes are observed in immersed glasses as compared to the pristine glasses. After immersion, weak diffraction peaks corresponding to semi-carbonated hydroxyapatite (HAp) (ICDD card no. 01-072-1243) appear in all immersed samples. In SC-0, a few feeble peaks indexed with tetracalcium phosphate (TTCP) (ICDD card no. 01-070-1379) are also present. The main constituents of tetra calcium phosphate are calcium (Ca) and phosphorus (P), the primary elements found in the structure of the bone matrix. The phase primarily occurs as an intermediate between the HAp layer's formation with the Ca/P ratio >2, and can be beneficial for cell adhesion and bone regeneration [224][225].

In the magnesium-substituted glasses, HAp formation is not detected by XRD within the first 5 days of immersion. This suggests that Mg^{2+} initially

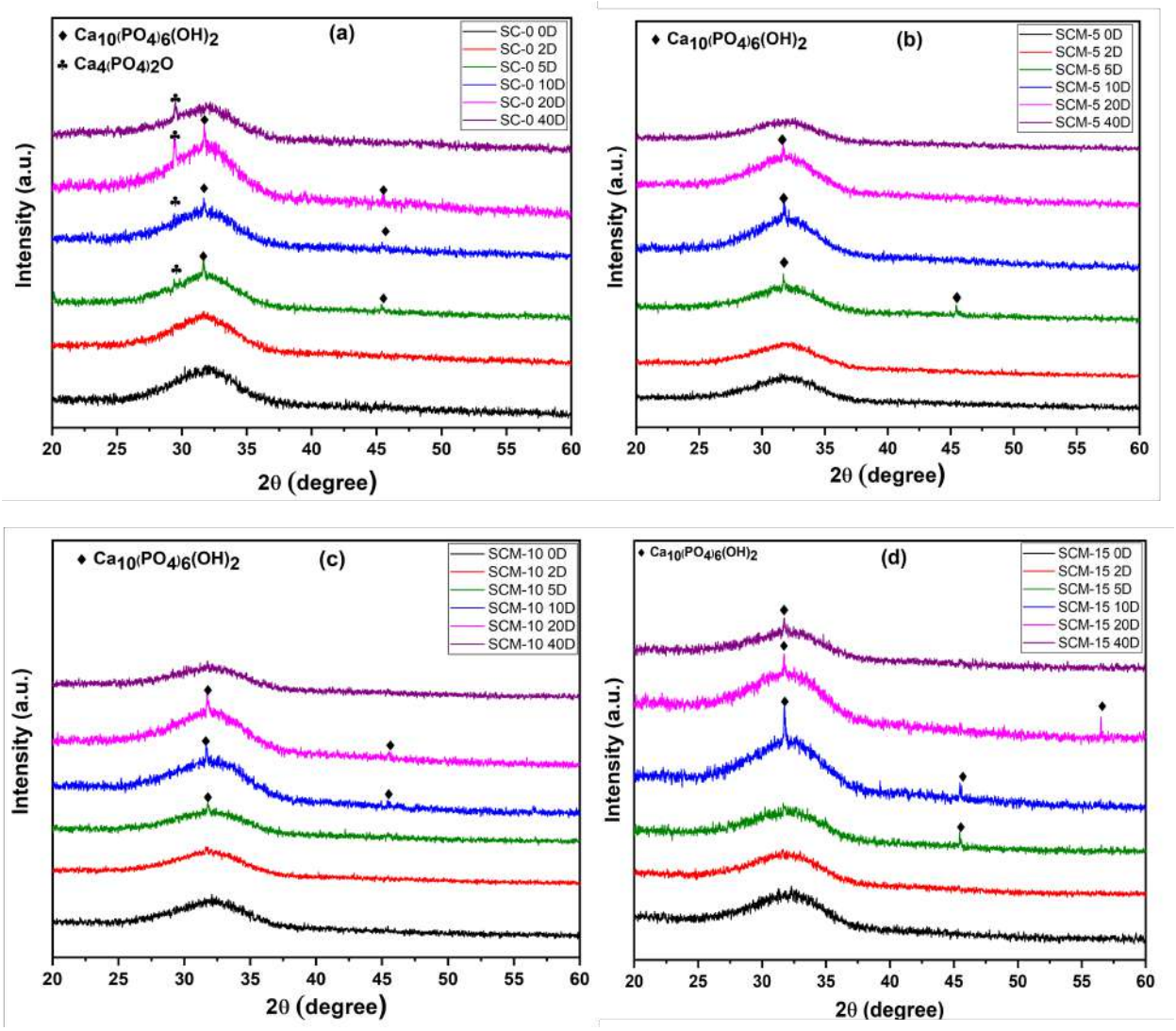

Figure 4.13: XRD patterns of glass samples (a)SC-0 (b) SCM-5 (c) SCM-10 (d) SCM-15 before and after SBF immersion

retards HAp formation but may ultimately enhance its stability. The slower degradation of these glasses indicates increased glass network interconnectivity due to magnesium. However, prolonged immersion leads to the breakage of bonds formed by magnesium, followed by the formation of a silanol layer and subsequent development of the HAp layer. As the XRD pattern of all the glasses shows no formation of the HAp layer, the data for 2 days is omitted for further studies.

4.1.11 FTIR analysis of immersed glasses

FTIR spectra of the glass samples after immersion in SBF for various durations are shown in **Fig. 4.14** (FTIR spectra from 4000-400 cm^{-1} is given in appendix as **Fig. A2**). Deconvoluted was done to **(Fig. 4.15)** analyze the changes in the bands compared to the pristine glasses. While the deconvoluted spectra reveal variations in the trends among the different glass compositions, the most significant changes are observed after 20 days of immersion, except for SCM-15. The band at ∼910 cm^{-1} gradually merges with a sharper band at ∼1015 cm^{-1} (attributed to phosphate units), with the latter's intensity increasing with immersion time. The band at 1632 cm^{-1} was observed in all the glasses with increase in immersion time, which is attributed to the presence of H_2O in the HAp layer [71]. The band corresponding to the $CO_3{}^{2-}$ at 1482 cm^{-1} intensifies with the increase in the immersion time, indicating the formation of the c-HAp layer [226].

In the fingerprint region, SCM-10 and SCM-15 exhibit similar behavior. Deconvolution reveals increased intensity and a shift towards higher frequencies compared to the pristine glasses, consistent with the expected changes upon SBF immersion. These changes highlight the interplay between silanol and phosphorus units in forming the HAp layer. Specifically, the shoulder band at 580 cm^{-1} increases in intensity, and the appearance of phosphate and carbonate bands, along with band splitting, further confirms the formation of c-HAp [222][223].

After immersion, the phosphate and carbonate bands observed on the glass surface resemble those of synthetic c-HAp and HAp formed on mineral-based bioactive glasses [227]. It is contradictory that magnesium with 15% substitution forms a better c-HAp layer than SCM-5 and SCM-10 glasses; this might be due to the relatively weaker bond strength of Mg-O-Si bonds compared to Si-O-Si bonds, which could facilitate glass degradation with increasing immersion time [194]. These results are in trend with magnesium at 5 wt% and afterward, opposite in the trend compared to the earlier reports in the literature for higher magnesium substitution [223][228]. This contrasting behavior may be related

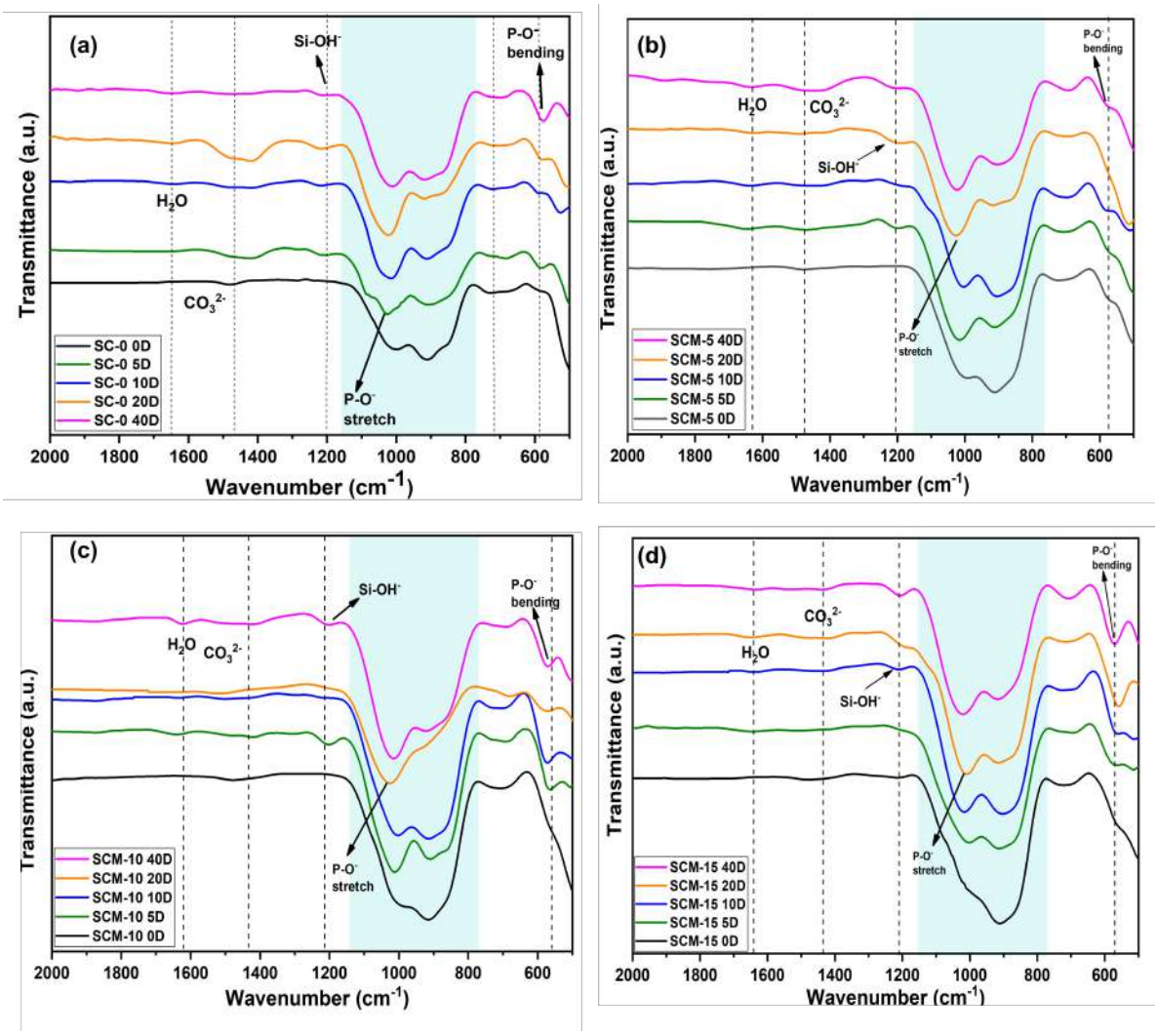

Figure 4.14: FTIR spectra (2000-500 cm^{-1}) of (a) SC-0, (b) SCM-5, (c) SCM-10, and (d) SCM-15 after immersion in SBF for different time period (compared with pristine glasses)

to the association of higher MgO content with the phosphate glass network, as discussed in Section 4.1.6. However, it is well documented in the literature that magnesium enhances the bioactive properties by promoting cell proliferation and osteointegration [43].

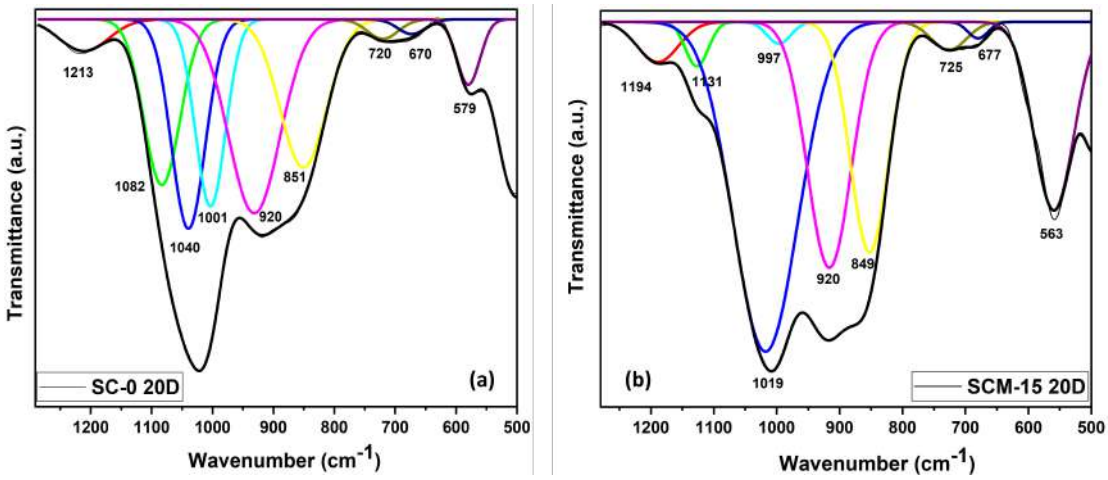

Figure 4.15: Representative deconvoluted FTIR spectra of (a) SC-0 (20 days) and (b) SCM-15 (20 days) (400–1300 cm^{-1})

4.1.12 MTT assay

The MTT assay was performed to evaluate the effect of the glasses on the viability of peripheral blood mononuclear cells (PBMCs) at concentrations up to 200 μg/ml **(Fig. 4.16)(a)**. Cell viability was also monitored over 48 hours using a constant concentration of 100 μg/ml **(Fig. 4.16)(b)**. The results indicate that cell viability remained above 85% for all glasses up to 200 μg/ml and after 48 h of treatment with 100 μg/ml.

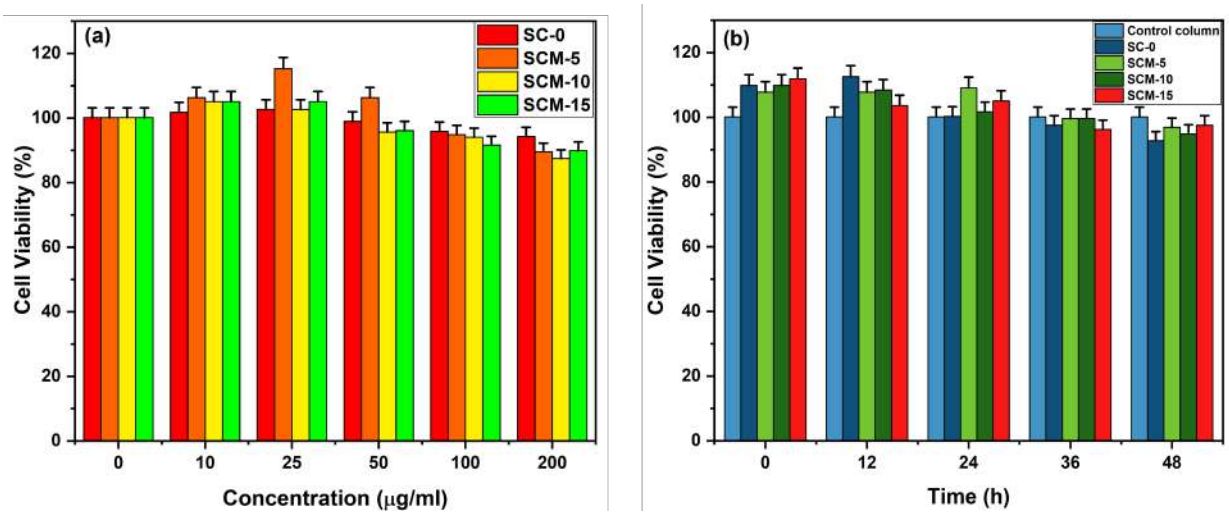

Figure 4.16: Cell growth effect of (a) Different concentrations of glasses on human PBMC cells (b) At different time intervals with constant concentration (100 μg/ml) of glasses. The bar represents that the treatments on PBMC cells are not significantly different at p- value >0.05

According to ISO 10993-5, a substance is considered cytotoxic if it reduces

cell viability by more than 30% [61][229]. None of the tested glasses exhibited cytotoxicity to PBMCs, even at the highest concentration (200 μg/ml) or after 48 h of exposure (100 μg/ml). This finding was confirmed by a one-way ANOVA test ($p < 0.05$). Notably, glasses like SC-0 and SCM-10, which showed poorer HAp layer formation in previous studies, did not exhibit any cytotoxic effects. Interestingly, SCM-5 resulted in the highest cell proliferation among the glasses. The cytocompatibility of MgO-doped bioactive glass, showing no toxic effects at 100 μg/ml on normal human fibroblast cells, has been previously reported [230]. The glasses tested in the present study demonstrate excellent cytocompatibility with PBMCs.

4.2 43SiO_2-25CaO-7P_2O_5(25-y)Na_2O-(y)K_2O (y = 0, 5, 10, and 15 wt%)

Similar to the MgO-substituted series, these glasses were synthesized via the melt-quench technique. This series systematically replaces Na_2O with K_2O. The as-prepared glasses and those immersed in SBF were characterized using various techniques, with the results and discussion presented in the following subsections.

4.2.1 Compositional analysis

EDS was employed to analyze the composition of the melt-quenched glasses. The measured compositions of the pristine glasses closely matched with the nominal compositions, with trace amounts of additional elements also detected. As with the MgO-substituted series, SC-0 serves as the base glass. Similar to the previous series, trace amounts of MgO and Al_2O_3 (below 1 wt%) were detected.

Table 4.5: EDS analysis of as-quenched SC-0, SNK-5, SNK-10, and SNK-15 (wt%) with mean ± standard deviation (n = 8). Nominal compositions are given in parentheses below the measured values.

Glass ID	**Elements (wt%)**					
	SiO_2	**CaO**	**Na_2O**	**P_2O_5**	**K_2O**	**MgO**
SC-0	42.8 ± 1.50 (43)	23.9 ± 3.86 (25)	24.4 ± 2.00 (25)	7.2 ± 0.52 (7)	– (–)	0.82 ± 0.10 (–)
SNK-5	44.0 ± 1.25 (43)	22.0 ± 3.02 (25)	21.06 ± 2.00 (25)	7.7 ± 0.31 (7)	4.47 ± 0.45 (5)	0.68 ± 0.17 (–)
SNK-10	42.0 ± 3.52 (43)	24.36 ± 4.72 (25)	15.4 ± 2.42 (15)	7.1 ± 1.10 (7)	9.95 ± 2.02 (10)	0.67 ± 0.33 (–)
SNK-15	42.0 ± 0.66 (43)	25.01 ± 6.02 (25)	10.40 ± 3.05 (10)	5.7 ± 0.45 (7)	14.67 ± 2.50 (15)	0.78 ± 0.22 (–)

4.2.2 Physical parameters

The density (ρ) of the glasses was measured using Archimedes' method as discussed earlier and given in Section 3.3.1. As shown in **Fig. 4.17**, increasing K_2O substitution for Na_2O results in a decrease in density (from 2.70 g/cm^3 to 2.61 g/cm^3) and a corresponding increase in molar volume. This inverse relationship between density and molar volume is expected. The observed trend is attributed to the substitution of the smaller Na^+ (1.02 Å) with the larger K^+ (1.34 Å), indicating that ionic size has a more significant effect than the atomic mass of Na_2O and K_2O. The larger K^+ ions disrupt the glass network, creating a more open structure and increasing the molar volume. This is consistent with the decreasing oxygen packing density and increasing oxygen molar volume observed with increasing K_2O [165][195][231]. The lower field strength of K^+ (0.52 Å^{-2}) compared to Na^+ (0.96Å^{-2}) [232] further contributes to the more open, less compact glass structure. This increased openness might lead to higher dissolution rates in SBF, as discussed in section 4.2.8.

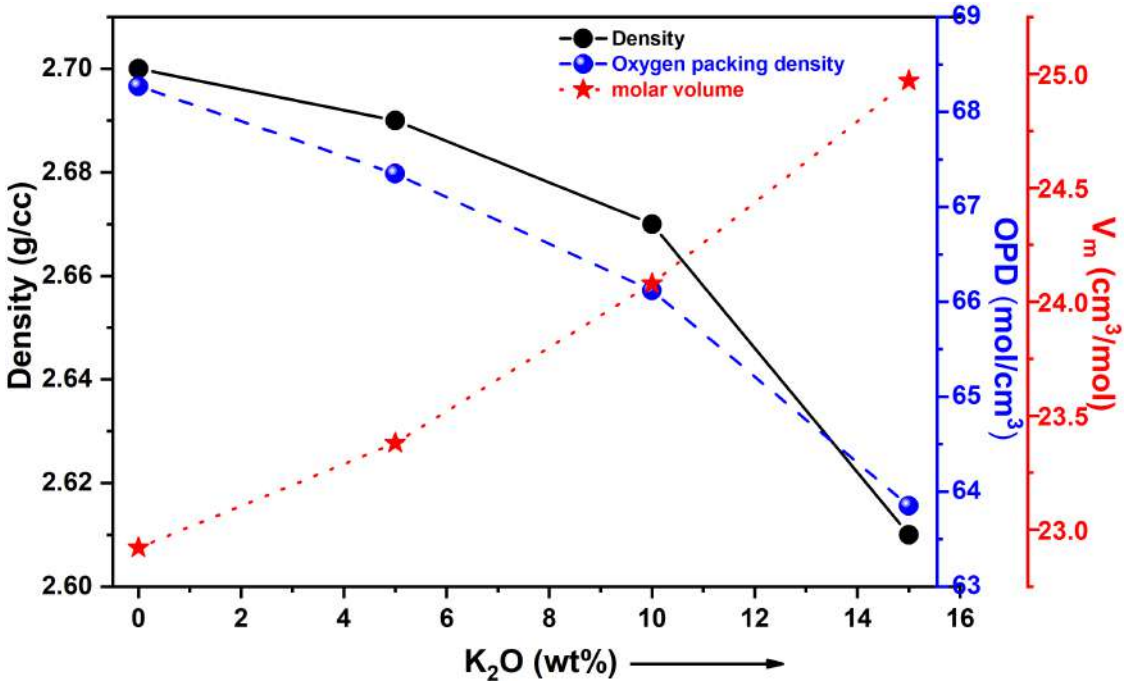

Figure 4.17: Relationship between density, molar volume, and oxygen packing density with the increase in the K_2O (wt%) in the glass composition

4.2.3 XRD analysis

XRD patterns of the glasses are presented in **Fig. 4.18**. A broad hump between 25° and 37°, indicates the amorphous structure of the present glasses. This characteristic hump arises from the presence of short-range order and the absence of long-range order. A secondary halo is also present at ∼20° in SC-0 glass only.

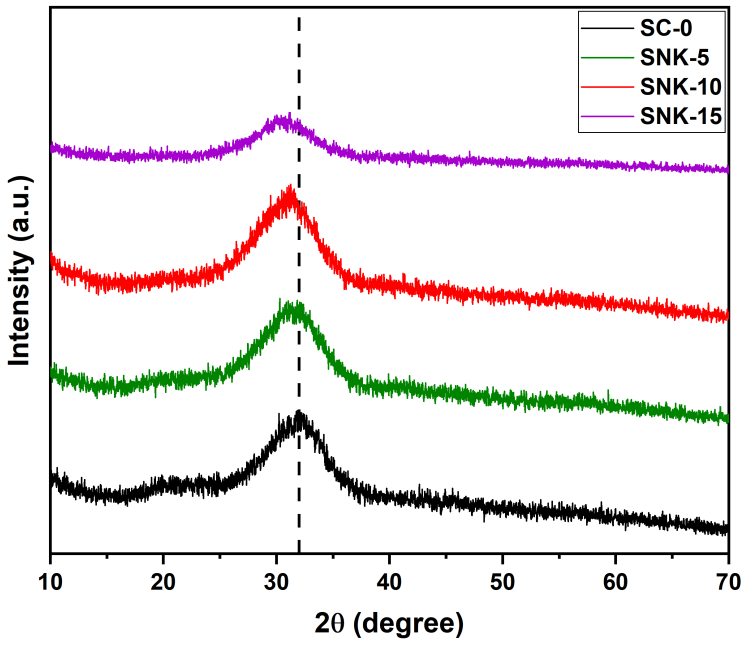

Figure 4.18: XRD patterns of SC-0, SNK-5, SNK-10, and SNK-15 glasses

With increasing K_2O substitution for Na_2O, the main hump become broad, while the secondary halo diminishes and eventually disappears at 15 wt% K_2O (SNK-15). This suggests a decrease in immiscibility and a corresponding increase in homogeneity with K_2O content. This trend is attributed to the replacement of the higher field strength Na^+ (0.96 $Å^{-2}$) with the lower field strength K^+ (0.52$Å^{-2}$) [233], as higher field strength cations generally promote immiscibility [196]. Furthermore, the main hump shifts slightly to lower angles with increasing K_2O, consistent with increased homogeneity and the larger ionic radius of K^+ compared to Na^+.

4.2.4 Differential thermal analysis

DTA was used to determine the T_g, and T_c to evaluate the thermal stability of the glasses. DTA curves are shown in **Fig. 4.19**, and the derived thermal properties are summarized in **Table 4.6**.

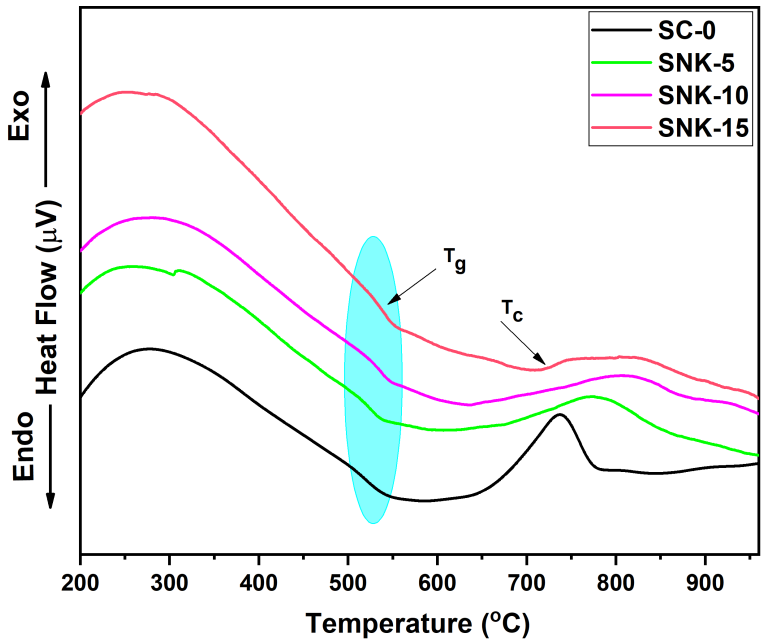

Figure 4.19: DTA curves of as-quenched SC-0, SNK-5, SNK-10, and SNK-15 glasses

Table 4.6: Characteristics temperatures T_g, and T_c taken from the DTA curve and the increasing values of ΔT ($\Delta T = T_c - T_g$) and softening point (T_c) as calculated from dilatometry along with TEC

Sample ID	T_g (°C)	T_c (°C)	ΔT (°C)	T_s (°C)	TEC ($\times 10^{-6}$/°C)
SC-0	525	674	149	497	15.8
SNK-5	526	679	153	497	17
SNK-10	530	683	153	507	10
SNK-15	535	700	165	508	12

Both T_g and T_c exhibit an increasing trend with increasing K_2O content, consistent with the findings of Avramov *et al.* [234][163]. This trend is attributed to the spatial hindrance effect of the larger K^+ ion compared to Na^+ . The larger K^+ hinders the mobility of modified SiO_4^{4-} tetrahedra, reducing devitrification and increasing T_g and T_c of the glass [163]. The conversion of

some NBOs to BOs, as observed in the FTIR spectra Section 4.2.6, is likely to contribute to this increase.

The onset of T_c increases with higher K_2O, and the T_c peaks broaden. This broadening suggests slower crystallization, potentially due to the disruption of the glass network by the larger K^+ ions and the mixed alkali effect, where the presence of both Na^+ and K^+ creates competing interactions that hinder crystallization [215]. Overall, there is an increase in thermal stability ($\Delta T = T_c - T_g$) with increasing K_2O, reaching 165 °C for SNK-15. This wider sintering window (ΔT) can be advantageous for biomedical applications requiring high sintering temperatures and delayed crystallization [235].

4.2.5 Thermal expansion coefficient

The thermal expansion coefficient (TEC) exhibits a non-linear trend with increasing K_2O substitution. The TEC initially increases from SC-0 to SNK-5, then decreases for SNK-10 and SNK-15 (**Table 4.6**). The highest TEC (17×10^{-6}/°C) is observed for SNK-5, and the lowest (10×10^{-6}/°C) for SNK-10. SNK-15 shows a slight increase in TEC (12×10^{-6}/°C). While a decreasing TEC generally suggests the formation of stronger bonds, the non-linearity in this series complicates this interpretation. The softening temperature (T_s) increases with increasing K_2O, consistent with the DTA results and indicative of enhanced thermal stability. The measured TEC values are slightly higher (except SNK-10 glass) than the required values for bioactive glasses, human teeth, coatings for orthopedic substrates, and enamel (8–10 $\times 10^{-6}$/°C) [143][146].

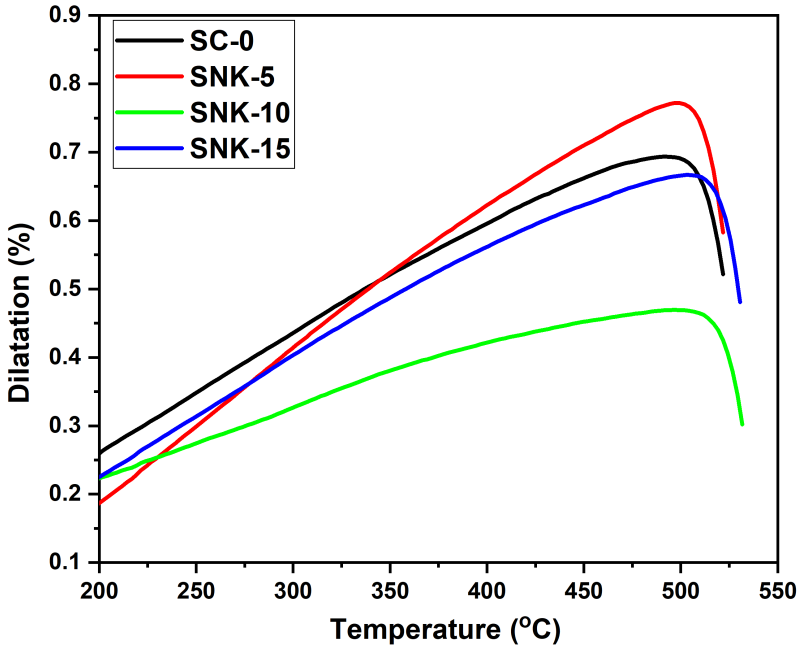

Figure 4.20: Dilatometery curve obtained from the as quenched glass frits of different glass samples at the heating rate 5 °C/min in air

4.2.6 FTIR analysis

FTIR spectra of the glasses (**Fig. 4.21**, FTIR spectra in the range from 4000-400 cm^{-1} is shown in Appendix **Fig. A1(b)**) reveal slight band shifts and broadening, indicative of changes in the silicate and phosphate networks with increasing K_2O content in the glasses. Higher K_2O concentrations influence the silicate structural units, causing bands, particularly in the 800-1200 cm^{-1} range associated with Si-O-Si and P-O bond vibrations, to shift to lower wavenumbers and broaden. This broadening suggests an increase in structural disorder, likely due to the larger size of K^+ (1.34 Å) compared to Na^+ (0.96 Å) [236].

Initially, adding K_2O disrupts the silicate network, decreasing the intensity of the 1012 cm^{-1} band and forming Si-OH^- groups at 1226 cm^{-1}, which enhances water absorption and benefits the physiochemical reactions during in vitro testing [236]. Increasing K_2O up to 10 wt% causes slight shifts in the 500-700 cm^{-1} range and intensifies the 1012 cm^{-1} band without silanol group formation as compared to SNK-5 and SNK-15 glass. Above 10 wt% K_2O, this

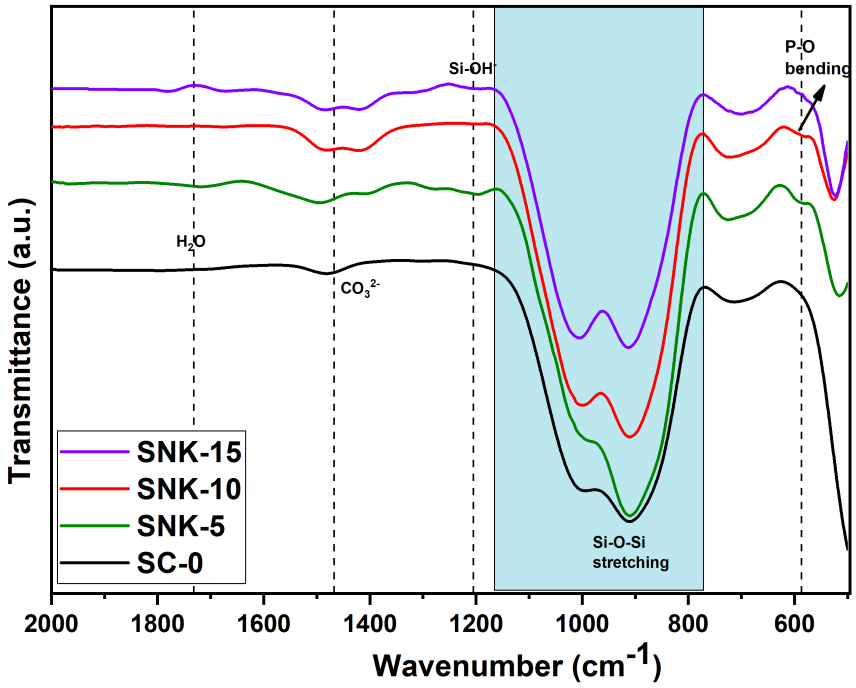

Figure 4.21: FTIR spectra of SC-0, SNK-5, SNK-10, and SNK-15 glasses

band's intensity decreases, with the emergence of a silanol band, indicating a stronger mixed alkali modifier effect (Na_2O/K_2O ratio ~1). Mixed modifier effects are known to be most prominent when the ratio of two modifier oxides, mixed former, and mixed intermediate oxides approaches unity, as discussed earlier and widely reported in the literature [198][237].

To further investigate the structural changes, the fingerprint region was deconvoluted as shown in **Fig. 4.22**. Bands in the 500-730 cm^{-1} range are attributed to Si-O-Si stretching, while the band at 587 cm^{-1} corresponds to P-O bending vibrations [209]. These bands are relatively weak due to the low phosphorus content. In the 740-1200 cm^{-1} range, the intense band around ~909 cm^{-1} denotes Si-O-NBO asymmetric stretching, with the dominance of Q^1 units increasing with K_2O [210]. The band at 1031-1065 cm^{-1} represents changes in PO_4^{3-} vibrations, and the band at 1480 cm^{-1} is attributed to carbonyl groups, potentially related to carbonate remained in the eggshell pores [58], which is also observed in the MgO-series glasses (as discussed in the section 4.2.5).

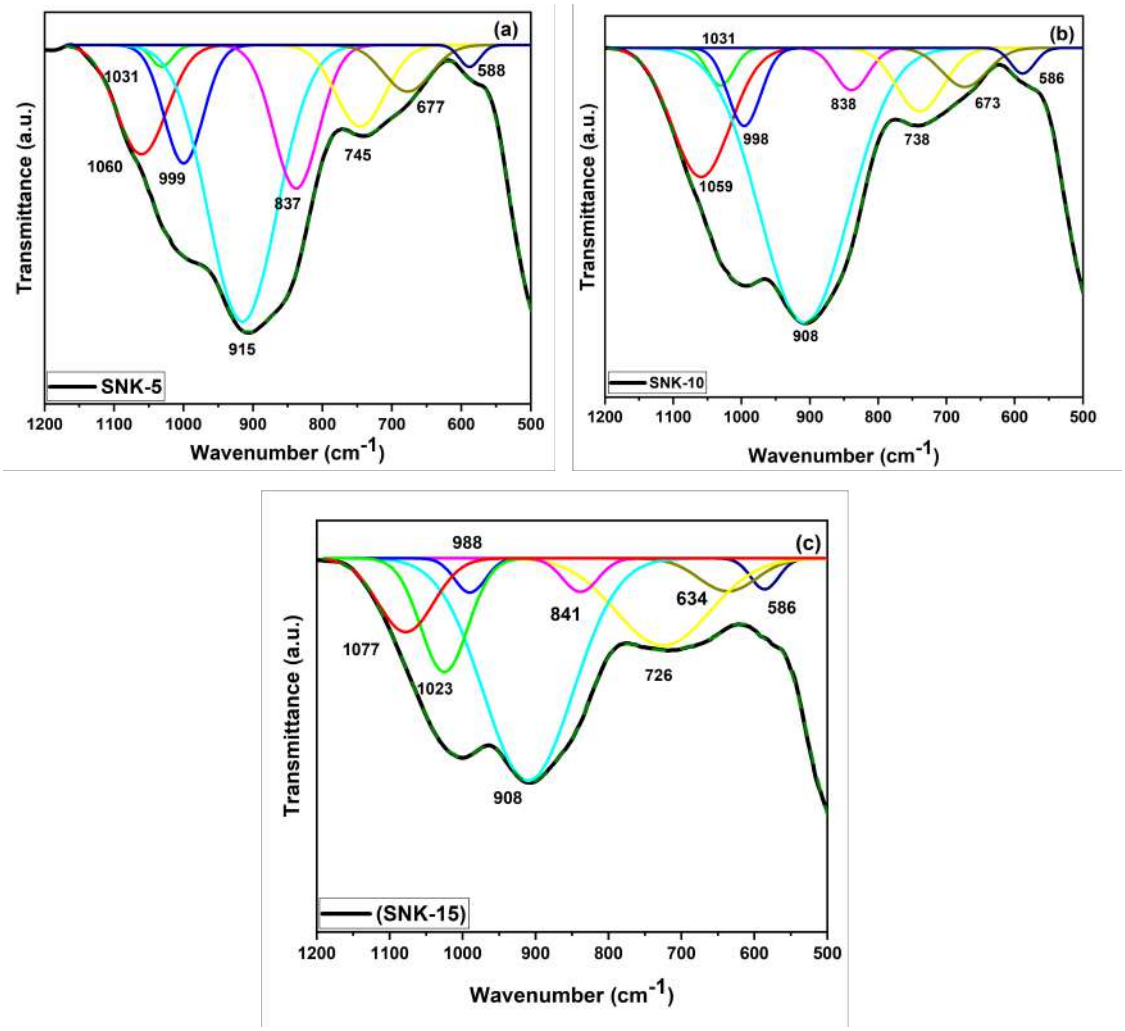

Figure 4.22: Deconvoluted FTIR spectra of (a) SNK-5, (b) SNK-10, and (c) SNK-15 glasses

FTIR analysis reveals an increase in the proportion of Q^1 and Q^3 structural units with increasing K_2O content, coupled with a decrease in Q^2 units. This trend suggests a conversion of some NBOs into BOs, as shown in the deconvoluted spectra (**Table 4.7**). To further quantify these changes, the fractions (f_0, f_1, f_2, f_3) of the different Q^n units were calculated using the following equations:

$$f_0 = \frac{A(Q^0)}{A(Q^0) + A(Q^1) + A(Q^2) + A(Q^3)} \tag{4.2}$$

$$f_1 = \frac{A(Q^1)}{A(Q^0) + A(Q^1) + A(Q^2) + A(Q^3)} \tag{4.3}$$

$$f_2 = \frac{A(Q^2)}{A(Q^0) + A(Q^1) + A(Q^2) + A(Q^3)} \tag{4.4}$$

$$f_3 = \frac{A(Q^3)}{A(Q^0) + A(Q^1) + A(Q^2) + A(Q^3)} \tag{4.5}$$

where $A(Q^n)$ represents the area of the corresponding Q^n peak.

Table 4.7: Area of Q^3, Q^2, and Q^1 units along with Q^3/Q^2, Q^2/Q^1, and Q^3+Q^2/Q^1 ratio of deconvoluted structural units of silicate to know about the change in various structural units of glass network

Sample ID	Q^3	Q^2	Q^1	Q^3/Q^2	Q^2/Q^1	$(Q^3+Q^1)/Q^2$	f_0	f_1	f_2	f_3
SC-0	0.88	62.52	74.2	0.014	0.84	1.20	0.13	0.46	0.39	0.003
SNK-5	30.3	25.36	105	1.19	0.24	5.33	0.18	0.53	0.12	0.15
SNK-10	43.1	14.61	140.9	2.95	0.10	12.61	0.03	0.68	0.07	0.20
SNK-15	20.4	5.30	99.4	3.85	0.05	22.61	0.04	0.75	0.04	0.15

The calculated f_n values, presented in **Table 4.7**, show that f_0 and f_2 decrease with increasing K_2O, while f_1 and f_3 increase. Overall, the results indicate an increase in the odd structural units as compared to the even structural units. This trend is likely due to the mixed alkali effect arising from the presence of both Na^+ and K^+ modifiers [238].

4.2.7 Hardness of pristine glasses

The Vickers hardness of the pristine glasses, as shown in **Fig. 4.23**, increases with increasing K_2O content, ranging from ∼4.6 to 6.02 GPa. However, SNK-10 deviates from this trend, potentially due to the more pronounced mixed-modifier effect discussed in the above sections. Despite K^+ having a lower field strength than Na^+, substituting Na^+ with K^+ does not decrease the hardness. This may be attributed to local structural distortions introduced by the K^+ substitution, potentially increasing hardness [205]. These values fall within the

acceptable range for bioactive glasses [217], surpassing even Hench's glass. The increase in BOs relative to NBOs with increasing K_2O, along with decreased phase separation, may contribute to the enhanced hardness. The absence of fractures during indentation (**Fig. 4.24**) indicates good fracture toughness of these glasses. In other words, the developed glasses may have better technological properties like machinability etc.

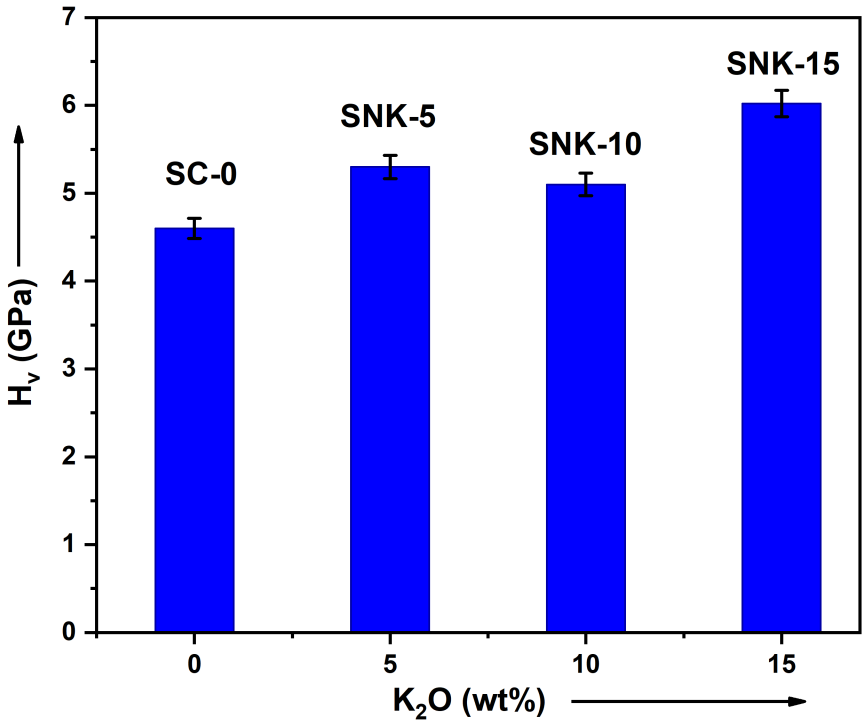

Figure 4.23: Histogram represents the Vickers Hardness (GPa) with increasing K_2O (wt%) in glass composition

The K_2O series exhibited lower hardness values (5.3–6.02 GPa) compared to the MgO series (6.1–6.5 GPa). This difference may be attributed to the more open glass structure resulting from the larger size of K^+ replacing Na^+ compared to the smaller Mg^{2+} replacing Ca^{2+}. This open structure is also consistent with the lower thermal stability observed in the K_2O series compared to the MgO series. However, both series exhibit higher thermal stability and hardness compared to the SC-0 base glass (4.6 GPa). The mixed modifier effect, evident in both series as the ratio of modifiers approaches unity, likely

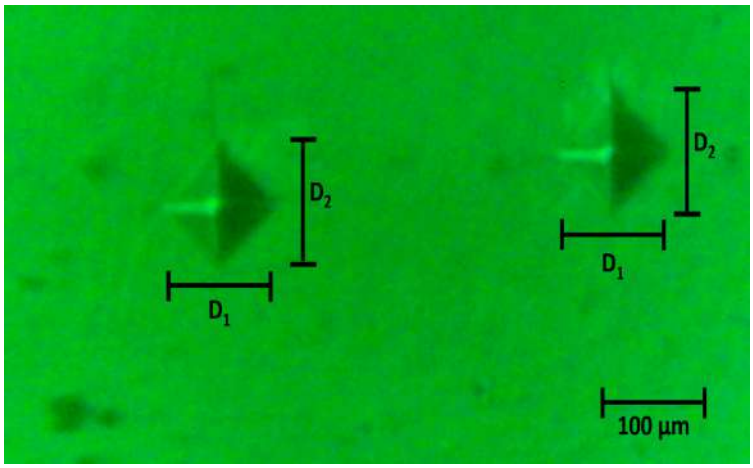

Figure 4.24: Representative image of Vickers indentation marks on SNK-15 glass observed by Eclipse-MA100, Nikon equipment, where D_1 and D_2 are the lengths of diagonal indent

contributes to the non-linear trends observed in various properties.

4.2.8 In-vitro testing of bioactivity

4.2.8.1 Biodegradability

The pH change of the SBF solution upon glass immersion (**Fig. 4.25(a)**) is a key indicator of bioactivity. Initially, a rapid pH increase from 7.34 to 8.2 within 10 days is observed, driven by the release of Na^+, K^+, and Ca^{2+} ions from the glasses into the SBF and their exchange with H^+ or H_3O^+ ions. The change in the pH value is related to the dissolution of the glasses in SBF. As discussed in FTIR analysis (Section 4.2.6), the formation of the Si-OH^- group increases with K_2O content. So, it is responsible for early changes in pH values and the degradability of glasses.

This elevated pH indicates the dissolution of the silica glass network, resulting in the formation of better silanol groups and a subsequent decrease in pH in the second step. The fluctuations in pH over time are governed by the overall concentration of acidic ions like Si^{4+} and basic ions such as K^+, Ca^{2+}, and Na^+ in the SBF. After the initial surge, there is typically marginal or no further change in pH, indicating a stabilization of the ion exchange process between SBF and glasses. Chemically, it can be explained as follows:

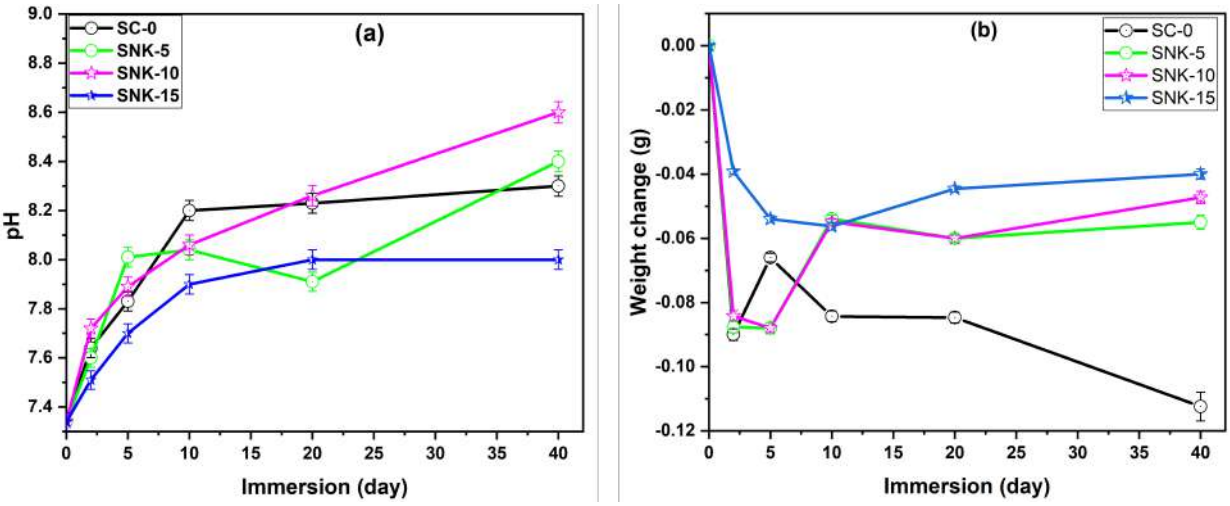

Figure 4.25: pH and weight change of glasses in SBF. (a) pH change of SNK glasses compared to SC-0. (b) Weight change over time. Error bars indicate standard deviation

$$\text{Si-O-K}^+/\text{Na}^+ + \text{H}^+ \rightarrow \text{Si-OH}^- + \text{K}^+/\text{Na}^+ \tag{4.6}$$

The pH and weight changes of the glasses during immersion in SBF (**Fig. 4.25**) are closely related and reflect alterations in the chemistry of the glass surface due to ion leaching from the glasses. This pH decrease suggests potential network breakage due to leaching of the glassy matrix, exposing a fresh surface and reducing the demand for H^+ ions. SNK-5 and SNK-15 show higher biodegradability, likely facilitated by $Si\text{-}OH^-$ groups, which promote HAp layer formation. Conversely, SNK-10's continuous pH increase is attributed to ongoing Si^{4+} leaching, supported by MP-AES analysis. SNK-10 also shows less Ca^{2+} and Na^+ leaching, consistent with its weight gain at 20 days. Among the K_2O glasses, SNK-5 exhibits the greatest weight loss, and SNK-15 the least, with SNK-15 reaching maximum weight gain at 20 days. This weight gain correlates with reduced Ca^{2+} in SBF and its deposition on the glass surface (EDS analysis, **Table 4.8(b)**). K_2O glasses show continuous weight gain up to 40 days, unlike SC-0, which shows weight loss after 20 days. As discussed previously, the single alkali oxide glass (SC-0) shows a different weight loss trend, likely due to its higher initial Ca^{2+} leaching and resulting porosity in the immersed glasses. This difference influences the kinetics of HAp formation and dissolution. The pH and weight changes after SBF immersion are

related to HAp layer formation. Furthermore, the presence of two modifiers in comparable ratios can significantly alter the glass behavior. Therefore, glass compositions can be tailored for specific needs and applications in the human body. In comparison to the MgO glass series, the K_2O-containing glasses show higher weight loss changes due to their more open structure.

4.2.9 MP-AES analysis

MP-AES was used to quantify ion concentrations in SBF after glass immersion for 20 and 40 days (**Table 4.8**). The results indicate that among the glass containing K_2O, increasing K_2O concentration results in the maximum leaching across all the glasses, indicating heightened susceptibility to physicochemical reactions compared to reference SC-0 glass and MgO contained glasses. As previously discussed, the formation of Si-OH^- groups increases with increasing K_2O concentration. The lower field strength of K^+ compared to Na^+ might be the possible reason behind increased leaching. The physiochemical reactions between alkali ions and H^+ ions play an important role in bone bonding and their regeneration.

Table 4.8: The MP-AES recorded the Ca, K, and Na ion quantity (mg l^{-1}, n = 3) in the SBF solution after 20 and 40 days. The Ca/P (molar ratio) as determined from EDS was compared with the change in the (wt %) of Ca and P before and after immersion for 40 days (mean ± standard deviation, n = 6)

(a) Ion concentrations in SBF solution

Sample	20 days				40 days			
Name	Si	Ca	K	Na	Si	Ca	K	Na
SBF	<1	16.4	257	3508	<1	16.4	257	3508
SC-0	65	135	245	3223	43	50	228	4641
SNK-5	180	219	347	4725	159	141	250	2442
SNK-10	183	174	513	3220	160	138	350	2072
SNK-15	169	278	602	3708	153	254	410	1812

(b) changes in Ca (wt%) and P (wt%) and Ca/P ratio determined from the EDS analysis for unsoaked and soaked glasses after 20 and 40 days

Sample	Unsoaked (0 days)		Soaked (20 days)		Soaked (40 days)		
Name	Ca	P	Ca	P	Ca	P	Ca/P
SC-0	17.1	3.2	18.3	3.4	19.6	5.0	3.8
SNK-5	17.5	3.0	11.7	2.1	14.0	4.1	3.4
SNK-10	17.3	3.5	15.1	1.6	14.2	5.3	2.5
SNK-15	16.9	2.3	15.2	3.2	18.8	8.3	2.2

Compared to the (base) glass SC-0, all K_2O-containing glasses exhibit higher Si^{4+} ion leaching, which is directly associated with glass dissolution. This indicates that glass degradation initiates upon immersion in SBF through the reaction between silica tetrahedral units and water. SNK-15, however, demonstrates less Si^{4+} leaching than SNK-5 after both 20 and 40 days, consistent with the observed decrease in pH after 20 days and the reduced weight loss for this glass observed after 20 days.

Furthermore, K_2O enhances the release of modifier ions (Ca^{2+} and Na^+) while reducing Si^{4+} release. Replacing Na^+ with K^+ appears to facilitate modifier ion leaching while hindering Si^{4+} leaching. Similar trends for Ca^{2+} and Na^+ release with increasing K_2O in S53P4 glass have been reported by Massera *et al.* [239]. This enhanced modifier ion release may contribute to the improved HAp layer formation observed on the SNK-5 and SNK-15 glass surfaces. In contrast, SNK-10 shows the opposite trend, releasing more Si^{4+} than modifier ions. This higher Si^{4+} release delays the formation of the silanol layer and subsequently the calcium phosphate layer, as evidenced by the XRD analysis of SNK-10. This may explain the less pronounced HAp layer formation on SNK-10, even after extended immersion for 20 and 40 days, which is also supported by FE-SEM-EDS analysis.

This series exhibits increased glass dissolution compared to the MgO series. The addition of MgO retards Si^{4+} ion release, likely contributing to the slower and delayed HAp layer formation compared to the K_2O series. In the K_2O series, the higher dissolution of calcium and Si^{4+} ions, compared to both the base glass and the MgO series, promotes earlier formation of the silanol layer, which subsequently facilitates HAp layer development.

4.2.10 FE-SEM and EDS analysis

Fig. 4.26 shows the morphological changes in the glasses before and after immersion in SBF. Initially, a sponge-like layer forms on the glass surface, followed by the development of spherulite or globular structures composed of flakes. These structures grow over the spongy layer with increasing immersion time, particularly evident in SNK-5 and SNK-15 over 20 and 40 days. The

increasing calcium (Ca) and phosphorus (P) content observed in EDS analysis confirms the development of an HAp layer on the glass surface after immersion.

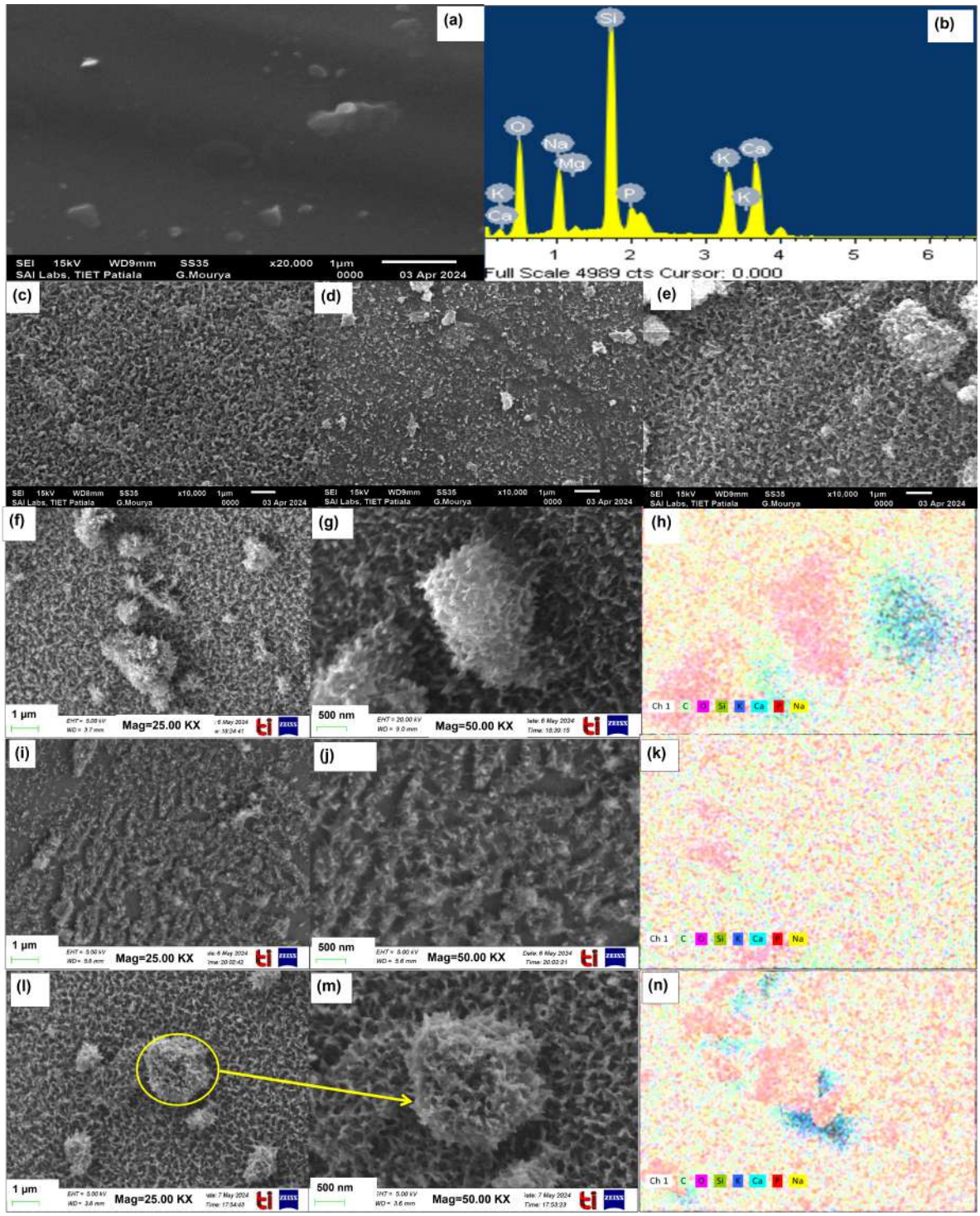

Figure 4.26: (a) Representative SEM and (b) EDS analysis of SNK-15 glass before immersion (c, d, e) SNK-5, 10 and 15 glass after 20 days at 20X (f, i, l) SNK-5, 10, and 15 glass after 40 days at 25X (g, j, m) 40 days at 50X (h, k, n) EDS area mapping of SNK-5, 10, and 15 at 40 days

Interestingly, all glasses with K_2O addition exhibit better HAp layer forma-

tion than the glasses without K_2O and glasses with MgO addition (as explained in first series). However, SNK-10 (10 wt% K_2O) shows less prominent HAp growth than SNK-5 and SNK-15 even after 40 days. This could be due to continuous Si^{4+} leaching into SBF, delaying the formation of the Si-OH^- layer necessary for calcium phosphate deposition. This observation is consistent with the XRD, FTIR, and MP-AES results.

EDS mapping reveals a carbonated hydroxyapatite (c-HAp) layer on all glasses, supported by the increased intensity of the CO_3^{2-} band in FTIR spectra. The Ca/P ratios for the K_2O glasses (2.26–3.4) are higher than the standard stoichiometric HAp ratio (1.67). Notably, SNK-15 shows a significant decrease in Ca/P ratio, approaching the values reported for c-HAp in the literature [71]. The formation of the HAp layer in the present glasses contrasts with results reported in the literature for the glasses synthesized using conventional chemicals with K_2O substitution, where K_2O is reported to retard the HAp layer formation on the glasses [46][239][240].

4.2.11 XRD analysis

XRD patterns of the pristine glasses and after immersion in SBF for various durations are shown in **Fig. 4.27**. Minor changes are observed after immersion, with weak diffraction peaks corresponding to semi-crystalline hydroxyapatite (HAp) (ICDD card no. 01-072-1243) appearing at $2\theta \approx 32^\circ$ in all immersed glasses. Feeble peaks corresponding to tetracalcium phosphate (TTCP) (ICDD card no. 01-070-1379) are also observed. TTCP, composed primarily of calcium and phosphorus, often appears as an intermediate phase during HAp formation, particularly when the Ca/P ratio is > 2 [224][225].

No HAp formation is detected in SNK-5, SNK-10, and SC-0 glass after 2 days of immersion in SBF. In contrast, SNK-15 shows weak peaks for both HAp and TTCP after 2 days, with stable HAp formation up to 40 days. Both, SNK-5 and SC-0 show both phases after 5 days. The stable HAp formation is recorded in SNK-5 and SNK-15 samples compared to SC-0 glass. No HAp is observed in SNK-10 after 5 days; however, weak TTCP peaks appear after 10 days, and HAp forms after 40 days. This delayed HAp formation in SNK-10 is

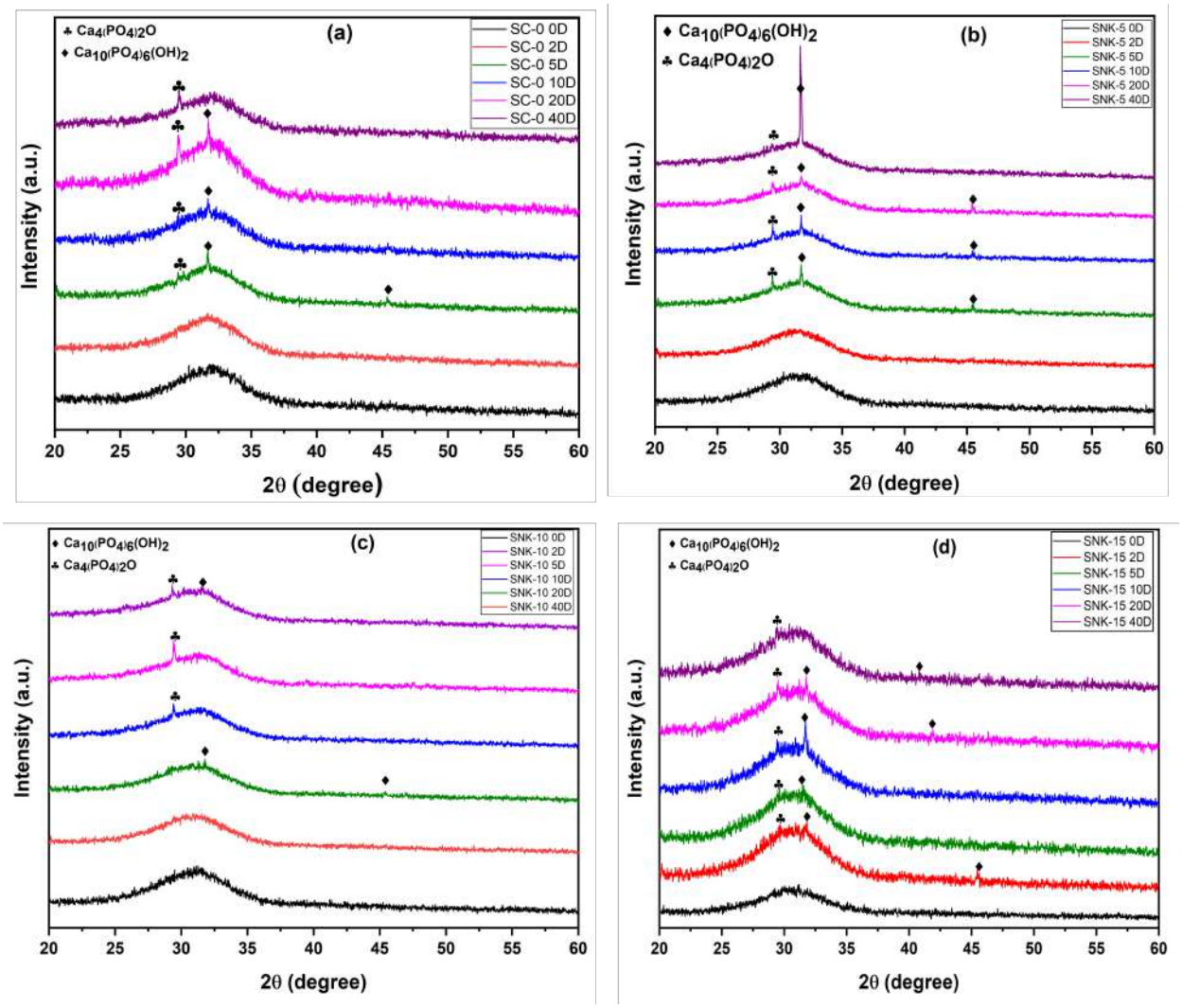

Figure 4.27: The XRD pattern of pristine glasses (a) SC-0 (b) SNK-5 (c) SNK-10 (d) SNK-15 in comparison with the glasses after immersion in SBF solution for different time period

consistent with the weight change and MP-AES analysis of SBF.

Similar to the MgO series, minimal changes are observed in the K_2O glasses after 2 days of immersion. However, HAp layer formation occurs earlier in the K_2O series compared to the MgO series. The TTCP phase is observed in all K_2O glasses, likely due to the consistent calcium content, unlike the MgO series where CaO is systematically replaced. Similar to SCM-10, SNK-10 exhibits delayed formation of both TTCP and HAp, possibly due to the mixed modifier effect. The comparable concentrations of Na_2O and K_2O in SNK-10 and CaO and MgO in SCM-10 likely lead to a competitive interaction between these modifiers, influencing the observed behavior.

4.2.12 FTIR analysis

FTIR spectra of the glasses after immersion in SBF reveal notable changes in their structural composition as shown in **Fig. 4.28** (FTIR spectra in the range from 4000-400 cm^{-1} is shown in Appendix **Fig. A3**). The increased FWHM with immersion time indicates greater structural disorder and porosity. The intense $Si\text{-}OH^-$ band at ~1200 cm^{-1} and ~1735 $^{-1}$ appears in the immersed glasses at different immersion times [236]. The band at ~910 cm^{-1} gradually merges with the phosphate band at ~1025 cm^{-1} as the immersion time increases.

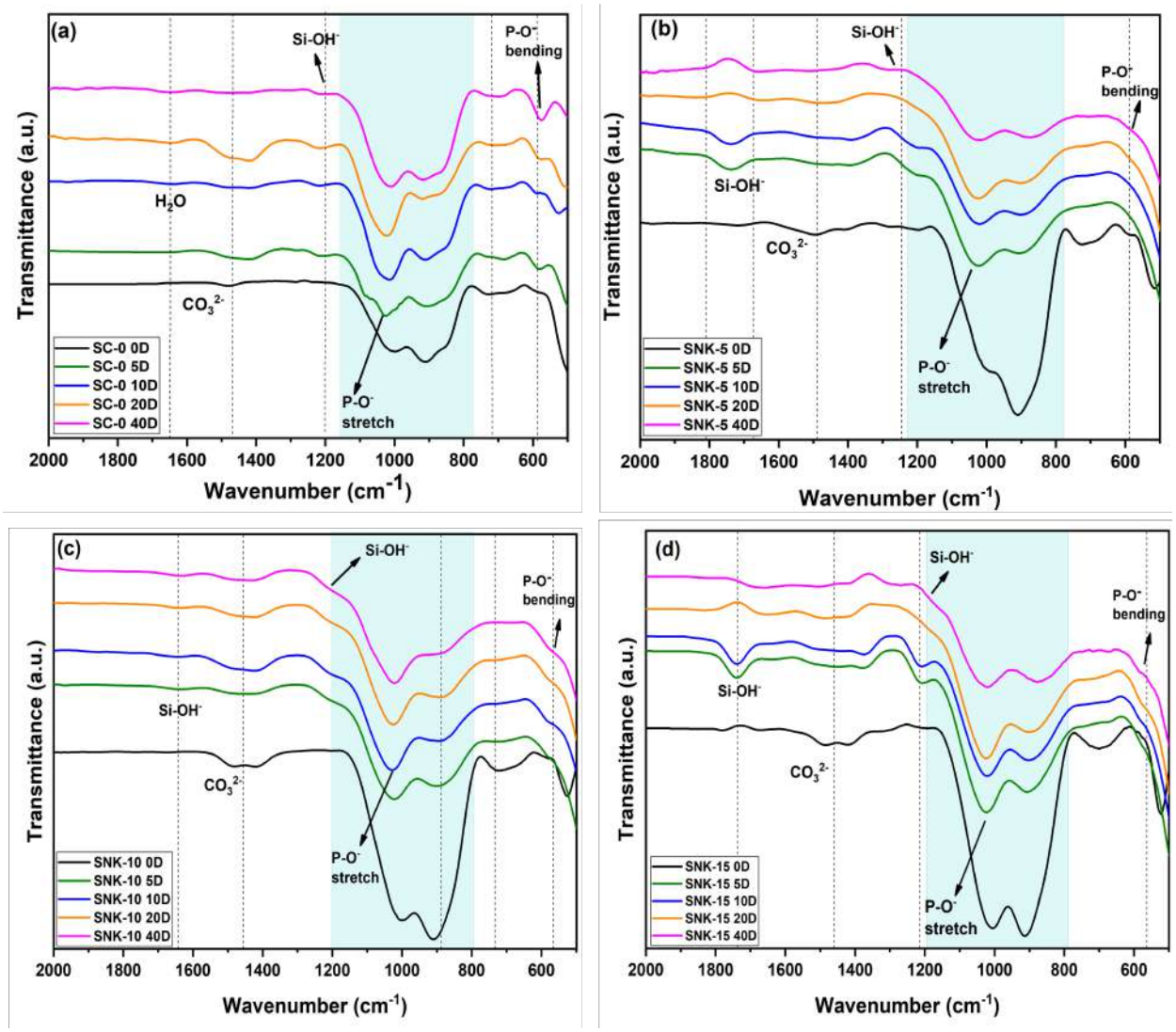

Figure 4.28: FTIR spectra of pristine glasses: (a) SC-0, (b) SNK-5, (c) SNK-10, (d) SNK-15; and after immersion in SBF for 0, 5, 10, 20, and 40 days

SNK-5 and SNK-15 show intense phosphate bands after 20 days, while SNK-

10 exhibits delayed dissolution, with a strong phosphate band appearing only after 40 days. The early formation of the silanol layer (after 5 days) in SNK-5 and SNK-15 suggests that it acts as a base to HAp formation. In the fingerprint region, all samples show similar behavior, with increasing intensity of the P-O bending band at ∼587 cm^{-1} and the appearance of a new band at 605 cm^{-1}, indicating HAp formation [168][241]. The pronounced band at ∼1450 cm^{-1} (CO_3^{2-}) confirms the formation of carbonated hydroxyapatite (c-HAp), consistent with EDS results. SNK-10 shows significant changes in the Si-O-Si stretching band at 910 cm^{-1} [210], in correlation with the extensive Si^{4+} leaching observed in MP-AES analysis, likely contributing to its delay in HAp formation.

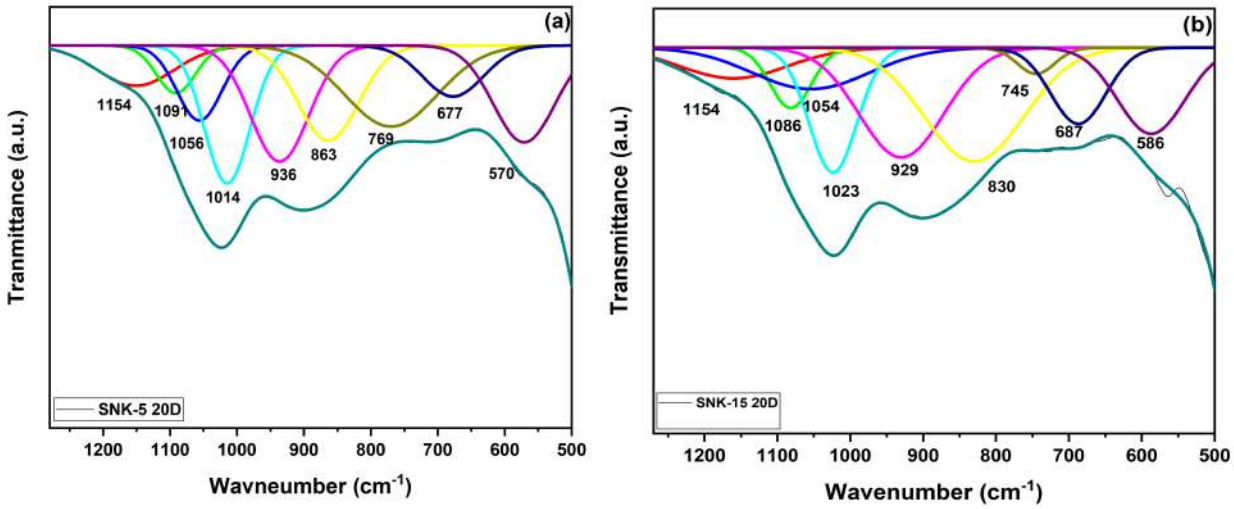

Figure 4.29: Deconvoluted FTIR spectra of (a) SNK-5 and (b) SNK-15 glasses after 20 days in SBF

Deconvoluted FTIR spectra (**Fig. 4.29**) provide more detailed insights into structural changes. The deconvoluted spectra show increased intensity and shifts to higher frequencies compared to pristine glasses, which is expected after SBF immersion. These findings underscore the exciting transformations in glass's structural composition with immersion time, highlighting the interplay between silanol and phosphorus units in forming HAp layers. The distinct behavior of the SNK-10 samples, with its delayed yet intense changes, offers intriguing insights into the dissolution and reformation processes in bioactive glasses. Interestingly, carefully selecting two distinct modifiers in an approximate ratio i.e. ∼1 may help to develop bioactive materials with improved

thermal and corrosion resistance materials for biomedical applications. These materials can be tailored to have either higher or lower pH values, making them suitable for compatibility with human plasma as well as fillers in teeth.

FTIR results indicate more pronounced structural changes in the K_2O series compared to the MgO series. The K_2O glasses exhibit intensified silanol bands, even in the pristine state, potentially due to their more open structure. This open structure, compared to the MgO series, likely leads to greater structural modification upon immersion. The FTIR spectra also reveal more intense c-HAp formation in the K_2O series compared to both the MgO series and the base glass.

4.2.13 MTT assay

The MTT assay was used to evaluate the effect of the glasses on cell viability at concentrations up to 200 μg/ml as shown in **Fig. 4.30(a)**. Additionally, the effect on human peripheral blood mononuclear cells (PBMC) was monitored over different time durations up to 48 h using a constant concentration of 100 μg/ml (**Fig. 4.30(b)**). The results demonstrated that cell viability remained unaffected across all glasses at concentrations up to 200 μg/ml and even after 48 h of treatment with 100 μg/ml.

The findings of the present bioglasses reveal that none of the glasses were cytotoxic to PBMC, maintaining viability above the threshold value i.e., >30% according to ISO10993-5 standard as mentioned earlier [229] . Statistical analysis using a one-way ANOVA test confirmed no significant differences among the treated cells ($p < 0.05$). Interestingly, glasses with less HAp formation (SC-0 and SNK-10) did not show cytotoxic effects. Notably, SC-0 exhibited high cell proliferation. The biocompatibility of K_2O-doped mesoporous bioactive glass has been previously reported at a concentration of 20 μg/ml on human normal fibroblast cells [171]. Overall, the present glasses demonstrate good cytocompatibility with PBMCs.

In contrast to the MgO series, the K_2O glasses exhibit lower cell viability over time. The MgO series maintains high viability (up to 85% at 200 µg/ml

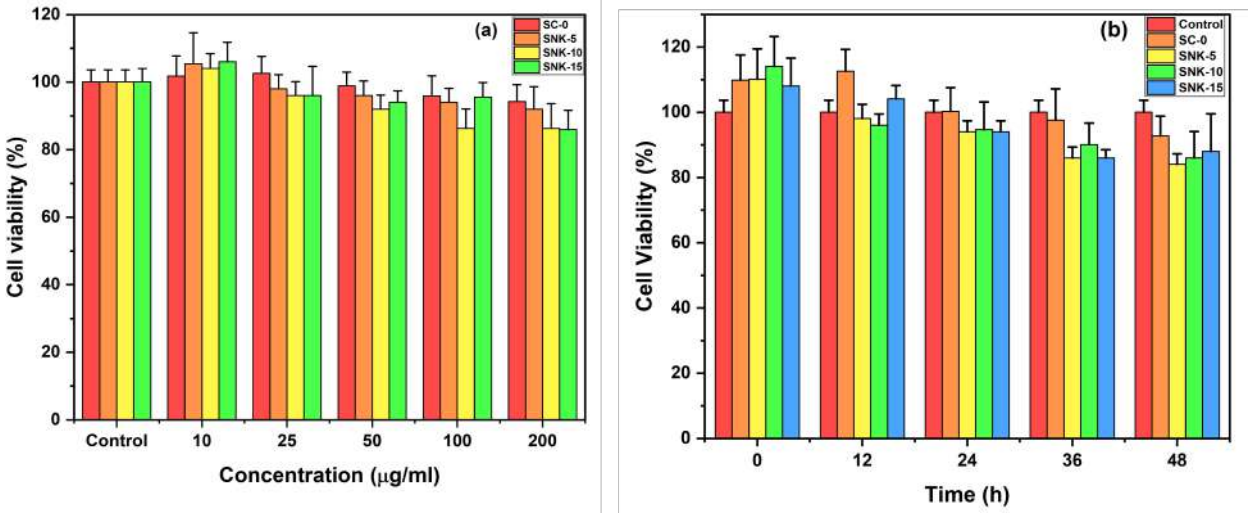

Figure 4.30: Cell growth effect of (a) different concentrations of SC-0, SNK-5, SNK-10, and SNK-15 on human PBMC cells, and (b) at different time intervals with a constant concentration (100 µg/ml) of SC-0, SNK-5, SNK-10, and SNK-15. Data are presented as mean ± std.dev. of three independent experiments. The bar represents that the data is not significantly different at (p- value > 0.05)

and 94% at 100 µg/ml) even after 48 hours. While the K_2O glasses initially show comparable viability (up to 86% at 200 µg/ml), viability decreases over time, reaching 83% for SNK-5 and 85% for the other K_2O glasses. This reduced viability in the K_2O series may be attributed to the higher ion leaching rate compared to the MgO series (Section 4.2.9).

4.3 Comparative study of glasses

Based on the bioactivity, biocompatibility, and other properties of glasses, three of the best compositions were synthesized using conventional chemicals to validate and compare the results with glass synthesized by hybrid sources, i.e., biowaste and conventional chemicals. Glasses with composition $43SiO_2$-$25CaO$-$25Na_2O$-$7P_2O_5$, $43SiO_2$-$10CaO$-$15MgO$-$25Na_2O$-$7P_2O_5$, and $43SiO_2$-$25CaO$-$10Na_2O$-$15K_2O$-$7P_2O_5$ are designated as MS-0, MM-15, and MK-15, respectively. The properties of these synthesized glasses are discussed below and compared with those of the hybrid-source-derived glasses of similar compositions.

4.3.1 Physical paramter

The densities MS-0, MM-15, and MK-15 glasses are 2.8 g/cm^3, 2.64 g/cm^3, and 2.7 g/cm^3, respectively. These values are slightly different from the hybrid-source-derived glasses i.e., SC-0, SCM-15, and SNK-15 glasses. However, the trends in density and molar volume remain consistent across both sets of glasses. **Table 4.9** summarizes the density, molar volume (V_m), and oxygen packing density (OPD) of the conventional glasses compared with those derived from hybrid-sources.

Table 4.9: Density (ρ), molar volume (V_m), and oxygen packing density (OPD) of conventionally prepared glasses. The values of Hybrid-source-derived glasses are shown in parentheses below each corresponding conventional value.

Glass ID	ρ (g/cm^3)	V_m (cm^3/mol)	OPD (mol/cm^3)
MS-0	2.8	22.12	70.7
(SC-0)	(2.7)	(22.9)	(68.2)
MM-15	2.64	21.9	69.8
(SCM-15)	(2.63)	(22.0)	(69.3)
MK-15	2.7	24.17	66
(SNK-15)	(2.61)	(24.9)	(63.8)

Similar to the hybrid-source-derived series, the addition of MgO in MM-15 leads to a decrease in both density and molar volume compared to MS-0. This is attributed to the smaller ionic radius and higher field strength of Mg^{2+} relative to Ca^{2+}, resulting in a more compact network [161][194]. Conventionally derived glasses exhibit slightly higher density and OPD and lower V_m compared

to their hybrid-source-derived counterparts. This difference is likely due to the higher porosity often observed in bioactive glasses derived from biowaste sources [52][221].

Likewise, MK-15 exhibits a decrease in density and an increase in molar volume is observed compared to MS-0, which is consistent with the potassium-substituted hybrid-source-derived glasses. This is due to the substitution of the smaller Na^+ ion (1.02 Å) with the larger K^+ ion (1.34 Å), which disrupts the network, resulting in a more open structure and an increased molar volume. This structural change is also reflected in the lower oxygen packing density. The lower field strength of K^+ (0.52 $Å^{-2}$) compared to Na^+ (0.96 $Å^{-2}$) further contributes to this less compact structure [165][195][231]. These results confirm that hybrid-source-derived glasses exhibit a more open structure compared to conventionally derived glasses.

4.3.2 XRD analysis

XRD analysis confirmed the amorphous nature of all conventionally prepared glasses, as evidenced by the broad halo observed around 32° (**Fig. 4.31**). Similar to the hybrid series, a second halo at ∼20° is present in MS-0. This second halo becomes more prominent with MgO addition in MM-15 in comparison to MS-0 glass, mimics the trend observed in the hybrid sources obtained MgO glasses and suggesting an increased tendency for phase separation. As discussed previously, network-modifying cations with higher field strengths can promote phase separation [196].

In contrast, the 20° halo disappears entirely with K_2O addition (MK-15), indicating decreased phase separation, consistent with the observations in the hybrid-source-derived K_2O glasses i.e., SNK-15. This is likely due to the substitution of the higher field strength Na^+ (0.96 $Å^{-2}$) with the lower field strength K^+ (0.52 $Å^{-2}$). Higher field strength cations are known to increase immiscibility [196]. The slight shift of the main halo to lower angles with increasing K_2O content further supports increased homogeneity and is consistent with the larger ionic radius of K^+ compared to Na^+. Thus the XRD pattern of hybrid sources derived glasses and conventional chemical derived glasses are more or

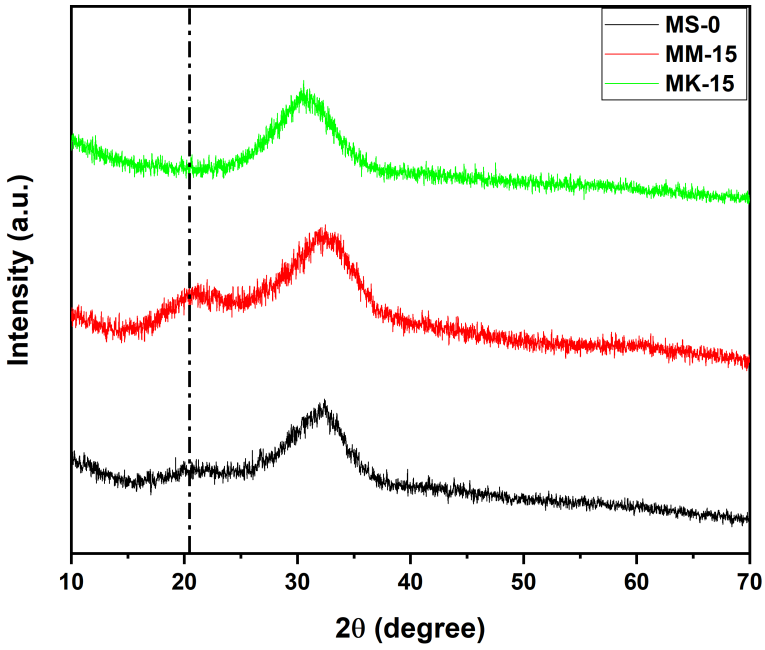

Figure 4.31: The X-ray diffraction patterns of MS-0, MM-15, and MK-15 glasses

less follow the similar trend.

4.3.3 Differential thermal analysis

DTA was performed on the conventionally prepared glasses (as shown in **Fig. 4.32**) to determine their thermal properties and compare them with the hybrid-source-derived glasses. The results, summarized in **Table 4.10**, show similar trends to the hybrid-source-derived glasses. As expected, T_g decreases with MgO addition (MM-15) and increases with K_2O addition (MK-15).

The decrease in T_g for MM-15 compared to MS-0 can be attributed to the dual nature of MgO and the formation of $(MgO_4)^{2-}$ tetrahedra, which can disrupt the silicate network and lead to weaker Si-O-Mg bonds compared to Si-O-Si bonds. This observation aligns with trends in other MgO-containing bioglasses [194]. The presence of Na^+ ions might also contribute to this T_g decrease due to ion mixing or preferential bonding [157]. Similar to the hybrid-source-derived glasses, the presence of two T_c values, especially in MM-15, suggests an increased tendency for phase separation. Broadening of the crystallization peaks with increasing MgO is also observed, consistent with the

XRD results (Section 4.3.2).

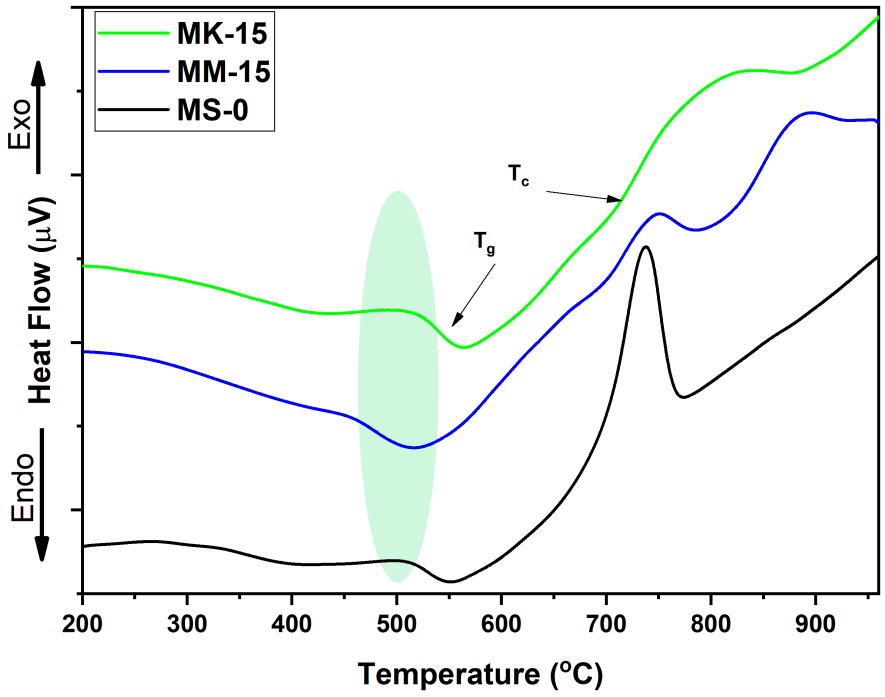

Figure 4.32: DTA thermographs of MS-0, MM-15, and MK-15 glasses

Table 4.10: Represents the thermal parameters of the MS-0, MM-15 and MK-15 glasses. ΔT indicates the sintering window, TEC and T_s (°C) are calculated from dilatometry. The values of Hybrid-source-derived glasses are shown in parentheses below each corresponding conventional value.

Sample ID	T_g (°C)	T_c (°C)	ΔT (°C)	T_s (°C)	TEC ($\times 10^{-6}$/°C)
MS-0	535	684	149	499	15.1
(SC-0)	525	674	149	497	15.8
MM-15	502	716	208	458	12
(SCM-15)	490	720	230	499	10.5
MK-15	547	715	168	510	14
(SNK-15)	535	700	165	508	12

In MK-15, the increase in T_g compared to MS-0 aligns with the behavior of the K_2O-containing hybrid-source-derived glasses and can be attributed to the spatial hindrance effect of the larger K^+ ion compared to Na^+, as discussed previously in section 4.3.4. This effect restricts the mobility of modified SiO_4^{4-} tetrahedra, reducing devitrification [163]. The broadening of the T_c peak in MK-15 suggests slower crystallization, potentially due to glass network disruption by the larger K^+ ions and the mixed alkali effect [215]. Overall, the

addition of K_2O leads to increased thermal stability ($\Delta T = T_c$ - T_g), beneficial for biomedical applications requiring high sintering temperatures and delayed crystallization [235]. The thermal behavior of the conventionally derived glasses closely resembles that of the hybrid-source-derived glasses, validating the use of biowaste for synthesizing bioactive glasses with high thermal stability.

4.3.4 Thermal expansion coefficient

The TECs of the conventionally prepared glasses (MS-0, MM-15, and MK-15) are approximately similar but marginally higher than those of the hybrid-source-derived glasses. MS-0 has a TEC of 15.1 $\times$ $10^{-6}/°C$. Both MM-15 and MK-15 exhibit lower TEC values, 14 $\times$ $10^{-6}/°C$ and 15 $\times$ $10^{-6}/°C$, respectively. It is associated with the higher asymmetric nature of these glasses in comparison to the hybrid-source-derived glasses of similar compositions. The softening temperatures (T_s), summarized in **Table 4.10**, are also comparable to those of the hybrid-derived glasses and consistent with the T_g values obtained from DTA. This similarity in thermal properties between the conventional and hybrid glasses suggests comparable behavior in terms of thermal response of both type of glasses synthesized using two different sources.

The measured TEC values are on higher side in comparison to the range reported for various biomedical applications, including bioactive glasses, dentin and enamel coatings, and orthopedic substrates [143][208].

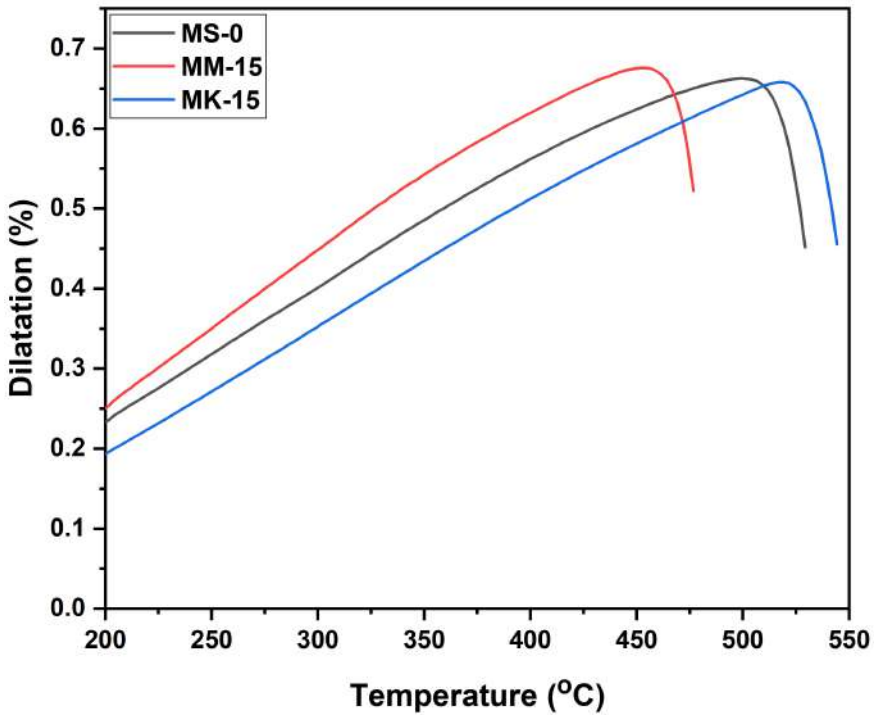

Figure 4.33: Dilatometry curves of the as-quenched MS-0, MM-15, and MK-15 glass frits at a heating rate of 5 °C/min in air

4.3.5 FTIR analysis

The FTIR spectra of the conventionally derived glasses (as shown in **Fig. 4.34**, FTIR spectra in the range from 4000-400 cm^{-1} is shown in Appendix **Fig. A1(c)**) show similar bands to their hybrid-source-derived glasses, primarily featuring silicate-related bands in the 800-1200 cm^{-1} region.

As observed in the hybrid sources derived series with SCM-15, the MM-15 sample exhibits a slight shift of these bands to higher wavenumbers compared to MS-0. The bands between ∼851 and ∼1200 cm^{-1} are attributed to Si-O-Si asymmetric stretching, with possible overlap from phosphorus-related bands in the 900-1200 cm^{-1} region [209][210]. The shoulder band at ∼1014 cm^{-1} shows a slight decrease in intensity with MgO addition. Similar to SCM-15, minor changes are observed in the bands at ∼916 cm^{-1} and ∼850 cm^{-1}. The band at ∼706 cm^{-1}, present in all samples, corresponds to Si-O-Si symmetric stretching vibrations [210]. Additionally, the band at ∼565 cm^{-1} is assigned to P-O asymmetric bending vibrations. [211].

In MK-15 glass, a slight broadening of the spectra is observed, particularly in

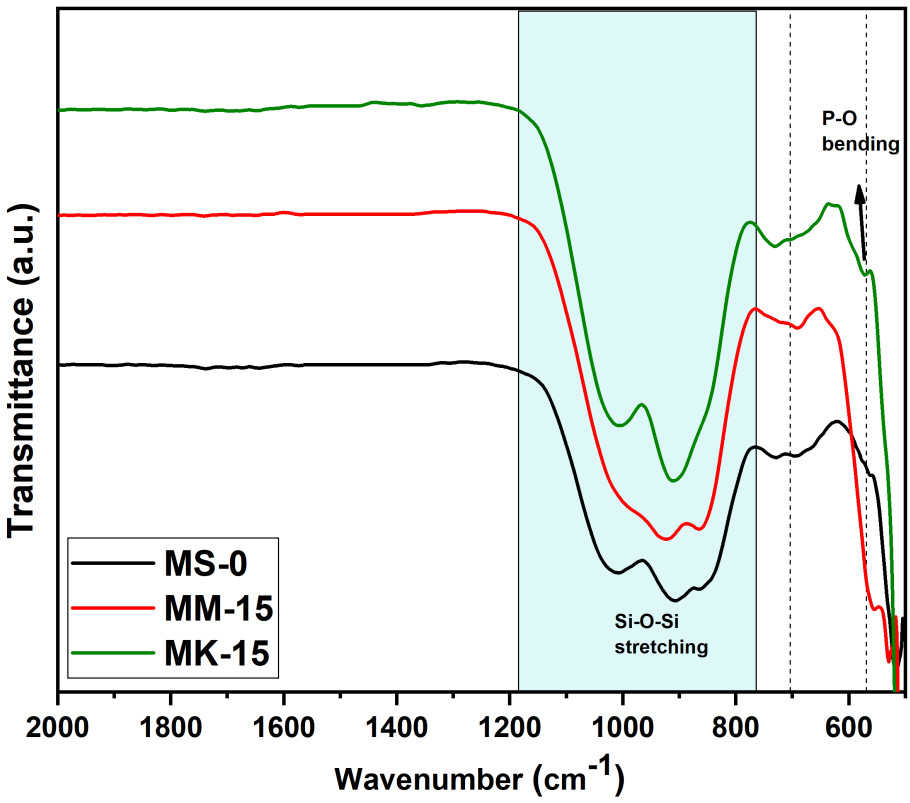

Figure 4.34: FTIR spectra of MS-0, MM-15 and MK-15 glasses

the 800-1200 cm^{-1} region. This broadening suggests an increase in structural disorder, likely due to the larger cationic size of K^+ (1.38 Å) compared to Na^+ (1.02 Å) [236]. Similar bands to those observed in MS-0 and MM-15 are also present in MK-15, indicating the presence of both silicate and phosphate structural units. However, the intensity of the ∼916 cm^{-1} band increases with K_2O addition (MK-15), consistent with the trend observed in the K_2O-substituted hybrid-source-derived glasses.

Table 4.11: Quantitative analysis of Q^n structural units of conventionally derived glasses

Sample ID	Q^3	Q^2	Q^1	$\frac{Q^3}{Q^2}$	$\frac{Q^2}{Q^1}$	$\frac{Q^3+Q^1}{Q^2}$	$\frac{Q^3+Q^2}{Q^1}$	f_0	f_1	f_2	f_3
MS-0	0.28	1.65	2.1	0.17	0.78	1.44	0.92	0.23	0.39	0.31	0.054
MM-15	0.57	2.86	2.2	0.19	1.3	0.96	1.55	0.29	0.27	0.35	0.071
MK-15	1.02	2.05	3.46	0.49	0.59	2.1	0.88	0.16	0.44	0.36	0.13

To further investigate these structural changes, the different Q^n structural

units and their fractions (f_n) were quantified using deconvoluted FTIR spectra in the 600-1200 cm^{-1} region. The results follow a similar trend to that observed in the hybrid-source-derived glasses. With increasing MgO concentration, Q^3 and Q^2 units increase relative to Q^1 units. K_2O addition, on the other hand, leads to an increase in the odd-numbered structural units (Q^3 and Q^1) relative to Q^2, as shown in **Table 4.11**. Overall, the FTIR spectra of the conventionally derived glasses are largely consistent with those of the hybrid-source-derived series.

4.3.6 Hardness

The microhardness of the glasses MS-0, MM-15 and MK-15 is 6.6, 6.25, and 6.3 GPa, respectively, These values are higher compared to their hybrid counterparts: SC-0 (4.6 GPa), SCM-15 (6.1 GPa), and SNK-15 (6.02 GPa).This difference might be due to the formation of more covalent bonds in the conventionally prepared glass structure, leading to increased rigidity and compactness. These results are also consistent with the density and FTIR results of MS-0, MM-15, and MK-15 glasses. This suggests that conventionally derived glasses have greater rigidity than those derived using hybrid sources. However, the hardness of these conventional glasses is still within the range reported for bioactive glasses [216][217]. However, these glasses show cracks in comparison to those of hybrid glasses, indicating that these have low fracture toughness as compared to the hybrid glasses, as shown in **Fig. 4.35**

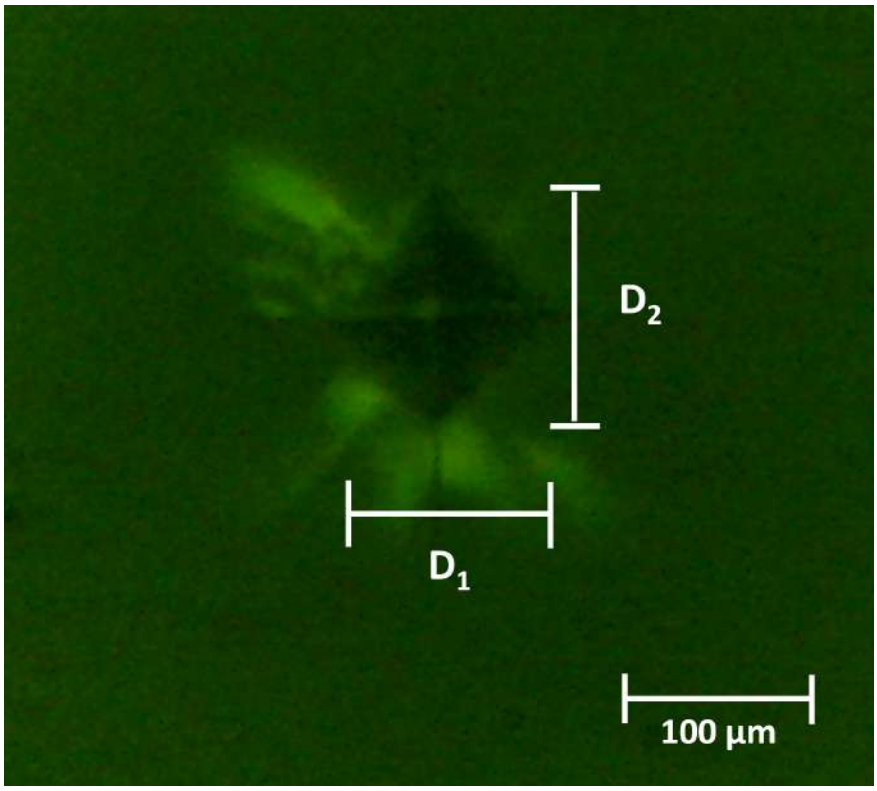

Figure 4.35: Representative image of Vickers indentation marks on MK-15 glass observed by Eclipse-MA100, Nikon equipment, where D_1 and D_2 are the lengths of diagonal indent

4.3.7 In-vitro testing

The in-vitro bioactivity of the conventionally prepared glasses (MS-0, MM-15, MK-15) was evaluated and compared with that of their hybrid sources derived glasses (SC-0, SCM-15, SNK-15).

4.3.7.1 Biodegradability test

The weight change and pH variation during immersion in SBF provide insight into the biodegradability of glasses. **Fig. 4.36** shows the results for the conventional glasses.

MS-0 and MM-15 exhibited maximum weight losses of 5.9% and 6.6%, respectively, after just two days of immersion in SBF. Unlike the gradual weight loss observed for the hybrid-derived glass SC-0, MS-0 showed a more rapid initial weight loss, potentially due to the higher reactivity of conventional chemicals. This higher reactivity is also reflected in the earlier formation of HAp

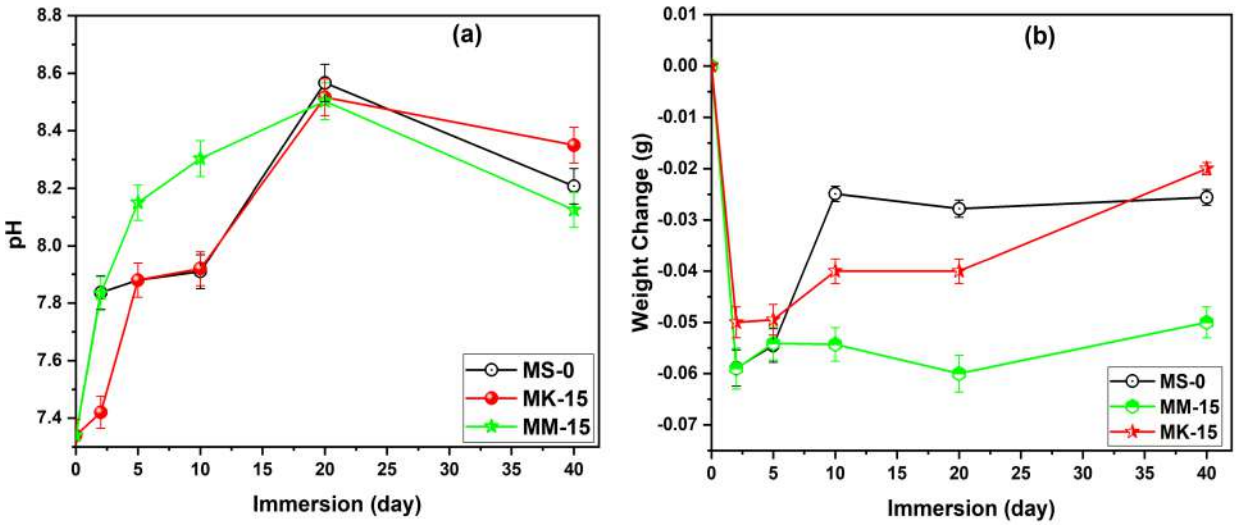

Figure 4.36: (a) pH and (b) weight change of conventional chemical derived glasses in SBF

observed in the XRD analysis of MS-0 (Section 4.3.10). Following the initial weight loss, MS-0 showed a weight gain throughout the immersion period, except for a slight weight fluctuations after 20 days of immersion. This fluctuation could be due to the formation of an intermediate phase formation, as observed in the XRD analysis. The weight change trend of MS-0 is consistent with its pH change profile as shown in **Fig. 4.36(a)**.

MM-15 showed a similar initial weight loss to its hybrid source derived glass, SCM-15. However, MM-15 exhibited higher weight gain after 5 days, possibly due to the increased reactivity of the conventional chemicals. Similar to SCM-15, the addition of MgO in MM-15 slow down the degradation rate, resulting in only marginal weight changes throughout the immersion period. This slower degradation correlates with the slower release of Si^{4+} observed in the MP-AES results for MM-15. The pH changes in the SBF solutions are non-uniform and consistent with the observed weight changes, reflecting alterations in the glass surface chemistry due to ion leaching and HAp formation, as discussed in Sections 4.1.8, and 4.2.8.

MK-15 exhibited a maximum weight loss of 5 wt% after 2 days, compared to 3.8 wt% for SNK-15 at the same time period. Like SNK-15, MK-15 showed a weight increase after 5 days, consistent with the formation of an intermediate phase observed in the XRD analysis. A slight weight loss at 10 days was

followed by relatively stable weight until 20 days of immersion, after which a continuous weight increase was observed up to 40 days. This behavior is more or less same as the trend observed for SNK-15. Overall, both MS-0 and MM-15 show different weight change profiles after 40 days compared to SC-0 and SCM-15, respectively. This suggests differences in the long-term stability of the HAp layer formed on the conventionally derived glasses with respect to the hybrid-derived glasses.

4.3.8 MP-AES analysis

MP-AES analysis was performed to quantify ion concentrations in SBF after immersing the MS-0, MM-15, and MK-15 glasses for 20 and 40 days. **Table 4.12** shows the concentrations of Si^{4+}, Ca^{2+}, Mg^{2+}, Na^{+}, and K^{+} in SBF, along with changes in Ca and P content (wt%) in the glasses before and after immersion, as determined by EDS analysis. The Ca/P molar ratios calculated from EDS data are also included.

Table 4.12: MP-AES analysis of ion concentrations (mg l^{-1}, n = 3) in SBF after 20 and 40 days. Changes in Ca and P content (wt%) and the Ca/P molar ratio before and after immersion for 20 and 40 days (mean ± standard deviation, n = 6) as determined by EDS are also presented.

(a) Ion concentrations in SBF

Sample	20 days					40 days				
Name	Si	Ca	Mg	K	Na	Si	Ca	Mg	K	Na
SBF	<1	16.4	37.4	257	3508	<1	16.4	37.4	257	3508
MS-0	97.5	29.9	34.7	239	3078	100	25.5	33.25	239	2478
MM-15	59.6	25.7	45.7	258	3708	41.2	25.5	43.9	261	4750
MK-15	63	50.2	35.94	373	3933	71.2	48.6	36	385	3783

(b) changes in Ca (wt%) and P (wt%) and Ca/P ratio determined from the EDS analysis for unsoaked and soaked glasses after 20 and 40 days

Sample	Unsoaked (0 days)		Soaked (20 days)			Soaked (40 days)		
Name	Ca	P	Ca	P	Ca/P	Ca	P	Ca/P
MS-0	19.5	2.7	15.2	2.9	5.2	16.2	6.6	2.4
MM-15	11.2	4	9.5	23.3	3.7	8.9	4.1	2.2
MK-15	22.3	2.0	16.6	3.7	4.5	17	3.7	4.5

MS-0 exhibited the highest Si^{4+} ion release compared to the other glasses, consistent with the trend observed in the hybrid-source-derived glasses. How-

ever, these conventionally prepared glasses showed less ion release in comparison to those of their hybrid source counterparts, possibly because of the more polymerized structure of the conventional glasses, as suggested by the density and FTIR analysis. Additionally, our earlier study revealed that eggshell-derived CaO exhibits a different conversion profile and higher porosity compared to conventional $CaCO_3$, potentially retaining some carbonate groups even at 1000 °C [58]. This difference in the CaO precursor may contribute to the higher ion leaching observed in the hybrid-source-derived glasses. Furthermore, the decrease in Si^{4+} release in the case of MM-15 glass indicates the slower Si^{4+} release, which may contribute to the more heterogeneous HAp layer formed on their surfaces, as shown in FE-SEM micrographs. Similarly, results have been observed in the case of MgO-substituted SCM-5, SCM-5,10, and SCM-15 glasses reported in the present study. The slower ion release might be the possible reason behind the continuous pH increase even after 20 days in the MM-15 glass, corresponding to the delayed but continuous ion exchange reaction between SBF and glasses. Furthermore, the MM-15 sample shows less leaching of the Mg^{2+} as compared to the SCM-15 glass, which might be the possible reason behind the better formation of the HAp layer as compared to the SCM-15 glass indicating higher release of Mg^{2+} in SCM-15 glass, as magnesium is highly reported to decrease the crystallization tendency of HAp layer [228]. However, the sodium ion leaching is non-uniform in all the glasses and higher as compared to the hybrid-soruce-derived glasses. The decrease in the leaching of Ca^{2+} in MS-0 and MM-15 glasses after 40 days is due to the formation of the HAp layer on the glass surface as observed in the EDS analysis of these glasses.

In MK-15 glass, the lower Ca^{2+} release could be the reason for the less dense HAp layer formed compared to SNK-15 glass. However, MK-15 glass indicates the release of higher amounts of the Ca^{2+} and other ions, except silica as compared to MS-0, and MM-15 glass, followed by a decrease in the Ca^{2+} in the solution after 40 days. Overall, the results indicate less Ca^{2+} and Si^{4+} ion release from the conventionally prepared glasses compared to the hybrid-source-derived glasses, which can be attributed to the high porosity of

the agro-food waste-derived glasses, as reported previously [71].

4.3.9 FE-SEM EDS analysis

FE-SEM analysis reveals appreciable changes on the glass surfaces after 20 and 40 days of SBF immersion (**Fig. 4.37**). After 20 days, all samples show non-uniform distribution of the HAp layer due to surface inhomogeneity. The HAp layer become homogeneous over time with increasing thickness of the layer. MS-0 and MM-15 exhibit small spherical crystals, more pronounced than those observed on SC-0 and SCM-15 glass. After 40 days, flaky structures appear on MS-0 and MM-15, indicating further layer growth. This enhanced HAp formation on the conventional chemicals-derived glasses could be due to faster ion exchange compared to the hybrid-source-derived glasses, potentially due to the less Mg^{2+} leaching (compared to SCM-15 glass), which is known to retard c-HAp crystallization. However, the EDS analysis indicates a higher Ca/P ratio (as shown in **Table 4.12**) as compared to the SC-0 and SCM-15 glass samples (Ca/P ratios of 4.1 and 1.6, respectively) after 20 days. The Ca/P ratios for MS-0 and MM-15 glass were approximately 2.45 and 2.20 after 40 days, indicating more stable layer formation compared to SC-0 and SCM-15, which showed dissolution after 20 days.

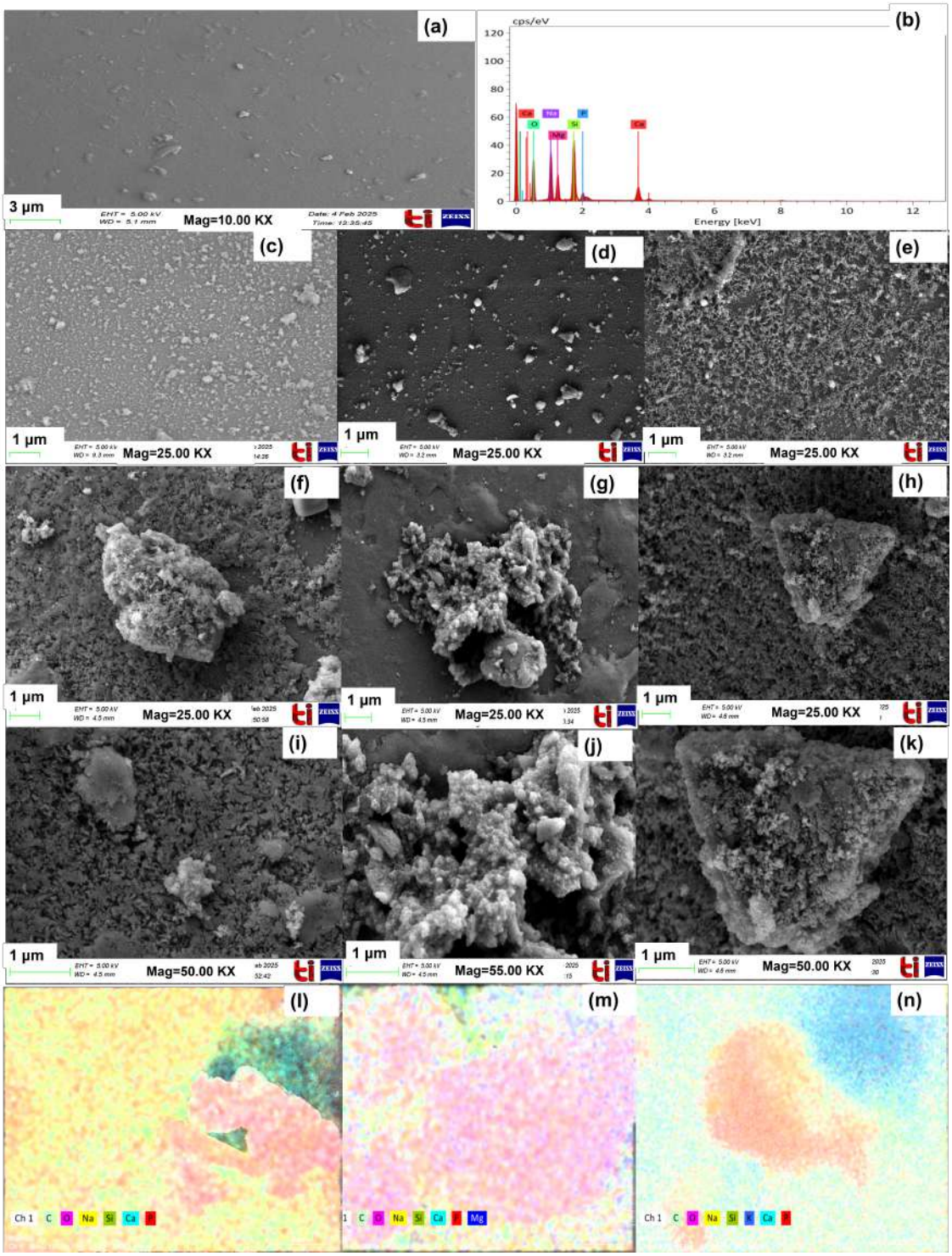

Figure 4.37: FE-SEM images and EDS analysis of glasses after SBF immersion: (a) Representative FE-SEM and (b) EDS analysis of MM-15 glass; (c, d, e) MS-0, MM-15, and MK-15 after 20 days at 25X; (f, g, h) MS-0, MM-15, MK-15 after 40 days at 25X; (i, j, k) MS-0, MM-15, MK-15 after 40 days at 50X; (l, m, n) EDS area mapping of MS-0, MM-15, and MK-15 after 40 days

For MK-15, FE-SEM micrographs reveal less spongy layer formation compared to SNK-15. This could be attributed to the reduced Ca^{2+} ion release

from MK-15, as observed in the MP-AES analysis. The reduced spongy layer formation, followed by the development of a flaky structure after 40 days of immersion, suggests less homogeneous HAp formation on MK-15 compared to SNK-15. This observation is further supported by the higher Ca/P ratio for MK-15.

4.3.10 XRD analysis

XRD patterns of the pristine and SBF-immersed glasses are shown in **Fig. 4.38**. After immersion, all glasses exhibit weak diffraction peaks corresponding to semi-crystalline hydroxyapatite (HAp) (ICDD card no. 01-072-1243), superimposed on the amorphous hump, as formation of HAp is a surface phenomenon [7]. In contrast to the hybrid-source-derived glasses, HAp peaks appear in MS-0 and MM-15 after just two days of immersion and remain stable up to 40 days, indicating more rapid and stable HAp layer formation.

In MS-0, weak peaks corresponding to tetracalcium phosphate (TTCP) (ICDD card no. 01-070-1379) are observed at 20 and 40 days immersion in SBF, appearing later than in SC-0, where TTCP is present at all immersion periods. This delayed TTCP formation in MS-0 might explain its higher Ca/P ratio after 20 and 40 days. MM-15, however, does not exhibit any peaks corresponding to the TTCP phase, likely due to its lower Ca^{2+} content, similar to the SCM-15 glass. Further, MK-15 shows fewer and weaker HAp peaks compared to SNK-15 glass, indicating delayed HAp formation than SNK-15 glass. This delay may be attributed to the reduced Ca^{2+} leaching observed in MP-AES analysis in MK-15 glass compared to SNK-15 glass.

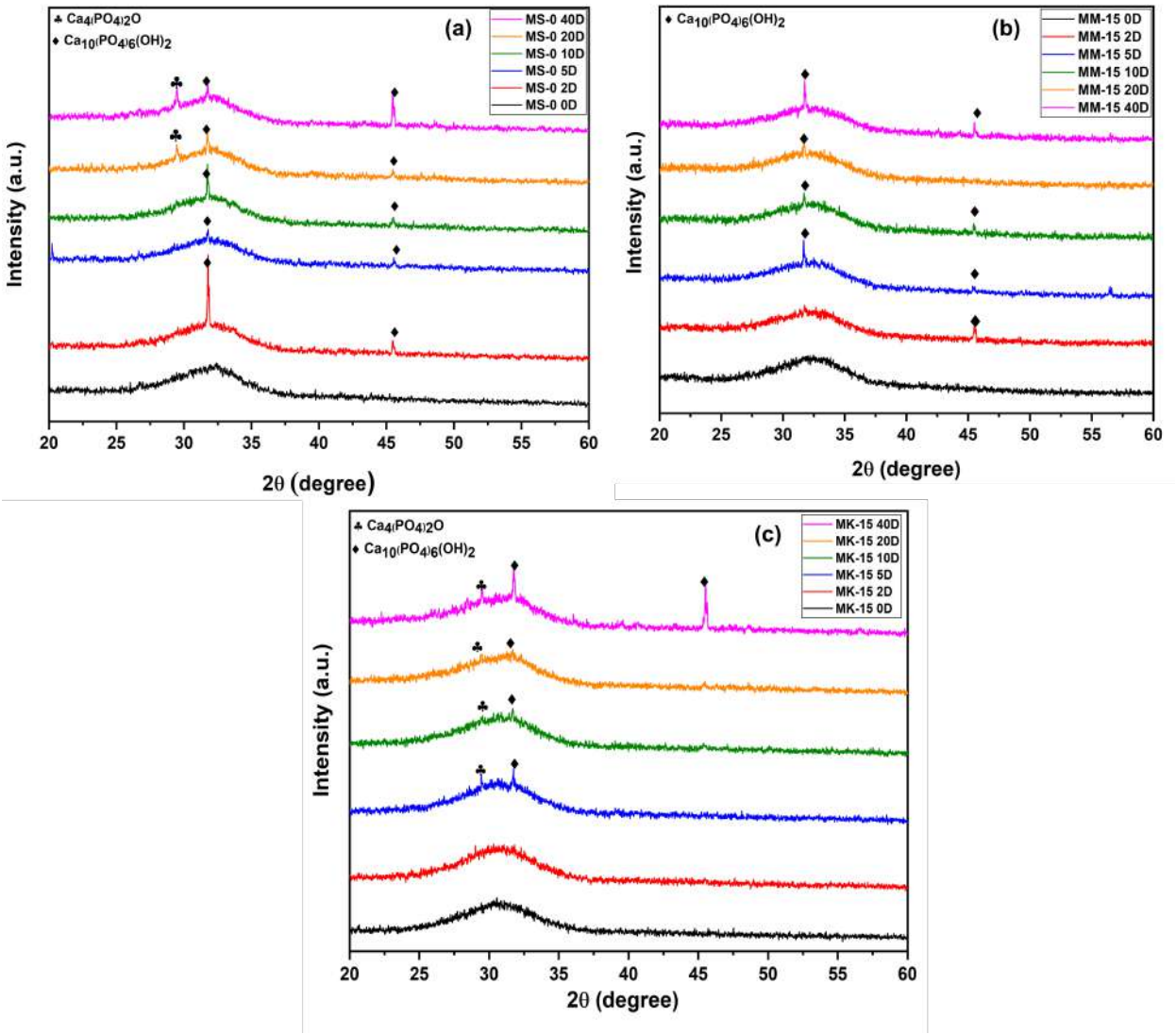

Figure 4.38: XRD patterns of pristine and SBF-immersed (a) MS-0, (b) MM-15, (c) MK-15 glasses for different time durations

4.3.11 FTIR analysis

FTIR spectra of the glasses after varying SBF immersion times (**Fig. 4.39**, FTIR spectra in the range from 4000-400 cm^{-1} is shown in Appendix **Fig. A4**) reveal changes in their structural composition. The increased FWHM observed for all glasses with increasing immersion time indicates an increased structural disorder. The intense Si-OH^- band at ∼1200 cm^{-1} and ∼1735 cm^{-1} is present in all glasses at different time intervals [236]. The prominent Si-O-Si stretching band at ∼910 cm^{-1} gradually merges with the phosphate band at ∼1025 cm^{-1} as immersion time increases [168][210].

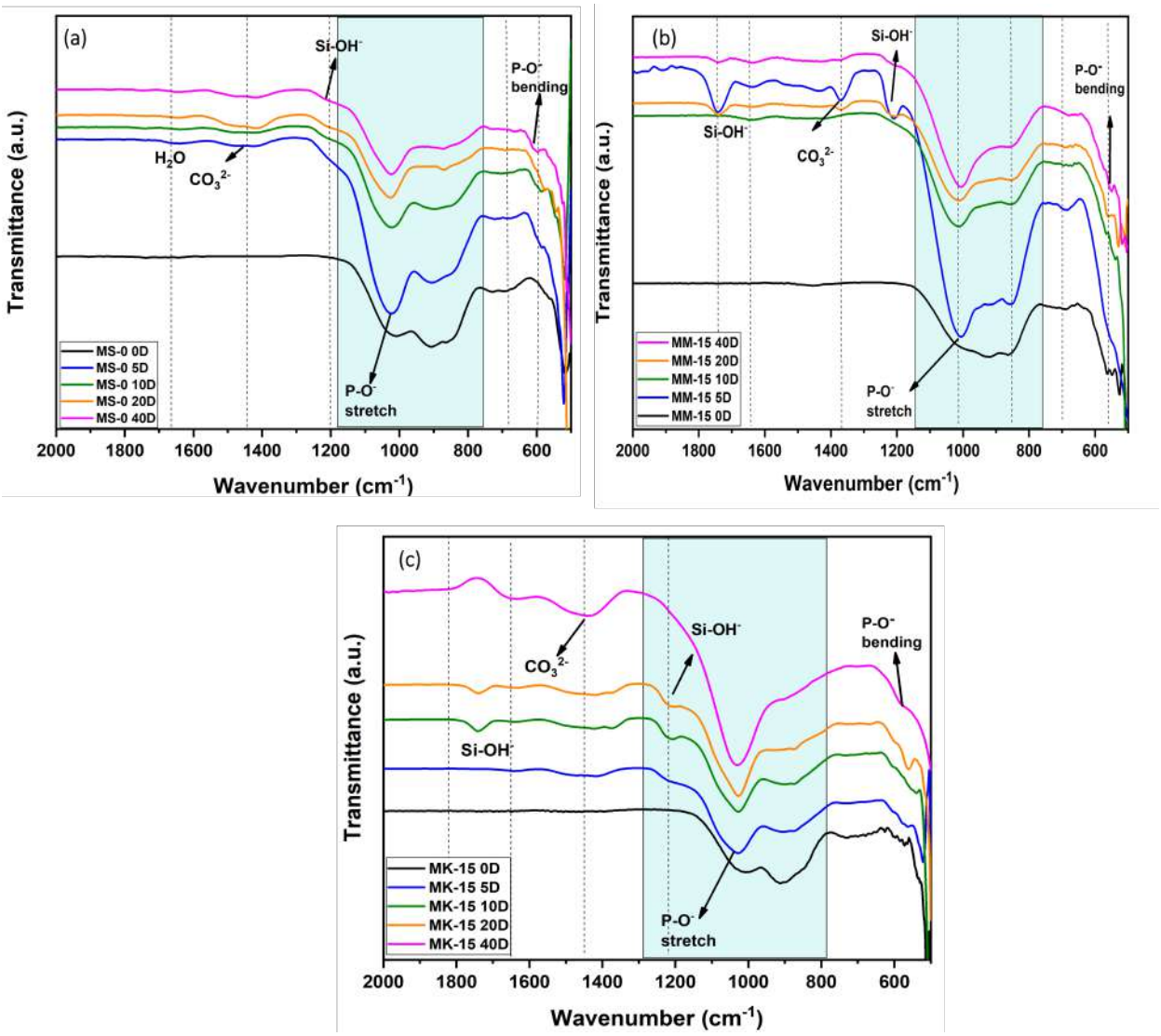

Figure 4.39: FTIR spectra of (a) MS-0, (b) MM-15, (c) MK-15 glasses after SBF immersion for different durations

MS-0 and MK-15 exhibit highly intense phosphate bands after 20 days of immersion, similar to SC-0 and SNK-15 samples, while MM-15 shows a slow and continuous increase in this band with increasing immersion time, followed by an intensified band corresponding to phosphate units after 40 days. The early formation of the silanol layer suggests it acts as a precursor to HAp formation. In the fingerprint region, all samples show similar behavior, with increased intensity of the P-O^{-} bending band at ∼587 cm^{-1} [222][227]. The band at 735 cm^{-1} gradually disappears with immersion time, suggesting increased disorder in the silicate structure. The pronounced CO_3^{2-} band at ∼1450 cm^{-1} confirms the formation of carbonated hydroxyapatite (c-HAp), consistent with the EDS

results [71][242]. Overall, the FTIR spectra confirm c-HAp formation on all glass surfaces with increasing immersion time. The most significant changes are observed in MS-0 and MK-15, potentially due to higher silica leaching compared to MM-15, resulting in a more intense Ca-P layer.

4.3.12 MTT assay

Fig. 4.40 shows the cell viability of the conventionally derived glasses (MS-0, MM-15, and MK-15) after 24 h of incubation with PBMCs at concentrations up to 200 μg/ml. In contrast to the hybrid-source-derived glasses, which maintained high viability even at 200 μg/ml, the conventional glasses exhibited a decrease in cell viability to ∼70% at just 50 μg/ml. This decrease might be attributed to the higher initial leaching of alkali ions (e.g., Na^+) from the conventional glasses, potentially causing a cytotoxic effect. High alkali ion release and its negative impact on cell viability have been reported in the literature [243][244][245].

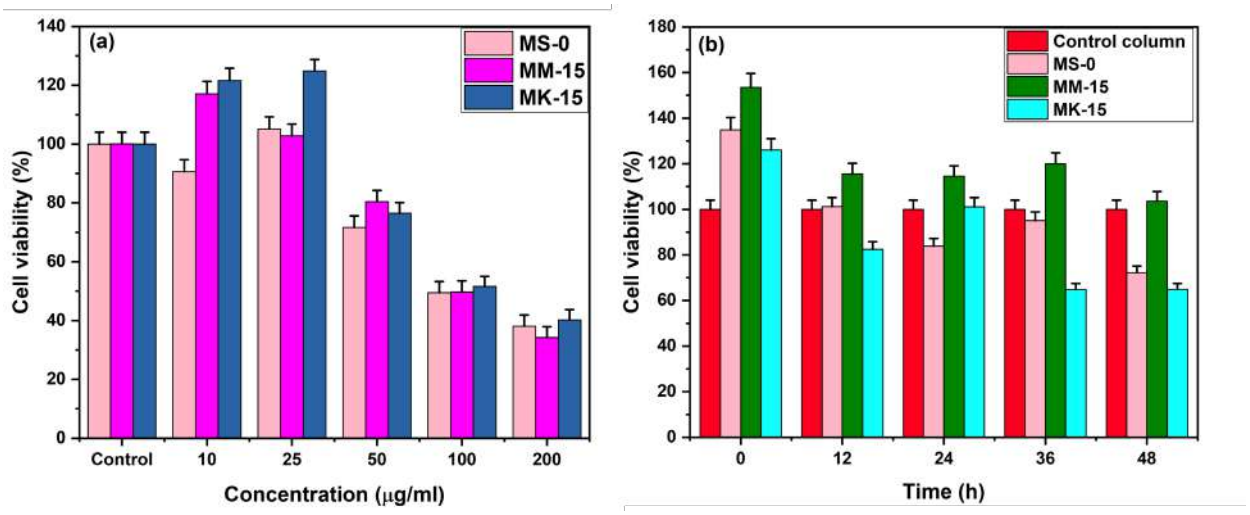

Figure 4.40: Cell growth effect of (a) Different concentrations of glasses on human PBMC cells (b) At different time intervals with constant concentration (25 µg/ml) of glasses. The figure represents the mean ± std. dev. of 3 different experiments and are significantly different at p-value < 0.05.

The faster ion release from the conventional glasses compared to the hybrid glasses could also contribute to this reduced cytocompatibility. Similar findings have been reported by Wallace *et al.* [246] and Tilocca [247], suggesting that a rapid release of alkali ions, rather than a balanced release of calcium (essential

for cell viability and interfacial bonding), can be detrimental. Due to the significant decrease in viability observed at 50 μg/ml, a lower concentration (25 μg/ml) was used for the time-dependent cell viability test (up to 48 h). All conventional glasses, except MK-15, maintained acceptable cell viability up to 48 h. MK-15 showed a decrease to 64% viability after 48 h. Overall, the hybrid-source derived glasses exhibited higher cell viability (>80%) as compared to their conventionally derived glasses.

4.4 Summary

This study investigated the effects of compositional modifications and precursor sources on bioactive glass properties. In the first series, the addition of MgO for CaO in 43SiO_2-25Na_2O- 7P_2O_5-(25-x)CaO-(x)MgO (x=0,5,10, and 15 wt%) resulted in increased phase separation compared to the base glass without the addition of MgO. On the other hand, substituting K_2O for Na_2O decreases the phase separation. Both MgO and K_2O additions were found to increase the glass sintering window (ΔT) and hardness, while simultaneously decreasing TEC relative to the base glass. The results consistently indicated non-linear trends, attributed to the mixed modifier effect, which also influenced the in-vitro bioactivity. In-vitro assessments revealed that MgO-containing glasses exhibited delayed crystalline c-HAp formation, resulting in a less stable HAp layer (Ca/P ratio of 1.63 after 20 days), but demonstrated better cytocompatibility with cell viability > 86%. K_2O-containing glasses showed faster and more stable c-HAp formation (Ca/P ratio of 2.2 after 40 days). However, their cytocompatibility was reduced over time as compared to MgO series glasses, likely due to higher rates of ion leaching. Compared to hybrid-source-derived glasses, conventional chemical-derived glasses exhibited better structural, thermal, and mechanical properties, including higher density and hardness. Furthermore, conventional chemical-derived glasses demonstrated faster and more stable c-HAp formation (Ca/P = 2.4–4.5 after 40 days) but reduced cell viability and increased cytotoxicity at higher concentrations. Among all the synthesized compositions, the comparison of the bioactive, mechanical, and thermal properties of the best-performing glasses with the commercial 45S5

bioglass is presented in **Table 4.13**.

Table 4.13: Comparison of bioactive, mechanical, and thermal properties of the glasses synthesized in the present work and 45S5 bioactive glass as reported in the literature.

Sample ID	**Cell viability (after 24 h)**	**Ca/P ratio (days)**	**Hardness (GPa)**	**Sintering window** ($\Delta T = T_c - T_g$)	**TEC** ($\times 10^{-6}\,^{\circ}\mathrm{C}^{-1}$)	**Ref.**
SC-0	$> 85\%$	4.1 (20 days)	4.6	149	15.8	[–]
SCM-15	$> 85\%$	1.6 (20 days)	6.1	230	10.5	[–]
SNK-15	$> 85\%$	2.2 (40 days)	6.0	165	12.0	[–]
MS-0	$< 80\%$	2.9 (20 days)	6.5	149	15.0	[–]
45S5 Bioglass	$> 85\%$	1.67 (21 days)	4.5	118	15.0	[18] [158] [217] [248]

Overall, the hybrid-source-derived glasses demonstrated better bioactive properties compared to those derived from conventional precursors. These findings underscore the significant impact of both the type of modifier oxide and the nature of the precursor source on the physicochemical properties and biological response of bioactive glasses. These insights are essential for the rational design of bioactive glasses tailored to specific biomedical applications.

CHAPTER 5

Conclusion and future scope

Conclusion

Two glass series, $43SiO_2$-$25Na_2O$-$7P_2O_5$-(25-x)CaO-xMgO (where x = 0, 5, 10, 15 wt%) and $43SiO_2$-$25CaO$-$7P_2O_5$-(25-y)Na_2O-yK_2O (where y = 0, 5, 10, 15 wt%), were synthesized via melt-quenching using hybrid sources, combining biowaste-derived SiO_2 and $CaCO_3$ with other conventional chemicals such as Na_2O, MgO, P_2O_5, and K_2O. These series were characterized to analyze the structural, thermal, and mechanical properties using various characterization techniques. Further, in-vitro bioactivity and biocompatibility assessments with human PBMCs were also conducted. For comparative analysis, three optimal compositions identified from the above compositions were also synthesized using exclusively conventional chemicals as a source. The compositions of these glasses are $43SiO_2$-$25CaO$-$25Na_2O$-$7P_2O_5$, $43SiO_2$-$10CaO$-$15MgO$-$25Na_2O$-$7P_2O_5$, and $43SiO_2$-$25CaO$-$10Na_2O$-$15K_2O$-$7P_2O_5$ are designated as MS-0, MM-15, and MK-15, respectively. The key conclusions drawn from the present study are as follows:

- All synthesized glasses were amorphous in nature, exhibiting a phase separation tendency. Further, MgO substitution in place of CaO increased this tendency, whereas K_2O in place of Na_2O reduced phase separation tendency.
- MgO exhibited a dual structural role, acting as a network former in the silicate glass network and a modifier in the phosphorus glass network, leading to an overall increase in glass network polymerization.
- K_2O addition increases the proportion of odd-numbered Q^3 and Q^1 structural units, overall promoting the conversion of some NBOs into BOs in this glass series.
- Both MgO and K_2O additions increase the glass sintering window (ΔT = 149-230 ^oC) and hardness (5.1-6.2 GPa) compared to the base glass (4.6 GPa). Simultaneously, MgO decreased the TEC, while K_2O increased it.

- The mixed-modifier effect was evident in both glass series, resulting in deviations from expected trends in different properties of these glasses and even in in-vitro bioactive properties.
- Regarding bioactivity, MgO addition retarded Si^{4+} ion release and delayed the formation of crystalline c-HAp during in-vitro testing in SBF.
- Conversely, K_2O addition increased overall ion leaching, which accelerated c-HAp formation. Consequently, K_2O-contained hybrid-source-derived glasses demonstrated higher bioactivity than MgO-containing glass series, primarily due to enhanced Ca^{2+} ion leaching and more open glass structure.
- Both MgO and K_2O series glasses exhibited good cytocompatibility (>85% cell viability) with PBMCs up to concentrations of 200 μg/ml.
- In comparison to hybrid-source-derived glasses, conventional chemical-derived glasses exhibited better physical, structural, and mechanical properties.
- Hybrid-source-derived glasses exhibit a more open glass structure as compared to the conventional chemical-derived glasses.
- Conventional chemical-derived glasses exhibited better c-HAp layer formation; however, the cell viability decreases in these glasses after a concentration of 50 μg/ml, exhibiting toxicity with higher concentrations.

The present glasses derived from hybrid sources exhibit good bioactivity and cytocompatibility, indicating their potential use in clinical applications such as tissue engineering and coatings for orthopedic and dental implants.

Future scope of the present work

Further research should investigate:

1. The present glasses require more extensive in-vitro as well as in-vivo testing, including cytotoxicity, cell adhesion, proliferation, osteogenetic differentiation, and therapeutic efficacy evaluations, to use them in real conditions.
2. The specific influence of two alkali modifiers in the (MgO, K_2O)-containing glasses warrants detailed investigation, particularly for potential dental filling applications.

3. The effect of heat-treatment on the bioactivity and biocompatibility can be explored.

4. This approach of utilizing hybrid sources (biowaste combined with conventional chemicals) offers a cost-effective and sustainable pathway to develop bioactive materials without hampering the other properties. Further research and development on other waste-derived sources, such as sugarcane bagasse ash and peanut shell ash, can be explored to develop environmentally friendly biomaterials.

References

[1] Larry L Hench. Biomaterials : a forecast for the future. *Biomaterials*, 19(16):1419–1423, 1998.

[2] Julian R Jones. Reprint of : Review of bioactive glass : From Hench to hybrids. *Acta Biomaterialia*, 23:S53–S82, 2015.

[3] Buddy D. Ratner, Allan S. Hoffman, Frederick J. Schoen, and Jack E. Lemons. *Biomaterials Science: An Introduction to Materials: Third Edition*. 2013.

[4] Mohamed N. Rahaman, Delbert E. Day, B. Sonny Bal, Qiang Fu, Steven B. Jung, Lynda F. Bonewald, and Antoni P. Tomsia. Bioactive glass in tissue engineering. *Acta Biomaterialia*, 7(6):2355–2373, 2011.

[5] Larry L. Hench, Ionnis D. Xynos, and Julia M. Polak. Bioactive glasses for in situ tissue regeneration. *Journal of Biomaterials Science, Polymer Edition*, 15(4):543–562, 2004.

[6] Gurbinder Kaur, Om P. Pandey, Kulvir Singh, Dan Homa, Brian Scott, and Gary Pickrell. A review of bioactive glasses: Their structure, properties, fabrication and apatite formation. *Journal of Biomedical Materials Research - Part A*, 102(1):254–274, 2014.

[7] Gurbinder Kaur. *Bioactive glasses - Potential Biomaterials for Future Therapy*. Springer International Publishing Switzerland 2017, 1 edition, 2017.

[8] Julian R. Jones. *Bioactive glasses*. Woodhead Publishing Limited, 2008.

[9] Brian Love. Polymeric Biomaterials. *Biomaterials*, pages 205–238, 1 2017.

[10] L. L. Hench, R. J. Splinter, W. C. Allen, and T. K. Greenlee. Bonding mechanisms at the interface of ceramic prosthetic materials. *Journal of Biomedical Materials Research*, 5(6):117–141, 1971.

[11] Kalpana S. Katti. Biomaterials in total joint replacement. *Colloids and Surfaces B: Biointerfaces*, 39(3):133–142, 12 2004.

[12] L.L. Hench and J. M. Polak. Third-Generation Biomedical Materials. *Science*, 295(5557):1012–1017, 2002.

[13] Mohammad M. Farag. Recent trends on biomaterials for tissue regeneration applications: review. *Journal of Materials Science*, 58(2):527–558, 1 2023.

[14] Enrico Ferrero, Ian Dunham, and Philippe Sanseau. In silico prediction of novel therapeutic targets using gene-disease association data. *Journal of Translational Medicine*, 15(182), 8 2017.

[15] S. Inayat-Hussain, N. F. Rajab, and E. L. Siew. In vitro testing of biomaterials toxicity and biocompatibility. In *Cellular Response to Biomaterials*, pages 508–537. Elsevier Ltd., 2008.

[16] Eva Jablonská, Jiří Kubásek, Dalibor Vojtěch, Tomáš Ruml, and Jan Lipov. Test conditions can significantly affect the results of in vitro cytotoxicity testing of degradable metallic biomaterials. *Scientific Reports*, 11(1), 12 2021.

[17] Tadashi Kokubo. Bioactive glass ceramics: properties and applications. *Biomaterials*, 12(2):155–163, 1991.

[18] Tadashi Kokubo and Hiroaki Takadama. How useful is SBF in predicting in vivo bone bioactivity? *Biomaterials*, 27(15):2907–2915, 2006.

[19] Ayako Oyane, Hyun-Min Kim, Takuo Furuya, Tadashi Kokubo, Toshiki Miyazaki, and Takashi Nakamura. Preparation and assessment of revised simulated body fluids. *Journal of biomedical materials research. Part A*, 65(2):188–195, 2003.

[20] Cuilian Wen, Nuonan Bai, Lijin Luo, Jianxia Ye, Xuan Zhan, and Yinggan Zhang. Structural behavior and in vitro bioactivity evaluation of hydroxyapatite-like bioactive glass based on the SiO 2 -CaO-P 2 O 5 system. *Ceramics International*, 47(13):18094–18104, 2021.

[21] Delia S. Brauer, Natalia Karpukhina, Matthew D. O'Donnell, Robert V. Law, and Robert G. Hill. Fluoride-containing bioactive glasses: Effect of glass design and structure on degradation, pH and apatite formation in simulated body fluid. *Acta Biomaterialia*, 6(8):3275–3282, 2010.

[22] Ishu Kansal, Dilshat U. Tulyaganov, Ashutosh Goel, Maria J. Pascual, and José M.F. Ferreira. Structural analysis and thermal behavior of diopside-fluorapatite- wollastonite-based glasses and glass-ceramics. *Acta Biomaterialia*, 6(11):4380–4388, 2010.

[23] M. Karanjai, B. V.Manoj Kumar, R. Sundaresan, B. Basu, T. R. Rama Mohan, and B. P. Kashyap. Fretting wear study on Ti–Ca–P biocomposite in dry and simulated body fluid. *Materials Science and Engineering: A*, 475(1-2):299–307, 2 2008.

[24] James M. Anderson. Future challenges in the in vitro and in vivo evaluation of biomaterial biocompatibility, 4 2016.

[25] Julian R. Jones. Review of bioactive glass: From Hench to hybrids. *Acta Biomaterialia*, 9(1):4457–4486, 2013.

[26] J. M. Anderson. Biocompatibility. In *Polymer Science: A Comprehensive Reference*, volume 9, pages 363–383. Elsevier, 2012.

[27] Larry L Hench. Bioceramics: from concept to clinic. J Am Ceram Soc. 1993;72:93-98. *Journal of the American Ceramic Society*, 74:1487–1510, 1991.

[28] Makato Ogino, Fumio Ohuchi, and L. L. Hench. Compositional dependence of the formation of calcium phosphate films on bioglass. *Journal of Biomedical Materials Research*, 14(1):55–64, 1980.

[29] I. Atkinson, E. M. Anghel, L. Predoana, O. C. Mocioiu, L. Jecu, I. Raut, C. Munteanu, D. Culita, and M. Zaharescu. Influence of ZnO addition on the structural, in vitro behavior and antimicrobial activity of sol–gel derived CaO–P2O5–SiO2 bioactive glasses. *Ceramics International*, 42(2):3033–3045, 2016.

[30] Francesco Baino, Sepideh Hamzehlou, and Saeid Kargozar. Bioactive glasses: Where are we and where are we going? *Journal of Functional Biomaterials*, 9(1), 2018.

[31] Eva Jablonská, Diana Horkavcová, Dana Rohanová, and Delia S. Brauer. A review of: In vitro cell culture testing methods for bioactive glasses and other biomaterials for hard tissue regeneration, 12 2020.

[32] Jinyan Li, Dong Zhai, Fang Lv, Qingqing Yu, Hongshi Ma, Jinbo Yin, Zhengfang Yi, Mingyao Liu, Jiang Chang, and Chengtie Wu. Preparation of copper-containing bioactive glass/eggshell membrane nanocomposites for improving angiogenesis, antibacterial activity and wound healing. *Acta Biomaterialia*, 36:254–266, 5 2016.

[33] Larry L Hench. Bioactive Ceramics. *Annals of the New York Academy of Sciences*, 523(1):54–71, 1988.

[34] Valentina Miguez-Pacheco, Larry L. Hench, and Aldo R. Boccaccini. Bioactive glasses beyond bone and teeth: Emerging applications in contact with soft tissues. *Acta Biomaterialia*, 13:1–15, 2015.

[35] Larry L. Hench. The story of Bioglass®. *Journal of Materials Science: Materials in Medicine*, 17(11):967–978, 2006.

[36] Nazanin Jafari, Mina Seyed Habashi, Alireza Hashemi, Reza Shirazi, Nader Tanideh, and Amin Tamadon. Application of bioactive glasses in various dental fields. *Biomaterials Research*, 26(1):1–15, 2022.

[37] Larry L Hench. Genetic design of bioactive glass. *Journal of the European Ceramic Society*, 29(7):1257–1265, 2009.

[38] Xin Liu, Mohamed N. Rahaman, and Qiang Fu. Bone regeneration in strong porous bioactive glass (13-93) scaffolds with an oriented microstructure implanted in rat calvarial defects. *Acta Biomaterialia*, 9(1):4889–4898, 2013.

[39] M. D. O'Donnell and R. G. Hill. Influence of strontium and the importance of glass chemistry and structure when designing bioactive glasses for bone regeneration. *Acta Biomaterialia*, 6(7):2382–2385, 2010.

[40] T. De Caluwé, C. W.J. Vercruysse, H. A. Declercq, D. Schaubroeck, R. M.H. Verbeeck, and L. C. Martens. Bioactivity and biocompatibility of two fluoride containing bioactive glasses for dental applications. *Dental Materials*, 32(11):1414–1428, 11 2016.

[41] Joyce Rodrigues de Souza, Elisa Camargo Kukulka, Vêronica Ribeiro dos Santos, Letícia Terumi Kito, Eliandra de Sousa Trichês, Gilmar Patrocínio Thim, Alexandre Luiz Souto Borges, and Tiago Moreira Bastos Campos. Enhancing bone regeneration: Exploring the potential of silicate chlorinated bioactive glasses and dehydration mechanisms. *Journal of Non-Crystalline Solids*, 631:122912, 5 2024.

[42] Hans Erling Skallevold, Dinesh Rokaya, Zohaib Khurshid, and Muhammad Sohail Zafar. Bioactive glass applications in dentistry, 12 2019.

[43] Mani Diba, Felipe Tapia, Aldo R. Boccaccini, and Leonie A. Strobel. Magnesium-Containing Bioactive Glasses for Biomedical Applications. *International Journal of Applied Glass Science*, 3(3):221–253, 2012.

[44] Duygu Ege, Kai Zheng, and Aldo R. Boccaccini. Borate Bioactive Glasses (BBG): Bone Regeneration, Wound Healing Applications, and Future Directions. *ACS Applied Bio Materials*, 5(8):3608–3622, 2022.

[45] Melissa Tiskaya, David Gillam, Saroash Shahid, and Robert Hill. A potassium based fluorine containing bioactive glass for use as a desensitizing toothpaste. *Molecules*, 26(14), 7 2021.

[46] Raika Brückner, Maxi Tylkowski, Leena Hupa, and Delia S. Brauer. Controlling the ion release from mixed alkali bioactive glasses by varying modifier ionic radii and molar volume. *Journal of Materials Chemistry B*, 4(18):3121–3134, 2016.

[47] Margit Fabian, Matthew Krzystyniak, Atul Khanna, and Zsolt Kovacs. Structural and Dynamical Effects of the CaO/SrO Substitution in Bioactive Glasses. *Molecules*, 29(19), 10 2024.

[48] Ilaria Cacciotti. Bivalent cationic ions doped bioactive glasses: the influence of magnesium, zinc, strontium and copper on the physical and biological properties. *Journal of Materials Science*, 52(15):8812–8831, 8 2017.

[49] Mónica Duque-Acevedo, Luis J. Belmonte-Ureña, Francisco Joaquín Cortés-García, and Francisco Camacho-Ferre. Agricultural waste: Review of the evolution, approaches and perspectives on alternative uses. *Global Ecology and Conservation*, 22(e00902), 6 2020.

[50] Hossein Moayedi, Babak Aghel, Mu'azu Mohammed Abdullahi, Hoang Nguyen, and Ahmad Safuan A Rashid. Applications of rice husk ash as green and sustainable biomass. *Journal of Cleaner Production*, 237, 11 2019.

[51] S. Bhuvaneshwari, Hiroshan Hettiarachchi, and Jay N. Meegoda. Crop residue burning in India: Policy challenges and potential solutions. *International Journal of Environmental Research and Public Health*, 16(5), 3 2019.

[52] Gaurav Sharma, Manmeet Kaur, Shivani Punj, and Kulvir Singh. Biomass as a sustainable resource for value-added modern materials: a review. *Biofuels, Bioproducts and Biorefining*, 14(3):673–695, 2020.

[53] X. F. Lou and J. Nair. The impact of landfilling and composting on greenhouse gas emissions - A review. *Bioresource Technology*, 100(16):3792–3798, 8 2009.

[54] S. K.S. Hossain, Lakshya Mathur, and P. K. Roy. Rice husk/rice husk ash as an alternative source of silica in ceramics: A review. *Journal of Asian Ceramic Societies*, 6(4):299–313, 2018.

[55] I. A. Cornejo, S. Ramalingam, J. S. Fish, and I. E. Reimanis. Hidden treasures: Turning food waste into glass. *American Ceramic Society Bulletin*, 93(6):24–27, 2014.

[56] Miao Deng, Guoyong Zhang, Yu Zeng, Xiangjun Pei, Runqiu Huang, and Jinhui Lin. Simple process for synthesis of layered sodium silicates using rice husk ash as silica source. *Journal of Alloys and Compounds*, 683:412–417, 10 2016.

[57] Fabio Seigi Murakami, Patrik Oening Rodrigues, Célia Maria Teixeira De Campos, and Marcos Antônio Segatto Silva. Physicochemical study of CaCO3 from egg shells. *Ciencia e Tecnologia de Alimentos*, 27(3):658–662, 2007.

[58] Navneet Kaur and K. Singh. Decompositional and chemical reaction kinetics study of eggshell powder waste for value-added materials. *Journal of Thermal Analysis and Calorimetry*, 148(13):6451–6463, 7 2023.

[59] Aman Bhardwaj, S. K.S. Hossain, and Manas R. Majhi. Preparación y caracterización de sílice refractaria de alta resistencia unida a arcilla utilizando residuos agrícolas. *Boletin de la Sociedad Espanola de Ceramica y Vidrio*, 56(6):256–262, 11 2017.

[60] S. K.S. Hossain, Lakshya Mathur, and P. K. Roy. Rice husk/rice husk ash as an alternative source of silica in ceramics: A review. *Journal of Asian Ceramic Societies*, 6(4):299–313, 10 2018.

[61] Shivani Punj, Neha Srivastava, Manoj Baranwal, and Kulvir Singh. In-vitro biological evaluation of diopside bio-ceramic synthesized from sustainable agro-food waste ashes. *silicon*, 2021.

[62] Gaurav Sharma. *Structural , physical and optical properties of rice husk*

ash derived glass / ceramics. PhD thesis, Thapar Institute of Engineering and Technology, Patiala, 7 2013.

[63] Wilaiwan Leenakul, Tawee Tunkasiri, Natee Tongsiri, Kamonpan Pengpat, and Jetsada Ruangsuriya. Effect of sintering temperature variations on fabrication of 45S5 bioactive glass-ceramics using rice husk as a source for silica. *Materials Science and Engineering C*, 61:695–704, 4 2016.

[64] Gaurav Sharma and K. Singh. Dielectric and optical properties of glasses and glass-ceramics synthesized from agro-food wastes. *Materials Chemistry and Physics*, 246(122754):0254–0584, 2020.

[65] Satwinder Singh Danewalia, Gaurav Sharma, Samita Thakur, and K. Singh. Agricultural wastes as a resource of raw materials for developing low-dielectric glass-ceramics. *Scientific Reports*, 6:1–12, 2016.

[66] Shiow Yi Chen, Po Fong Chou, Wai Kong Chan, and Hsiu Mei Lin. Preparation and characterization of mesoporous bioactive glass from agricultural waste rice husk for targeted anticancer drug delivery. *Ceramics International*, 43(2):2239–2245, 2017.

[67] Farnaz Naghizadeh, Mohammed Rafiq Abdul Kadir, Ali Doostmohammadi, Fatemeh Roozbahani, Nida Iqbal, Mohammad Mahdi Taheri, Sangeetha Vasudevaraj Naveen, and Tunku Kamarul. Rice husk derived bioactive glass-ceramic as a functional bioceramic: Synthesis, characterization and biological testing. *Journal of Non-Crystalline Solids*, 427:54–61, 2015.

[68] S. Sasikumar and R. Vijayaraghavan. Low temperature synthesis of nanocrystalline hydroxyapatite from egg shells by combustion method. *Trends in Biomaterials and Artificial Organs*, 19(2):70–73, 2006.

[69] Samina Ahmed and Mainul Ahsan. Synthesis of Ca-hydroxyapatite Bioceramic from Egg Shell and its Characterization. *Bangladesh Journal of Scientific and Industrial Research*, 43(4):501–512, 1970.

[70] Manmeet Kaur Chhina and K. Singh. Samarium doped calcium silicate derived from agro-food wastes and their structural, optical and luminescent properties. *Ceramics International*, 47(15):0272–8842, 2021.

[71] Shivani Punj and Kulvir Singh. Bioactive calcium silicate glass synthesized from sustainable biomass wastes. *Biofuels, Bioproducts and Biorefining*, 14(6):1141–1151, 2020.

[72] Povinder K. Mehta. US4105459, 1978.

[73] Iara J. Fernandes, Daiane Calheiro, Amanda G. Kieling, Carlos A.M. Moraes, Tatiana L.A.C. Rocha, Feliciane A. Brehm, and Regina C.E. Modolo. Characterization of rice husk ash produced using different biomass combustion techniques for energy. *Fuel*, 165:351–359, 2 2016.

[74] Iara J. Fernandes, Felipe A.L. Sánchez, José R. Jurado, Amanda G. Kieling, Tatiana L.A.C. Rocha, Carlos A.M. Moraes, and Vânia C. Sousa. Physical, chemical and electric characterization of thermally treated rice husk ash and its potential application as ceramic raw material. *Advanced Powder Technology*, 28(4):1228–1236, 4 2017.

[75] M. Nehdi, J. Duquette, and A. El Damatty. Performance of rice husk ash produced using a new technology as a mineral admixture in concrete. *Cement and Concrete Research*, 33(8):1203–1210, 8 2003.

[76] N. Yalçin and V. Sevinç. Studies on silica obtained from rice husk. *Ceramics International*, 27(2):219–224, 2001.

[77] Concha Real, María D Alcalá, and José M Criado. Preparation of Silica from Rice Husks. *Journal of the American Ceramic Society*, 79(8):2012–2016, 1996.

[78] Pallavi Deshmukh, Jatin Bhatt, Dilip Peshwe, and Shailkumar Pathak. Determination of silica activity index and XRD, SEM and EDS studies of amorphous SiO 2 extracted from rice Husk Ash. *Transactions of the Indian Institute of Metals*, 65(1):63–70, 2 2012.

[79] Donanta Dhaneswara, Jaka Fajar Fatriansyah, Frans Wensten Situmorang, and Alfina Nurul Haqoh. Synthesis of Amorphous Silica from Rice Husk Ash: Comparing HCl and CH3COOH Acidification Methods and Various Alkaline Concentrations. *International Journal of Technology*, 11(1):200–208, 1 2020.

[80] N. Tangboriboon, R. Kunanuruksapong, A. Sirivat, R. Kunanuruksapong, and A. Sirivat. Preparation and properties of calcium oxide from eggshells via calcination. *Materials Science- Poland*, 30(4):313–322, 2012.

[81] Z. Goudarzi, N. Parvin, and Fariborz Sharifianjazi. Formation of hydroxyapatite on surface of SiO2– P2O5–CaO–SrO–ZnO bioactive glass synthesized through sol-gel route. *Ceramics International*, 45(15):19323–19330, 10 2019.

[82] Shiva Naseri, William C. Lepry, and Showan N. Nazhat. Bioactive glasses in wound healing: Hope or hype? *Journal of Materials Chemistry B*, 5(31):6167–6174, 2017.

[83] Jyoti Prakash Nayak and Japes Bera. Bioactive porous silica ceramics prepared using rice husk ash by gelcasting method. *Advanced Materials Research*, 548:12–16, 2012.

[84] Hamisah Ismail and Hasmaliza Mohamad. Bioactivity and biocompatibility properties of sustainable wollastonite bioceramics from rice husk ash/rice straw ash: A review, 9 2021.

[85] J. P. Nayak, S. Kumar, and J. Bera. Sol-gel synthesis of bioglass-ceramics using rice husk ash as a source for silica and its characterization. *Journal of Non-Crystalline Solids*, 356(28-30):1447–1451, 6 2010.

[86] M. A. Pereira, J. E. de Oliveira, and C. S. Fonseca. Influence of the use of rice husk as source of silica on the sol-gel synthesis of bioglass. *Ceramica*, 67(383):333–337, 7 2021.

[87] A. Ratep. Preparation and Characterization of Silicate Glasses from Waste Agriculture Materials (Rice Husk and Peanut Peel). *Silicon*, 12(6):1425–1432, 2020.

[88] Sevil Yücel, Zeynep Aydın Sinirlioğlu, Burcu Karakuzu, Tülay Merve Temel, Yeliz Elalmış, and Ali Can Özarslan. Production, Characterization and Bioactivity of 46S6 Bioactive Glass from Rice Hull Ash Silica. *Advanced Materials Research*, 1120-1121:857–861, 2015.

[89] Sevil Yücel, Pınar Terzioğlu, Zeynep Aydin Sinirlioğlu, Bilge Sema Tekerek, and Yeliz Başaran Elalmiş. Synthesis, characterization, In vitro degradability and bioactivity of strontium substituted rice hull ash silica based melt derived 45S5 bioactive glass. *Journal of Engineering and Natural Sciences*, 383(212):23–32, 2015.

[90] Ali Can Özarslan and Sevil Yücel. Fabrication and characterization of strontium incorporated 3-D bioactive glass scaffolds for bone tissue from biosilica. *Materials Science and Engineering C*, 68:350–357, 2016.

[91] Burcu Karakuzu-Ikizler, Pınar Terzioğlu, Yeliz Basaran-Elalmis, Bilge Sema Tekerek, and Sevil Yücel. Role of magnesium and aluminum substitution on the structural properties and bioactivity of bioglasses synthesized from biogenic silica. *Bioactive Materials*, 5(1):66–73, 2020.

[92] Maziar Montazerian, Adam Shearer, and John C. Mauro. Perspectives on the impact of crystallization in bioactive glasses and glass-ceramics. *International Journal of Ceramic Engineering and Science*, 6(1), 1 2024.

[93] Hugo R. Fernandes, Anuraag Gaddam, Avito Rebelo, Daniela Brazete, George E. Stan, and José M.F. Ferreira. Bioactive glasses and glass-ceramics for healthcare applications in bone regeneration and tissue engineering. *Materials*, 11(12), 12 2018.

[94] Oscar Peitl, Edgar Dutra Zanotto, and Larry L. Hench. Highly bioactive P2O5-Na2O-CaO-SiO2glass-ceramics. *Journal of Non-Crystalline Solids*, 292(1-3):115–126, 2001.

[95] Francesco Baino. Bioactive glasses – When glass science and technology meet regenerative medicine. *Ceramics International*, 44(13):14953–14966, 2018.

[96] Alireza Zandi Karimi, Ehsan Rezabeigi, and Robin A.L. Drew. Crystallization behavior of combeite in 45S5 Bioglass® via controlled heat treatment. *Journal of Non-Crystalline Solids*, 502:176–183, 12 2018.

[97] Zhi Wei Loh, Mohd Hafiz Mohd Zaid, Khamirul Amin Matori, Wei Mun Cheong, Mohd Zul Hilmi Mayzan, and Rosdiyana Hisam. Synthesis of novel CaF2 CaO Na2O B2O3SiO2 bioglass system: phase transformation, surface reaction and mechanical properties. *Applied Physics A: Materials Science and Processing*, 130(6), 6 2024.

[98] Oscar Peitl Filho, Guy P Latorre, and Larry L Hench. Effect of crystallization on apatite-layer formation of bioactive glass 45 S5. *Journal of Biomedical Materials Research*, 30:509–514, 1996.

[99] Renato Luiz Siqueira and Edgar Dutra Zanotto. The influence of phosphorus precursors on the synthesis and bioactivity of SiO2-CaO-P2O5 sol-gel glasses and glass-ceramics. *Journal of Materials Science: Materials in Medicine*, 24(2):365–379, 2 2013.

[100] Roslinda Shamsudin, Farah 'Atiqah Abdul Azam, Muhammad Azmi Abdul Hamid, and Hamisah Ismail. Bioactivity and cell compatibility of β-wollastonite derived from rice husk ash and limestone. *Materials*, 10(10), 10 2017.

[101] Md Monirujjaman, Satish Jain, Sushil Patel, Simon Hasan, Locherla Daloji, Raghavendra Gujjala, Abdul Azeem P, and Syam Prasad P. Investigating the Mechanical and Tribological Properties of Bio-Waste Derived Bioactive Borosilicate Glass Incorporating Strontium Oxide. *Journal of Engineering and Science in Medical Diagnostics and Therapy*, 2024.

[102] Shivani Punj and K. Singh. Blue-green light emitting inherent luminescent glasses synthesized from agro-food wastes. *Journal of Materials Science: Materials in Electronics*, 30(4):3871–3881, 2019.

[103] Srinath Palakurthy, K Venugopal Reddy, Sushil Patel, and P Abdul Azeem. A cost effective SiO 2 – CaO – Na 2 O bio - glass derived from bio - waste resources for biomedical applications. *Progress in Biomaterials*, 9(4):239–248, 2020.

[104] Maroua H. Kaou, Csaba Balázsi, and Katalin Balázsi. Structural and Morphological Investigation of Calcium-Silicate-Based Bioceramics Prepared from Eggshell via Conventional Approach. *Inorganics*, 13(2), 2 2025.

[105] Rajan Choudhary, Sivasankar Koppala, and Sasikumar Swamiappan. Bioactivity studies of calcium magnesium silicate prepared from eggshell waste by sol-gel combustion synthesis. *Journal of Asian Ceramic Societies*, 3(2):173–177, 6 2015.

[106] Lunguo Xia, Zhilan Yin, Lixia Mao, Xiuhui Wang, Jiaqiang Liu, Xinquan Jiang, Zhiyuan Zhang, Kaili Lin, Jiang Chang, and Bing Fang. Akermanite bioceramics promote osteogenesis, angiogenesis and suppress osteoclastogenesis for osteoporotic bone regeneration. *Scientific Reports*, 6, 2 2016.

[107] Amirhossein Kazemi, Majid Abdellahi, Armina Khajeh-Sharafabadi, Amirsalar Khandan, and Neriman Ozada. Study of in vitro bioactivity and mechanical properties of diopside nano-bioceramic synthesized by a facile method using eggshell as raw material. *Materials Science and Engineering C*, 71:604–610, 2017.

[108] Rajan Choudhary, Sivasankar Koppala, Aviral Srivastava, and Swamiappan Sasikumar. In-vitro bioactivity of nanocrystalline and bulk larnite/chitosan composites: comparative study. *Journal of Sol-Gel Science and Technology*, 74(3):631–640, 6 2015.

[109] Palakurthy Srinath, P. Abdul Azeem, K. Venugopal Reddy, Padala Chiranjeevi, Manavathi Bramanandam, and Rayavarapu Prasada Rao. A novel cost-effective approach to fabricate diopside bioceramics: A promis-

ing ceramics for orthopedic applications. *Advanced Powder Technology*, 32(3):875–884, 3 2021.

[110] Rajan Choudhary, Senthil Kumar Venkatraman, Inna Bulygina, Fedor Senatov, Sergey Kaloshkin, Natalya Anisimova, Mikhail Kiselevskiy, Marina Knyazeva, Dimitri Kukui, Frank Walther, and Sasikumar Swamiappan. Biomineralization, dissolution and cellular studies of silicate bioceramics prepared from eggshell and rice husk. *Materials Science and Engineering C*, 118, 1 2021.

[111] SK S. Hossain, Sushma Yadav, Shreyasi Majumdar, S. Krishnamurthy, Ram Pyare, and P. K. Roy. A comparative study of physico-mechanical, bioactivity and hemolysis properties of pseudo-wollastonite and wollastonite glass-ceramic synthesized from solid wastes. *Ceramics International*, 46(1):833–843, 1 2020.

[112] Zhi Wei Loh, Mohd Hafiz Mohd Zaid, Khamirul Amin Matori, Mohd Mustafa Awang Kechik, Yap Wing Fen, Mohd Zul Hilmi Mayzan, Shahira Liza, and Wei Mun Cheong. Phase transformation and mechanical properties of new bioactive glass-ceramics derived from CaO–P2O5–Na2O–B2O3–SiO2 glass system. *Journal of the Mechanical Behavior of Biomedical Materials*, 143:105889, 7 2023.

[113] F. Andreola, M. I. Martín, A. M. Ferrari, I. Lancellotti, F. Bondioli, J. Ma Rincón, M. Romero, and L. Barbieri. Technological properties of glass-ceramic tiles obtained using rice husk ash as silica precursor. *Ceramics International*, 39(5):5427–5435, 7 2013.

[114] Farnaz Naghizadeh, Naznin Sultana, Mohammed Rafiq Abdul Kadir, Tengku Muzaffar Tengku Md Shihabudin, Rafaqat Hussain, and Tunku Kamarul. The fabrication and characterization of PCL/rice husk derived bioactive glass-ceramic composite scaffolds. *Journal of Nanomaterials*, 2014, 2014.

[115] S. Vichaphund, M. Kitiwan, D. Atong, and P. Thavorniti. Microwave

synthesis of wollastonite powder from eggshells. *Journal of the European Ceramic Society*, 31(14):2435–2440, 11 2011.

[116] A. Siddharthan, T. S. Sampath Kumar, and S. K. Seshadri. Synthesis and characterization of nanocrystalline apatites from eggshells at different Ca/P ratios. *Biomedical Materials*, 4(4), 2009.

[117] M. Sirait, K. Sinulingga, N. Siregar, and R. S.D. Siregar. Synthesis of hydroxyapatite from limestone by using precipitation method. In *Journal of Physics: Conference Series*, volume 1462. Institute of Physics Publishing, 3 2020.

[118] Ana Zastulka, Simona Clichici, Maria Tomoaia-Cotisel, Aurora Mocanu, Cecilia Roman, Cristian Doru Olteanu, Bogdan Culic, and Teodora Mocan. Recent Trends in Hydroxyapatite Supplementation for Osteoregenerative Purposes. *Materials*, 16(3), 2 2023.

[119] Shih Ching Wu, Hsi Kai Tsou, Hsueh Chuan Hsu, Shih Kuang Hsu, Shu Ping Liou, and Wen Fu Ho. A hydrothermal synthesis of eggshell and fruit waste extract to produce nanosized hydroxyapatite. *Ceramics International*, 39(7):8183–8188, 9 2013.

[120] E. Landi, G. Celotti, G. Logroscino, and A. Tampieri. Carbonated hydroxyapatite as bone substitute. *Journal of the European Ceramic Society*, 23(15):2931–2937, 2003.

[121] Samina Ahmed and Mainul Ahsan. Synthesis of Ca-hydroxyapatite Bioceramic from Egg Shell and its Characterization. *Bangladesh J. Sci. Ind. Res*, 43(4):501–512, 2008.

[122] S. Salman, O. Gunduz, S. Yilmaz, M. L. Öveçoğlu, Robert L. Snyder, S. Agathopoulos, and F. N. Oktar. Sintering effect on mechanical properties of composites of natural hydroxyapatites and titanium. *Ceramics International*, 35(7):2965–2971, 9 2009.

[123] S. Daglilar, M. E. Erkan, O. Gunduz, L. S. Ozyegin, S. Salman, S. Agath-

opoulos, and F. N. Oktar. Water resistance of bone-cements reinforced with bioceramics. *Materials Letters*, 61(11-12):2295–2298, 5 2007.

[124] M Sivakumar, T S Sampath Kumart, K L Shantha, and K Panduranga Rao. Development of hydroxyapatite derived fkom Indian coral. *Biomateriols*, 17:1709–1714, 1996.

[125] Shih Ching Wu, Hsueh Chuan Hsu, Shih Kuang Hsu, Chien Pei Tseng, and Wen Fu Ho. Effects of calcination on synthesis of hydroxyapatite derived from oyster shell powders. *Journal of the Australian Ceramic Society*, 55(4):1051–1058, 2019.

[126] Mohamed Saiful Firdaus Hussin, Hasan Zuhudi Abdullah, Maizlinda Izwana Idris, and Mohd Arizam Abdul Wahap. Extraction of natural hydroxyapatite for biomedical applications—A review. *Heliyon*, 8(8), 8 2022.

[127] J Hu, J J Russell, B Ben-Nissan, and R Vago. Production and analysis of hydroxyapatite from Australian corals via hydrothermal process. *Journal of materials science letters*, 20:85–87, 2001.

[128] Jin Woo Park, Sang Ryul Bae, Jo Young Suh, Dong Hee Lee, Sang Hyun Kim, Hyungjun Kim, and Chong Soo Lee. Evaluation of bone healing with eggshell-derived bone graft substitutes in rat calvaria: A pilot study. *Journal of Biomedical Materials Research - Part A*, 87(1):203–214, 10 2008.

[129] Eric M. Rivera, Miguel Araiza, Witold Brostow, Victor M. Castaño, J. R. Díaz-Estrada, R. Hernández, and J. Rogelio Rodríguez. Synthesis of hydroxyapatite from eggshells. *Materials Letters*, 41(3):128–134, 1999.

[130] Samina Ahmed and Mainul Ahsan. Synthesis of Ca-hydroxyapatite Bioceramic from Egg Shell and its Characterization. *Bangladesh J. Sci. Ind. Res*, 43(4):501–512, 2008.

[131] D. Siva Rama Krishna, A. Siddharthan, S. K. Seshadri, and T. S. Sampath Kumar. A novel route for synthesis of nanocrystalline hydroxya-

patite from eggshell waste. *Journal of Materials Science: Materials in Medicine*, 18(9):1735–1743, 2007.

[132] Cristina Rodica Dumitrescu, Ionela Andreea Neacsu, Vasile Adrian Surdu, Adrian Ionut Nicoara, Cosmin Iulian Codrea, Cristian-Emilian Pop, Roxana Trusca, and Ecaterina Andronescu. Maturation of hydroxyapatite from biogenic calcium source-a comparative study. *Bull., Series B*, 84(1):2022.

[133] N. A.S. Mohd Pu'ad, P. Koshy, H. Z. Abdullah, M. I. Idris, and T. C. Lee. Syntheses of hydroxyapatite from natural sources. *Heliyon*, 5(5), 5 2019.

[134] Dinesh K. Patel, Bin Jin, Sayan Deb Dutta, and Ki Taek Lim. Osteogenic potential of human mesenchymal stem cells on eggshells-derived hydroxyapatite nanoparticles for tissue engineering. *Journal of Biomedical Materials Research - Part B Applied Biomaterials*, 108(5):1953–1960, 7 2020.

[135] Sazia Sultana, Md Sahadat Hossain, Monika Mahmud, Mashrafi Bin Mobarak, Md Humayun Kabir, Nahid Sharmin, and Samina Ahmed. UV-assisted synthesis of hydroxyapatite from eggshells at ambient temperature: cytotoxicity, drug delivery and bioactivity. *RSC Advances*, 11(6):3686–3694, 1 2021.

[136] G. Ciobanu and M. Harja. Investigation on hydroxyapatite coatings formation on titanium surface. *IOP Conference Series: Materials Science and Engineering*, 444(3), 2018.

[137] A. A. Hamidi, M. N. Salimi, and A. H.M. Yusoff. Synthesis and characterization of eggshell-derived hydroxyapatite via mechanochemical method: A comparative study. *AIP Conference Proceedings*, 1835(iv):1–12, 2017.

[138] Himanshu Khandelwal and Satya Prakash. Synthesis and Characterization of Hydroxyapatite Powder by Eggshell. *Journal of Minerals and Materials Characterization and Engineering*, 04(02):119–126, 2016.

[139] Zaid Kareem and Ersan Eyiler. Synthesis of hydroxyapatite from eggshells via wet chemical precipitation: a review. *RSC Advances*, 14(30):21439–21452, 7 2024.

[140] Pilomeena Arokiasamy, Mohd Mustafa Al Bakri Abdullah, Shayfull Zamree Abd Rahim, Salmabanu Luhar, Andrei Victor Sandu, Noorina Hidayu Jamil, and Marcin Nabiałek. Synthesis methods of hydroxyapatite from natural sources: A review. *Ceramics International*, 48(11):14959–14979, 6 2022.

[141] S. Ramesh, A. N. Natasha, C. Y. Tan, L. T. Bang, S. Ramesh, C. Y. Ching, and Hari Chandran. Direct conversion of eggshell to hydroxyapatite ceramic by a sintering method. *Ceramics International*, 42(6):7824–7829, 5 2016.

[142] Wen Fu Ho, Hsueh Chuan Hsu, Shih Kuang Hsu, Chun Wei Hung, and Shih Ching Wu. Calcium phosphate bioceramics synthesized from eggshell powders through a solid state reaction. *Ceramics International*, 39(6):6467–6473, 8 2013.

[143] Rachele Sergi, Devis Bellucci, and Valeria Cannillo. A comprehensive review of bioactive glass coatings: State of the art, challenges and future perspectives. *Coatings*, 10(8), 8 2020.

[144] M. D. O'Donnell, P. L. Candarlioglu, C. A. Miller, E. Gentleman, and M. M. Stevens. Materials characterisation and cytotoxic assessment of strontium- substituted bioactive glasses for bone regeneration. *Journal of Materials Chemistry*, 20(40):8934–8941, 2010.

[145] Gurbinder Kaur, O. P. Pandey, and K. Singh. Glass Stability and Effect of Heat-Treatment Duration on Chemical Interaction between Calcium Lanthanum Borosilicate Glass Sealant and Electrolytes. *Journal of The Electrochemical Society*, 159(11):F717–F724, 2012.

[146] D. Bellucci, V. Cannillo, and A. Sola. Coefficient of thermal expansion of bioactive glasses: Available literature data and analytical equation estimates. *Ceramics International*, 37(8):2963–2972, 2011.

[147] Zdeněk Strnad. Role of the glass phase in bioactive glass-ceramics. *Biomaterials*, 13(5):317–321, 1992.

[148] Rees D. Rawlings. Bioactive glasses and glass-ceramics. *Clinical Materials*, 14(2):155–179, 1993.

[149] R. Hill. An alternative view of the degradation of bioglass. *Journal of Materials Science Letters*, 15(13):1122–1125, 1996.

[150] Marina T. Souza, Murilo C. Crovace, Cornelia Schröder, Hellmut Eckert, Oscar Peitl, and Edgar D. Zanotto. Effect of magnesium ion incorporation on the thermal stability, dissolution behavior and bioactivity in Bioglass-derived glasses. *Journal of Non-Crystalline Solids*, 382:57–65, 2013.

[151] Vrushali Pawar and Vaibhav Shinde. Bioglass and hybrid bioactive material: A review on the fabrication, therapeutic potential and applications in wound healing. *Hybrid Advances*, 6:100196, 8 2024.

[152] Michael Heiden Emily Walker. Magnesium, Iron and Zinc Alloys, the Trifecta of Bioresorbable Orthopaedic and Vascular Implantation - A Review. *Journal of Biotechnology & Biomaterials*, 05(02), 2015.

[153] J. Ma, C. Z. Chen, D. G. Wang, Y. Jiao, and J. Z. Shi. Effect of magnesia on the degradability and bioactivity of sol-gel derived SiO2-CaO-MgO-P2O5 system glasses. *Colloids and Surfaces B: Biointerfaces*, 81(1):87–95, 2010.

[154] Muhammad Shoaib, Ali Bahadur, Shahid Iqbal, Murefah Mana AL-Anazy, A. Laref, Muhammad Asif Tahir, Pervaiz Ali Channar, Saima Noreen, Muhammad Yasir, Amer Iqbal, and Khawaja Waqar Ali. Magnesium doped mesoporous bioactive glass nanoparticles: A promising material for apatite formation and mitomycin c delivery to the MG-63 cancer cells. *Journal of Alloys and Compounds*, 866:159013, 2021.

[155] A. Balamurugan, G. Balossier, J. Michel, S. Kannan, H. Benhayoune, A. H.S. Rebelo, and J. M.F. Ferreira. Sol gel derived SiO2-CaO-MgO-P2O5 bioglass system-preparation and in vitro characterization. *Jour-*

nal of Biomedical Materials Research - Part B Applied Biomaterials, 83(2):546–553, 11 2007.

[156] Ahmed Al-Noaman, Simon C.F. Rawlinson, and Robert G. Hill. The role of MgO on thermal properties, structure and bioactivity of bioactive glass coating for dental implants. *Journal of Non-Crystalline Solids*, 358(22):3019–3027, 2012.

[157] R. Wetzel, O. Bartzok, and D. S. Brauer. Influence of low amounts of zinc or magnesium substitution on ion release and apatite formation of Bioglass 45S5. *Journal of Materials Science: Materials in Medicine*, 31(10), 2020.

[158] R. Wetzel, M. Blochberger, F. Scheffler, L. Hupa, and Delia S. Brauer. Mg or Zn for Ca substitution improves the sintering of bioglass 45S5. *Scientific Reports*, 10(1):1–10, 2020.

[159] Elisa Fiume, Dilshat U. Tulyaganov, Avzal Akbarov, Nigora Ziyadullaeva, Andrea Cochis, Alessandro C. Scalia, Lia Rimondini, Enrica Verné, and Francesco Baino. Biological evaluation of a new sodium-potassium silico-phosphate glass for bone regeneration: In vitro and in vivo studies. *Materials*, 14(16), 8 2021.

[160] Elisa Fiume, Dilshat Tulyaganov, Graziano Ubertalli, Enrica Verné, and Francesco Baino. Dolomite-foamed bioactive silicate scaffolds for bone tissue repair. *Materials*, 13(3), 2 2020.

[161] Praveen Jha and K. Singh. Effect of MgO on bioactivity, hardness, structural and optical properties of SiO2–K2O–CaO–MgO glasses. *Ceramics International*, 42(1):436–444, 2016.

[162] M. Tylkowski and D. S. Brauer. Mixed alkali effects in Bioglass® 45S5. *Journal of Non-Crystalline Solids*, 376:175–181, 2013.

[163] V Cannillo and A Sola. Potassium-based composition for a bioactive glass. *Ceramics International*, 35:3389–3393, 2009.

[164] Murilo C. Crovace, Viviane O. Soares, Ana Candida M. Rodrigues, Oscar Peitl, Larissa M.S.C. Raucci, Paulo T. de Oliveira, and Edgar D. Zanotto. Understanding the mixed alkali effect on the sinterability and in vitro performance of bioactive glasses. *Journal of the European Ceramic Society*, 41(7):4391–4405, 2021.

[165] Polina Sinitsyna, Markus Engblom, and Leena Hupa. Impact of substituting K2O for Na2O on physico-chemical properties and in vitro bioactivity of bioactive glass S53P4. *Open Ceramics*, 16, 12 2023.

[166] Rehana Zia, Madeeha Riaz, Iqra Hameed, and Ayesha Afifa. The effect of K2O on the microstructure of Na2O-CaO-P2O5-SiO2 based ceramic system. *Optik - International Journal for Light and Electron Optics*, 2016.

[167] WEIJIA LI, JING ZHOU, and YUYIN XU. Study of the in vitro cytotoxicity testing of medical devices. *Biomedical Reports*, 3(5):617–620, 2015.

[168] Shivani Punj, Navneet Kaur Mattu, Kulvir Singh, and Manoj Baranwal. In-vitro and thermal stability study of bioglass synthesized from biogenic sources. *Ceramics International*, 2024.

[169] Jegan Athinarayanan, Vaiyapuri Subbarayan Periasamy, Mohammad Alhazmi, and Ali A. Alshatwi. Synthesis and biocompatibility assessment of sugarcane bagasse-derived biogenic silica nanoparticles for biomedical applications. *Journal of Biomedical Materials Research - Part B Applied Biomaterials*, 105(2):340–349, 2 2017.

[170] Saeid Kargozar, Peiman Brouki Milan, Moein Amoupour, Farzad Kermani, Sara Gorgani, Simin Nazarnezhad, Sara Hooshmand, and Francesco Baino. Osteogenic Potential of Magnesium (Mg)-Doped Multicomponent Bioactive Glass: In Vitro and In Vivo Animal Studies. *Materials*, 15(1):1–16, 2022.

[171] Muhammad Shoaib, Aamer Saeed, Javeed Akhtar, Muhammad Saif Ur Rahman, Aman Ullah, Klaus Jurkschat, and Muhammad Moazzam

Naseer. Potassium-doped mesoporous bioactive glass: Synthesis, characterization and evaluation of biomedical properties. *Materials Science and Engineering C*, 75:836–844, 6 2017.

[172] Dinesh K. Patel, Min Hyeok Kim, and Ki Taek Lim. Synthesis and Characterization of Eggshell-Derived Hydroxyapatite Bioceramics. *Journal of Biosystems Engineering*, 44(2):128–133, 6 2019.

[173] Damandeep Kaur, M. S. Reddy, and O. P. Pandey. In-vitro bioactivity of silicate-phosphate glasses using agriculture biomass silica. *Journal of Materials Science: Materials in Medicine*, 31(8), 2020.

[174] Mukta Rajotia, Pragya Pragya, Prakhar Bajpai, Anjali Upadhyay, Sudip Mukherjee, and Subrata Panda. Fabrication of Rice-Husk-Derived Silica Mediated Bioactive Glass for Antibacterial and Wound Healing Applications. *ACS Sustainable Resource Management*, 2(2):362–373, 2 2025.

[175] Sushil Patel, Raj Kumar Samudrala, Srinath Palakurthy, Bramanandam Manavathi, Raghavendra Gujjala, and Abdul Azeem P. In vitro evaluation and mechanical studies of MgO added borophosphate glasses for biomedical applications. *Ceramics International*, 48(9):12625–12634, 5 2022.

[176] Zakaria Tabia, Khalil El Mabrouk, Meriame Bricha, and Khalid Nouneh. Mesoporous bioactive glass nanoparticles doped with magnesium: Drug delivery and acellular: In vitro bioactivity. *RSC Advances*, 9(22):12232–12246, 2019.

[177] Cristina Daniela Ghiţulică, Andrada Ioana Damian-Buda, Andreia Cucuruz, and Georgeta Voicu. Synthesis and characterization of zno(Mgo)-caosio2-p2o5 bioglass obtained by sol-gel method in presence of surfactant agent. *Gels*, 7(4), 12 2021.

[178] Laís D. Silva, Fernanda C. Puosso, Viviane O. Soares, Oscar Peitl Filho, Simone do R.F. Sabino, Francisco C. Serbena, Murilo C. Crovace, and Edgar D. Zanotto. Two-step sinter-crystallization of

K2O–CaO–P2O5–SiO2 (45S5-K) bioactive glass. *Ceramics International*, 47(13):18720–18731, 7 2021.

[179] L L Hench and H A Paschall. Direct Chemical Bond of Bioactive Glass-Ceramic Materials to Bone and Muscle. *J. BIOMED. MATER. RES. SYMPOSIUM*, (4):25–42, 1973.

[180] Gigliola Lusvardi, Gianluca Malavasi, Ledi Menabue, M. Cristina Menziani, Alfonso Pedone, and Ulderico Segre. Density of multicomponent silica-based potential bioglasses: Quantitative structure-property relationships (QSPR) analysis. *Journal of the European Ceramic Society*, 27(2-3):499–504, 2007.

[181] Bernard Dennis Cullity and SR Stock. *Elements of X-ray diffraction*. Assison-Wesley publishing company, USA, 2" edition edition, 1978.

[182] Mitang Wang, Long Fang, Mei Li, Zhaogang Liu, Yanhong Hu, Xiaowei Zhang, Wei Deng, and Ruhil Dongol. Phase separation and crystallization of La2O3 doped ZnO-B2O3-SiO2 glass. *Journal of Rare Earths*, 37(7):767–772, 2019.

[183] James E Shelby. *Introduction to Glass Science and Technology*. The Royal Society of Chemistry, 1 2005.

[184] Elton N. Kaufmann. *Characterization of Materials*, volume 1 and 2. WILEY-INTERSCIENCE A john Wiley and Sons Publication, 2003.

[185] A. Alyamani and O. M. FE-SEM Characterization of Some Nanomaterial. In *Scanning Electron Microscopy*. InTech, 3 2012.

[186] Raghvendra Kumar Mishra, Sabu Thomas, and Ajesh K. Zachariah. Energy-Dispersive X-ray Spectroscopy Techniques for Nanomaterial. *Microscopy Methods in Nanomaterials Characterization*, pages 383–405, 1 2017.

[187] Brian C. Smith. *Fundamentals of fourier transform infrared spectroscopy, second edition*. 2011.

[188] Barbara H. Stuart. *Infrared and Raman Spectroscopy - Methods and Applications*. 2004.

[189] Oscar Peitl, Edgar Dutra, and Larry L Hench. Highly bioactive P 2 O 5 ± Na 2 O ± CaO ± SiO 2 glass-ceramics. *Journal of Non-Crystalline Solids*, 292:115–126, 2001.

[190] Punnama Siriphannon, Yoshikazu Kameshima, Atsuo Yasumori, Kiyoshi Okada, and Shigeo Hayashi. Influence of preparation conditions on the microstructure and bioactivity of-CaSiO 3 ceramics: Formation of hydroxyapatite in simulated body fluid. *Journal of biomedical materials research*, 52(1):30–39, 2000.

[191] V. Balaram. Microwave plasma atomic emission spectrometry (MP-AES) and its applications – A critical review. *Microchemical Journal*, 159:105483, 12 2020.

[192] Priyankar Dey, Nisha Tewari, Somit Dutta, Robert A. Newman, and Tapas Kumar Chaudhuri. Oleander attenuates hepatic inflammation in a TLR4-independent manner and by favorable modulation of hepatocellular global metabolome that supports cytoprotection. *Journal of Ethnopharmacology*, 323:117717, 4 2024.

[193] Gaurav Sharma and K. Singh. Agro-waste ash and mineral oxides derived glass-ceramics and their interconnect study with Crofer 22 APU for SOFC application. *Ceramics International*, 45(16):20501–20508, 11 2019.

[194] S. J. Watts, R. G. Hill, M. D. O'Donnell, and R. V. Law. Influence of magnesia on the structure and properties of bioactive glasses. *Journal of Non-Crystalline Solids*, 356(9-10):517–524, 2010.

[195] Praveen Jha and K. Singh. Effect of Field Strength and Electronegativity of CaO and MgO on Structural and Optical Properties of SiO2–K2O-CaO-MgO Glasses. *Silicon*, 8(3):437–442, 2016.

[196] Harisankar Sreenivasan, Paivo Kinnunen, Elijah Adesanya, Minna Patanen, Anu M. Kantola, Ville Veikko Telkki, Marko Huttula, Wei Cao,

John L. Provis, and Mirja Illikainen. Field Strength of Network-Modifying Cation Dictates the Structure of (Na-Mg) Aluminosilicate Glasses. *Frontiers in Materials*, 7(August):1–13, 2020.

[197] Adam Shearer, Matthew Molinaro, Maziar Montazerian, Jessica J. Sly, Marta Miola, Francesco Baino, and John C. Mauro. The unexplored role of alkali and alkaline earth elements (ALAEs) on the structure, processing, and biological effects of bioactive glasses. *Biomaterials Science*, 2024.

[198] Hongshen Liu, Andrew L. Ogrinc, Yinan Lin, Collin Wilkinson, Karan Doss, Aubrey L. Fry, Conghang Qu, Hongtu He, Timothy M. Gross, Nicholas J. Smith, John C. Mauro, and Seong H. Kim. Mixed modifier effects on structural, mechanical, chemical, and mechanochemical properties of sodium calcium aluminosilicate glass. *Journal of the American Ceramic Society*, 106(11):6541–6554, 11 2023.

[199] Kristin Griebenow, Caio Barca Bragatto, Efstratios I. Kamitsos, and Lothar Wondraczek. Mixed-modifier effect in alkaline earth metaphosphate glasses. *Journal of Non-Crystalline Solids*, 481:447–456, 2 2018.

[200] Hao Liu, Randall E. Youngman, Saurabh Kapoor, Lars R. Jensen, Morten M. Smedskjaer, and Yuanzheng Yue. Nano-phase separation and structural ordering in silica-rich mixed network former glasses. *Physical Chemistry Chemical Physics*, 20(23):15707–15717, 2018.

[201] Junjie Zhao, Xiuxia Xu, Xiaotong Chen, Qian Xu, Zhou Luo, Xvsheng Qiao, Jincheng Du, Xianping Fan, and Guodong Qian. A structure model for phase separated fluoroaluminosilicate glass system by molecular dynamic simulations. *Journal of the European Ceramic Society*, 39(15):5018–5029, 2019.

[202] Armando Mandlule, Franziska Döhler, Leo Van Wüllen, Toshihiro Kasuga, and Delia S. Brauer. Changes in structure and thermal properties with phosphate content of ternary calcium sodium phosphate glasses. *Journal of Non-Crystalline Solids*, 392-393:31–38, 6 2014.

[203] Refka Oueslati-Omrani, Ahmed Hichem Hamzaoui, Radhouane Chtourou, and Adel M'nif. Structural, thermal and optical properties of phosphate glasses doped with SiO2. *Journal of Non-Crystalline Solids*, 481:10–16, 2 2018.

[204] B. Bochentyn, A. Warych, N. Szreder, A. Mielewczyk-Gryń, J. Karczewski, M. Prześniak-Welenc, M. Gazda, and B. Kusz. Characterization of structural, thermal and mechanical properties of bismuth silicate glasses. *Journal of Non-Crystalline Solids*, 439:51–56, 5 2016.

[205] Francesco Gerardo Mecca, Devis Bellucci, and Valeria Cannillo. Effect of Thermal Treatments and Ion Substitution on Sintering and Crystallization of Bioactive Glasses: A Review. *Materials*, 16(13), 7 2023.

[206] R. Wetzel, O. Bartzok, L. Hupa, and D. S. Brauer. Low Mg or Zn substitution for improved thermal properties of Bioglass 45S5. *Materials Letters*, 256, 12 2019.

[207] Praveen Jha, S. S. Danewalia, and K. Singh. Influence of thermal stability on dielectric properties of SiO2–K2O–CaO–MgO glasses. *Journal of Thermal Analysis and Calorimetry*, 128(2):745–754, 2017.

[208] Ulrich Lohbauer. Dental glass ionomer cements as permanent filling materials? -Properties, limitations and future trends. *Materials*, 3(1):76–96, 2010.

[209] M R Majhi, Ram Pyare, and S P Singh. Studies on preparation and characterizations of CaO-Na2O-SiO2-P2O5 bioglass ceramics substituted with Li2O , K2O , ZnO , MgO , and B2O3. *International Journal of Scientific & Engineering Research*, 2(9):1–9, 2011.

[210] Mirosław Handke, Włodzimierz Mozgawa, and Marek Nocuń. Specific features of the IR spectra of silicate glasses. *Journal of Molecular Structure*, 325(C):129–136, 1994.

[211] Damandeep Kaur, M. S. Reddy, and O. P. Pandey. Synthesis, characterization, drug loading and in-vitro bioactivity studies of rice husk derived

SiO2–P2O5–MgO–CaO–SrO bio-active glasses. *Journal of Drug Delivery Science and Technology*, 61(October):102154, 2021.

[212] Rasha A. Youness, Mohammed Said Amer, and Mohammed A. Taha. Comprehensive In Vivo and In Vitro Studies for Evaluating the Bone-Bonding Ability of Na2O–CaO–SiO2–B2O3–Ag2O Glasses for Fracture Healing Applications. *Journal of Inorganic and Organometallic Polymers and Materials*, 2023.

[213] Jianchao Lu, Zhitao Shan, Jun Zhang, Yucai Su, Kangfeng Yi, Yanfei Zhang, and Qiuju Zheng. Mechanical properties of mixed modified oxide glasses. *Journal of Non-Crystalline Solids: X*, 16:100125, 2022.

[214] Asma M Alturki, Ayshah S Alatawi, Dalia E Abulyazied, H M Abomostafa, G M El komy, R Alamlah, Mohammed A Taha, and Rasha A Youness. Magnetic and Dielectric Properties of Hybrid Nanocomposites of Biologically Extracted Hydroxyapatite/Hematite/Silicon Dioxide for Potential Use in Bone Replacement Applications. *ECS Journal of Solid State Science and Technology*, 12(8):83001, 8 2023.

[215] A. K. Seal, P. Chakraborti, Nihar Ranjon Roy, S. Mukherjee, M. K. Mitra, and G. C. Das. Effect of phase separation on the fracture toughness of SiO 2-B2O3-Na2O glass. *Bulletin of Materials Science*, 28(5):457–460, 2005.

[216] Gurbinder Kaur, Vishal Kumar, Francesco Baino, John C. Mauro, Gary Pickrell, Iain Evans, and Oana Bretcanu. Mechanical properties of bioactive glasses, ceramics, glass-ceramics and composites: State-of-the-art review and future challenges. *Materials Science and Engineering C*, 104(December 2018):109895, 2019.

[217] I. D. Thompson and L. L. Hench. Mechanical properties of bioactive glasses, glass-ceramics and composites. *Proceedings of the Institution of Mechanical Engineers, Part H: Journal of Engineering in Medicine*, 212(2):127–136, 1998.

[218] Xuewu Zhan, Xiaopeng Wu, Yiqiang Xing, Xinghui Cui, Shijie Wang, Fei Zhao, Wei Meng, Chengliang Ma, and Xiangchong Zhong. Improved hydration resistance of MgO-2CaO•SiO2-3CaO•SiO2composite refractory using low-grade minerals. *Materials Research Express*, 7(8), 8 2020.

[219] V. Lalzawmliana, Akrity Anand, Vinod Kumar, Piyali Das, K. Bavya Devi, Jayanta Mukherjee, Asit Kumar Maji, Biswanath Kundu, Mangal Roy, and Samit Kumar Nandi. Potential of growth factor incorporated mesoporous bioactive glass for in vivo bone regeneration. *Journal of the Mechanical Behavior of Biomedical Materials*, 91:182–192, 2019.

[220] Ahmed Sleibi, A. R. Tappuni, Natalia G. Karpukhina, Robert G. Hill, and A. Baysan. A comparative evaluation of ion release characteristics of three different dental varnishes containing fluoride either with CPP-ACP or bioactive glass. *Dental Materials*, 35(12):1695–1705, 2019.

[221] Shivani Punj, Jashandeep Singh, and K. Singh. Ceramic biomaterials: Properties, state of the art and future prospectives. *Ceramics International*, 47(20):28059–28074, 10 2021.

[222] Devis Bellucci, Antonella Sola, Roberta Salvatori, Alexandre Anesi, Luigi Chiarini, and Valeria Cannillo. Role of magnesium oxide and strontium oxide as modifiers in silicate-based bioactive glasses: Effects on thermal behaviour, mechanical properties and in-vitro bioactivity. *Materials Science and Engineering C*, 72:566–575, 2017.

[223] Max Blochberger, Leena Hupa, and Delia S. Brauer. Influence of zinc and magnesium substitution on ion release from Bioglass 45S5 at physiological and acidic pH. *Biomedical Glasses*, 1(1):93–107, 2015.

[224] C. Moseke and U. Gbureck. Tetracalcium phosphate: Synthesis, properties and biomedical applications. *Acta Biomaterialia*, 6(10):3815–3823, 2010.

[225] Gamal A. Khater, Engie M. Safwat, Mohammad M. Farag, Iman A. Fathy, Hanem M. Awad, Ahmed Gamal Abd-Elsatar, and Ahmad G.A.

Khater. Bioactive Glasses Based on Sodium Disilicate and Tetracalcium Phosphate Compositions for Bone Grafting Applications. *Silicon*, 2 2025.

[226] Daniel Groh, Franziska Döhler, and Delia S. Brauer. Bioactive glasses with improved processing. Part 1. Thermal properties, ion release and apatite formation. *Acta Biomaterialia*, 10(10):4465–4473, 10 2014.

[227] H. A. ElBatal, E. M.A. Khalil, and Y. M. Hamdy. In vitro behavior of bioactive phosphate glass-ceramics from the system P2O5-Na2O-CaO containing titania. *Ceramics International*, 35(3):1195–1204, 2009.

[228] Zhen Geng, Zhenduo Cui, Zhaoyang Li, Shengli Zhu, Yanqin Liang, William Weijia Lu, and Xianjin Yang. Synthesis, characterization and the formation mechanism of magnesium- and strontium-substituted hydroxyapatite. *Journal of Materials Chemistry B*, 3(18):3738–3746, 5 2015.

[229] Biological evaluation of medical devices-COPYRIGHT PROTECTED DOCUMENT. Technical report, 2009.

[230] Radu Albulescu, Adrian Claudiu Popa, Ana Maria Enciu, Lucian Albulescu, Maria Dudau, Ionela Daniela Popescu, Simona Mihai, Elena Codrici, Sevinci Pop, Andreea Roxana Lupu, George E. Stan, Gina Manda, and Cristiana Tanase. Comprehensive in vitro testing of calcium phosphate-based bioceramics with orthopedic and dentistry applications. *Materials*, 12(22), 11 2019.

[231] Arun K. Varshneya and John C. Mauro. Introduction. *Fundamentals of Inorganic Glasses*, pages 1–18, 2019.

[232] P. Rajeshwari and T. K. Dey. Thermogravimetric kinetics of degradation of HDPE based MWCNTs reinforced composites. *International Journal of Plastics Technology*, 18(2):294–320, 2014.

[233] Wensheng Han, Mengjie Ran, Chang Chen, Guoxing Ren, and Wen Chen. Non-isothermal crystallization kinetics of calcium pyroniobate (Ca2Nb2O7) in SiO2-CaO-Nb2O5-Na2O-MgO-Al2O3 glass. *Thermochimica Acta*, 734, 4 2024.

[234] I. Avramov, Ts Vassilev, and I. Penkov. The glass transition temperature of silicate and borate glasses. *Journal of Non-Crystalline Solids*, 351(6-7):472–476, 2005.

[235] Paramjyot Kumar Jha, O. P. Pandey, and K. Singh. Non-isothermal crystallization kinetics of K2O modified sodium-phosphate glasses. *Journal of Non-Crystalline Solids*, 440:76–84, 2016.

[236] Takashi Uchino, Tetsuo Sakka, and Matae Iwasaki. Interpretation of Hydrated States of Sodium Silicate Glasses by Infrared and Raman Analysis. *Journal of the American Ceramic Society*, 74(2):306–313, 1991.

[237] Xiaonan Lu, Lu Deng, Caitlin Huntley, Mengguo Ren, Po Hsuen Kuo, Ty Thomas, Jonathan Chen, and Jincheng Du. Mixed Network Former Effect on Structure, Physical Properties, and Bioactivity of 45S5 Bioactive Glasses: An Integrated Experimental and Molecular Dynamics Simulation Study. *Journal of Physical Chemistry B*, 122(9):2564–2577, 2018.

[238] Xiaoju Wang, Susanne Fagerlund, Jonathan Massera, Berndt Södergård, and Leena Hupa. Do properties of bioactive glasses exhibit mixed alkali behavior? *Journal of Materials Science*, 52(15):8986–8997, 8 2017.

[239] J. Massera, L. Hupa, and M. Hupa. Influence of the partial substitution of CaO with MgO on the thermal properties and in vitro reactivity of the bioactive glass S53P4. *Journal of Non-Crystalline Solids*, 358(18-19):2701–2707, 2012.

[240] S M Salman and S N Salama. The role of strontium and potassium on crystallization and bioactivity of Na 2 O – CaO – P 2 O 5 – SiO 2 glasses. 38:55–63, 2012.

[241] Navneet Kaur Mattu and Kulvir Singh. Structurally modified bioglasses synthesized using agro-food wastes and conventional sources for bone regeneration application. *Ceramics International*, 49(23):38910–38920, 2023.

[242] K. Naemchan, S. Meejoo, W. Onreabroy, and P. Limsuwan. Temperature effect on chicken egg shell investigated by XRD, TGA and FTIR. *Advanced Materials Research*, 55-57:333–336, 2008.

[243] K E Wallace, R G Hill, J T Pembroke, and P V Hatton. Influence of sodium oxide content on bioactive glass properties. *Journal of Materials Science: Materials in Medicine*, 10:697–701, 1999.

[244] Fangzhu Qing, Zhe Wang, Youliang Hong, Ming Liu, Bo Guo, Hongrong Luo, and Xingdong Zhang. Selective effects of hydroxyapatite nanoparticles on osteosarcoma cells and osteoblasts. *Journal of Materials Science: Materials in Medicine*, 23(9):2245–2251, 9 2012.

[245] Ishu Kansal, Alluamarnath Reddy, Francisco Muñoz, Seong Jun Choi, Hae Won Kim, Dilshat U. Tulyaganov, and José M.F. Ferreira. Structure, biodegradation behavior and cytotoxicity of alkali-containing alkaline-earth phosphosilicate glasses. *Materials Science and Engineering C*, 44:159–165, 11 2014.

[246] K E Wallace, R G Hill, J T Pembroke, and P V Hatton. Influence of sodium oxide content on bioactive glass properties. *Journal of Materials Science: Materials in Medicine*, 10:697–701, 1999.

[247] Antonio Tilocca. Sodium migration pathways in multicomponent silicate glasses: Car-Parrinello molecular dynamics simulations. *Journal of Chemical Physics*, 133(1), 7 2010.

[248] Devis Bellucci, Valeria Cannillo, and Antonella Sola. Calcium and potassium addition to facilitate the sintering of bioactive glasses. *Materials Letters*, 65(12):1825–1827, 2011.

Appendix

The following are the Figures corresponding to the FTIR spectra of the different glasses in the range of 4000-400 cm^{-1}.

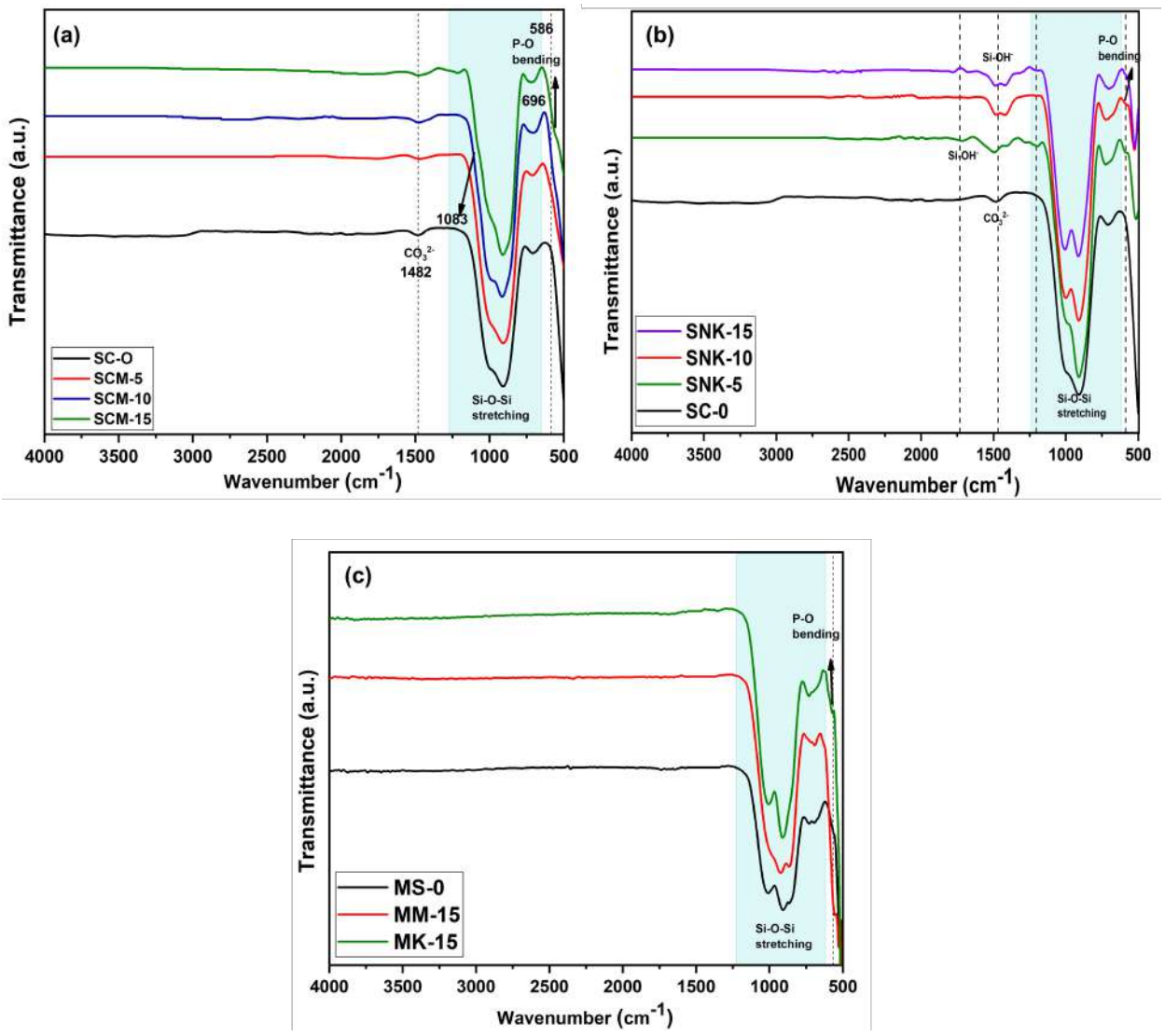

Figure A1: FTIR spectra of hybrid-source-derived glasses: (a) SC-0, SCM-5, SCM-10, and SCM-15 glass; (b) SC-0, SNK-5, SNK-10, and SNK-15 glass; (c) Represents the spectra of conventional chemical-derived glass in 4000-400 cm^{-1}

- MgO series: (SC-0, SCM-5, SCM-10 and SCM-15 after immersion in SBF for different time duration.)

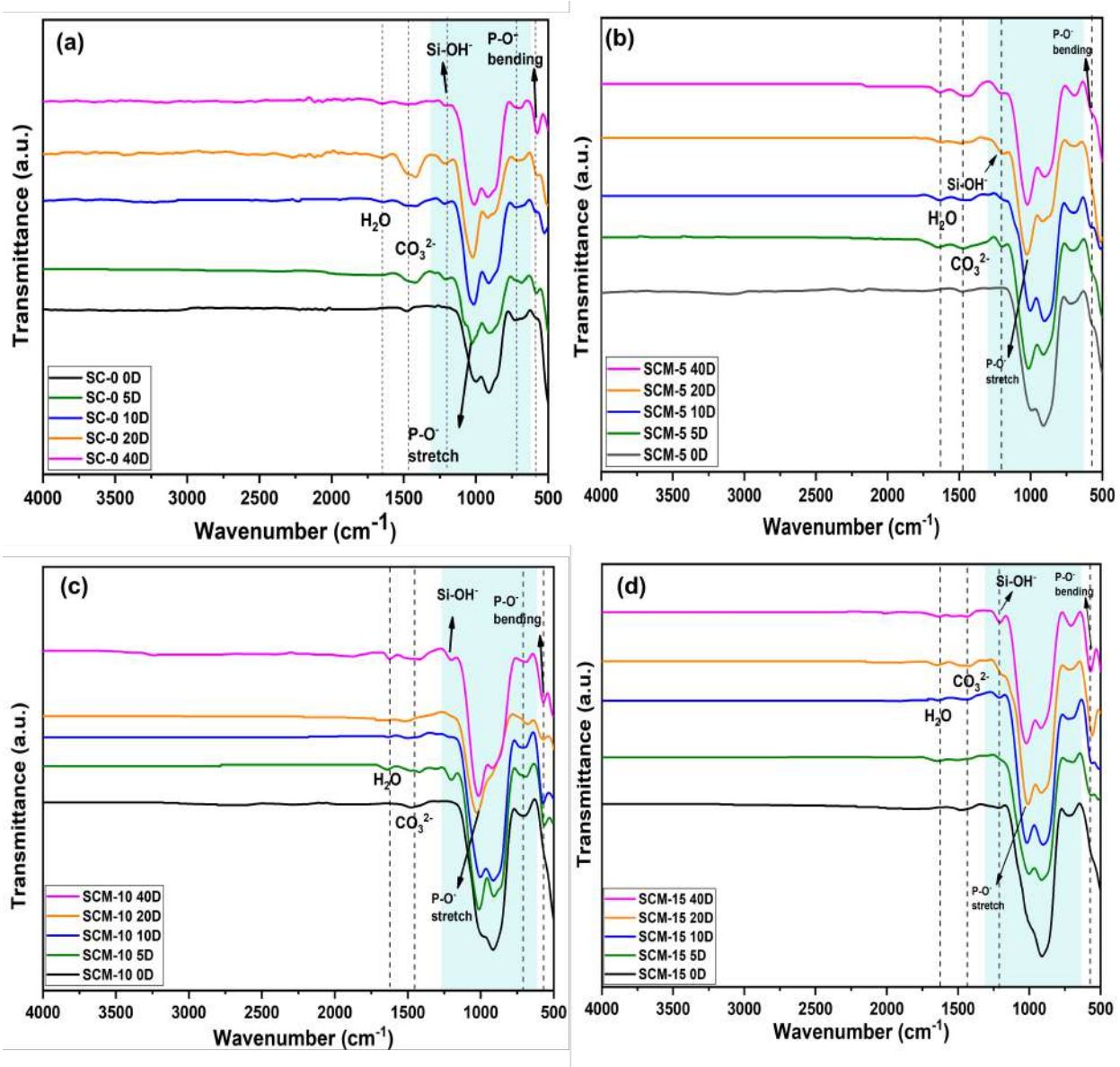

Figure A2: FTIR spectra of SC-0, SCM-5, SCM-10, and SCM-15 glass in 4000-400 cm^{-1} after immersion for 0,5,10,20, and 40 days.

- K_2O series: (SC-0, SNK-5, SNK-10, and SNK-15 after immersion in SBF for different time duration.)

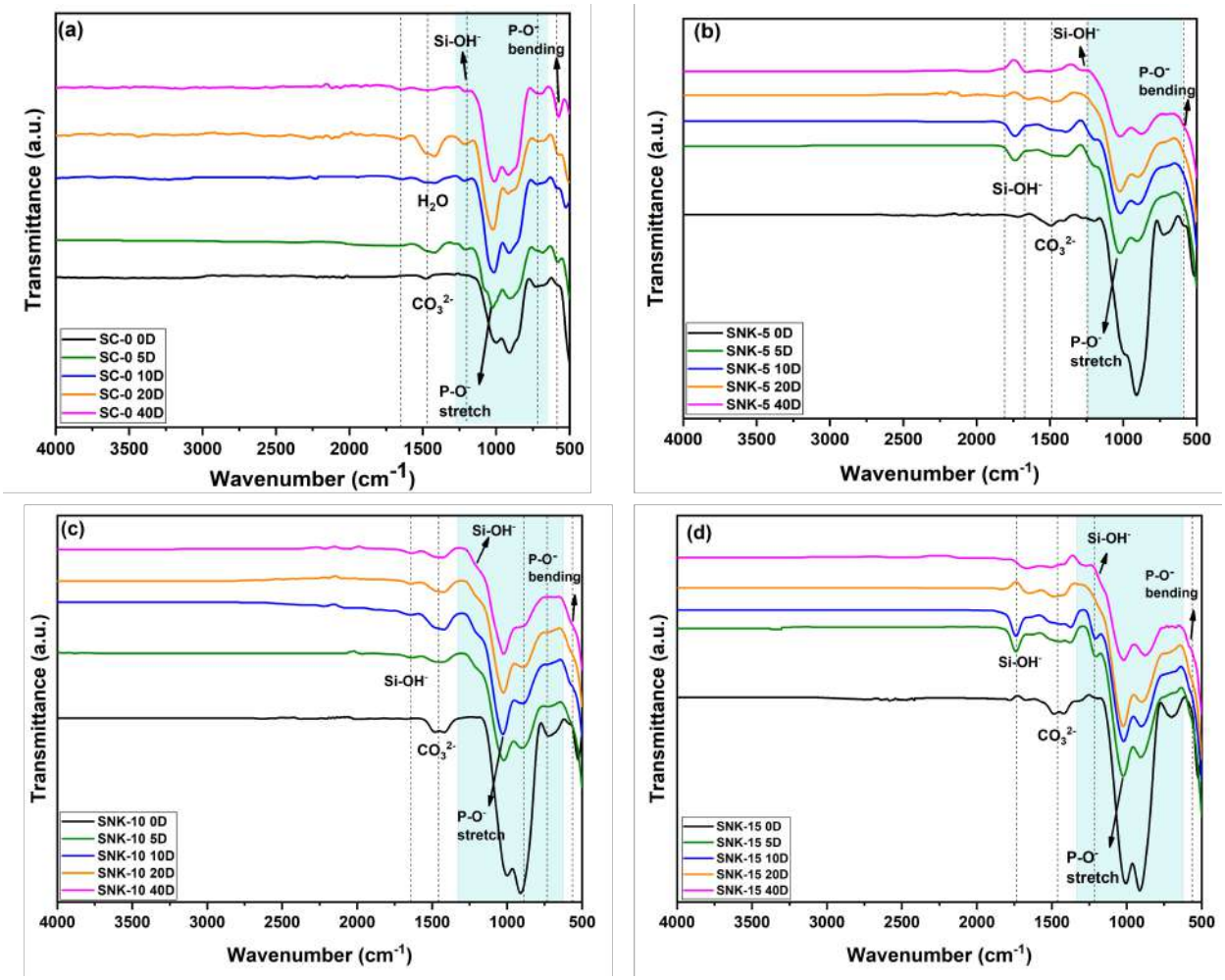

Figure A3: FTIR spectra of SC-0, SNK-5, SNK-10, and SNK-15 glass in 4000-400 cm^{-1} after immersion for 0,5,10,20, and 40 days

- Conventional chemical-derived glasses: (MS-0, MM-15, and MK-15 after immersion in SBF for different time duration.)

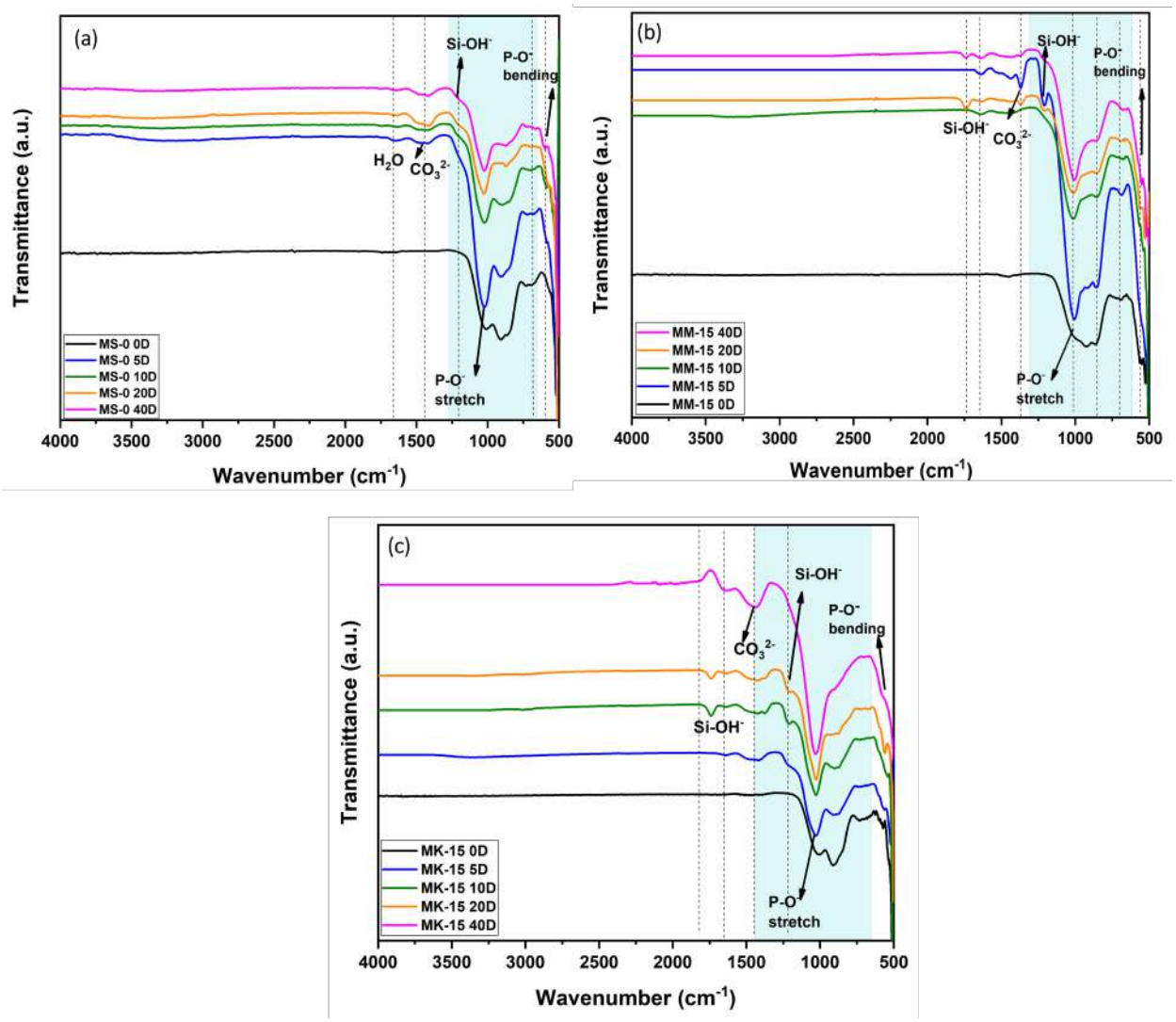

Figure A4: FTIR spectra of MS-0, MM-15, and MK-15 glass in 4000-400 cm^{-1} after immersion for 0,5,10,20, and 40 days